DEPARTMENT OF PHYSICS
UNIVERSITY OF JYVÄSKYLÄ
RESEARCH REPORT No. 3/2012

EXPERIMENTAL STUDY OF ELECTRON TRANSPORT IN MESOSCOPIC CARBON BASED NANOSTRUCTURES

BY
DAVIE MTSUKO

Academic Dissertation
for the Degree of
Doctor of Philosophy

To be presented, by permission of the
Faculty of Mathematics and Science
of the University of Jyväskylä,
for public examination in Auditorium FYS-1 of the
University of Jyväskylä on May 11, 2012
at 12 o'clock noon

Jyväskylä, Finland
May 2012

Preface

The experimental work reported in this thesis has been carried out during the years 2007-2011 at the Nanoscience Centre, Department of Physics in the University of Jyväskylä.

The work was done within the Molecular Technology group under the guidance of Professor Markus Ahlskog and in collaboration with Professor Reghu Menon of the Molecular Electronics group at Indian Institute of Science. I am very grateful to Professor Markus Ahlskog for the advice and mentorship and also for giving me a rare opportunity to do nanotechnology research in his group.

I acknowledge Vaibhav Varade for his assistance in fabrication of polymer samples. Many thanks to Mikael Pajunen and Jarkko Lievonen for their assistance in imaging of samples. I also acknowledge Jaakko Leppäniemi for introducing me to the dilution fridge and initiating me to field effect transistor device measurements and Asaf Avnon for initiating me to polypyrrole synthesis. I acknowledge Dr. Andreas Johansson for his guidance in measurements and instrumentation and Tuuli Gröhn for the LabVIEW programming. I also acknowledge Antti Nuottajärvi and Tarmo Suppula for helping me with cryogenics and fabrication instrumentation.

I also acknowledge the Department of Physics of Jyväskylä for financial resources for this thesis project and teaching staff from whom I have learnt the fundamentals of nanoscience, electronics and condensed matter physics.

I enjoyed my interaction with Tero Isotalo and Ping, in particular for the Coffee room chats, and Olli Herranen and Deep Talukdar for the discussions on sample preparation and electron transport.

I am also grateful to my family in Malawi for their support and also for bearing with my long absence during the 7 years of my studies and research work in Finland.

Jyväskylä, May 2012

Davie Mtsuko

Abstract

Davie, Mtsuko
Experimental study of electron transport in mesoscopic carbon based nanostructures
Jyväskylä: University of Jyväskylä, 2012,138p
(Research report/Department of Physics, University of Jyväskylä,
ISSN 0075-465X; 3/2012)
ISBN 978-951-39-4723-1
diss.

In this thesis we have studied experimentally electronic transport in mesoscopic hybrid polypyrrole-gold devices and single multiwalled carbon nanotube devices.

A novel fabrication technique for mesoscopic conducting hybrid polymer-gold films has been developed. The hybrid polymer-gold films have been fabricated by electrochemical deposition of polypyrrole on a gold nanoisland layer. Temperature dependence of conductance show that the dominant transport mechanism in the polypyrrole-gold films is variable range hopping in the temperature range from 20 K to 300 K. At very low temperature strong nonlinearities in the field dependent conductance are observed. The field dependence follows a phenomenological model that is different from conventional field dependent transport theories probably due to the presence of gold islands embedded in polymer.

Further, we have explored size and temperature dependences of basic electrical properties of intermediate sized multiwalled carbon nanotubes in a diameter range, 3 to 10 nm, which has not been systematically explored previously. In particular, we have observed in gate controlled conductance measurements, transport gaps which become more pronounced with decreasing temperature. Many transport features are found to scale with channel length and diameter of the nanotube devices. These include onstate and offstate resistances, on/off ratios, as well as periodicities of Coulombic oscillations. The kind of scaling behaviours observed are a manifestation of both diameter dependent intrinsic bandgaps and localization effects. However, some deviations from the scaling and complex transport gaps have also been observed which may be due to chiralities and possible interwall effects.

Keywords Electron transport, conducting polymer, multiwall carbon nanotube, atomic force microscopy, temperature dependence, size dependence

Author's address Davie Mtsuko
Nanoscience Center
Department of Physics
University of Jyväskylä
Finland

Supervisor Professor Markus Ahlskog
Nanoscience Center
Department of Physics
University of Jyväskylä
Finland

Reviewers Dr.Tech Hele Savin
Adjunct Professor (Docent)
Aalto University
Department of Micro and Nanosciences
P.O.BOX 13500, FI-00076 Aalto
Espoo
Finland

Ph.D Krister Svensson
Universitetslektor/Docent
Department of Physics and Electronics
University of Karlstad
651 88 Karlstad
Sweden

Opponent Dr.Tech Olli Salmela
Docent
Nokia Siemens Networks
Linnoitustie 6
02600 Espoo
Finland

List of Publications

The main results of this thesis have been reported in the following articles:

A.I. D.MTSUKO, A. AVNON, J.LIEVONEN, M.AHLSKOG, AND R.MENON, *Electrochemical deposition of polypyrrole on ultrathin gold films*. Nanotechnology **19** 125304 (2008).

A.II. D. MTSUKO, M. AHLSKOG, AND R. MENON., *Nonlinear transport in hybrid polypyrrole-gold nanostructures* . J. Nanosci. Nanotechnol. **10** (2010) 8185.

A.III. M. AHLSKOG, O. HERRANEN, A.JOHANSSON, J.LEPPÄNIEMI, AND D.MTSUKO, *Electronic Transport in intermediate sized carbon nanotubes*. Phys. Rev. B. **7** (2009) 155408.

Author's contribution

The author of this thesis did practically all of sample fabrication and measurements of publication A.I and A.II.

In A.I the author participated in writing the manuscript and analyzing the data. In A.II the author participated in analyzing the data and wrote the draft version of the publication.

In A.III, the author did part of the sample fabrication and a few electrical measurements.

Chapter 6 of this thesis contains results of publication A.III and much beyond it. The author did all of the sample fabrication, measurements, and data analysis of the work described in Chapter 6 of this thesis.

Contents

Preface i

Abstract iii

List of Publications vii

1 Introduction 1

2 Conducting polymers 5
2.1 Fundamental properties . . . 5
2.2 Polypyrrole synthesis . . . 8
2.3 Electron transport in conducting polymers . . . 8
2.4 Existing works on mesoscopic conducting polymers . . . 10

3 Multiwalled carbon nanotubes 15
3.1 Fundamentals of carbon nanotubes . . . 15
3.2 Synthesis of carbon nanotubes . . . 17
3.3 Theory of transport in carbon nanotubes . . . 18
3.3.1 Basic transport properties of nanotubes: Role of chirality and diameter . . . 18
3.3.2 Gate-controlled conduction . . . 21
3.3.3 Transport regimes . . . 25
3.3.4 Coulomb blockade regime in carbon nanotubes . . . 27
3.3.5 Magnetic field effects . . . 27
3.3.6 Transport in multiwall nanotubes . . . 29
3.3.7 Existing experiments on multiwalled nanotubes - Literature review . . . 31
3.3.8 Electron transport in Graphene nanoribbons . . . 32

4 Sample fabrication and measurement methods 35
4.1 Fabrication of microelectrodes . . . 36
4.2 Characterization and measurement techniques . . . 38

5 Mesoscopic conducting polymer devices 43
5.1 Novel fabrication concept: Nanoscale hybrid PPy-Au device . . . 43
5.2 Ultrathin gold films . . . 44
5.3 Fabrication of polypyrrole on insulating substrates . . . 47
5.3.1 Fabrication of microelectrodes and ultrathin gold films . . . 47
5.3.2 Electrochemical Synthesis of polypyrrole on substrates . . . 49
5.4 Results on transport measurements in PPy-Au structures . . . 51

5.4.1 Room temperature conductivity of PPy-Au:Role of gold islands 51
5.4.2 Temperature dependence of conductance 53
5.4.3 Field dependence of conductance 54
5.5 Future outlook 58

6 Transport measurements on intermediate sized MWNTs 61
6.1 The goal: Experiments on electron transport in intermediate sized MWNTs 61
6.2 Fabrication of MWNT samples 62
6.2.1 Nanotube material with a special diameter range 62
6.2.2 Fabrication of backgated MWNT devices 62
6.3 General transport features in MWNTs 65
6.4 Measurements on gapped MWNTs 69
6.4.1 Size and temperature dependence of the minimum on-state resistance 70
6.4.2 Size dependence of the Resistance ratio 74
6.4.3 Size and temperature dependence of maximum offstate resistance 74
6.4.4 Size dependence of the bias voltage gap 77
6.4.5 Coulomb blockade oscillations 78
6.5 Metallic and quasimetallic MWNTs 80
6.6 Conclusions on transport in intermediate sized multiwall nanotubes 83
6.7 Future outlook 84

7 Summary 85

Chapter 1

Introduction

This thesis consist of experimental work on nanoscale carbon based conducting materials; conducting polymers (CP) and carbon nanotubes (CNT) (Fig. 1). Carbon has four valence orbitals, namely $2s$, $2p_x$, $2p_y$ and $2p_z$. The first three orbitals take part in sp^2 orbital hybridization forming σ-bonding molecular orbitals. In both carbon nanotubes and conducting polymers the $2p_z$ electrons form π-bonding orbitals [1], [2]. Delocalisation of π-electrons can lead to metallic conductivity in both of these materials [3].

The electrical properties of CNTs and CPs are influenced by many factors including structural disorder, sample size, geometry and chemical doping that can lead to both metallic and semiconducting behaviour. The wide range of properties gives CPs and CNTs a high potential for applications in electronics. The electrical properties of CNTs and CPs have been extensively studied over the past three decades for a deeper understanding of the charge transport mechanism in these materials. However, there is still alot ongoing research works to address unanswered questions on some aspects of transport in these systems and for probing interesting physical phenomena lower dimensions. Low temperature transport studies in conducting polymers have shown variable range hopping and Efros-Shlovskii (ES) hopping as the dominant conduction mechanism [4]. In CNTs, especially in single walled ones, ballistic conduction has been observed and consequently different quantum transport phenomena such as Fabry-Perot interference, for example, have also been reported [5].

In literature of both CPs and CNTs, we observe that, there exist some ranges of size that have not been adequately explored owing to either fabrication difficulties in nanoscale CP samples or complexity of structure as is the case in multiwall nanotubes (i.e concentrically arranged single wall nanotubes) where a 0.34 nm interlayer spacing raises possibility of intershell transport between walls that can be wrapped in many different ways.

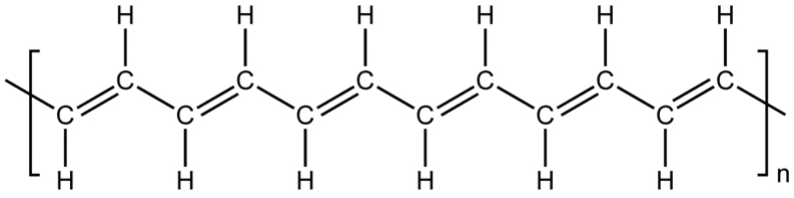

(a)

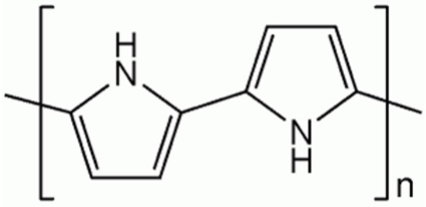

(b)

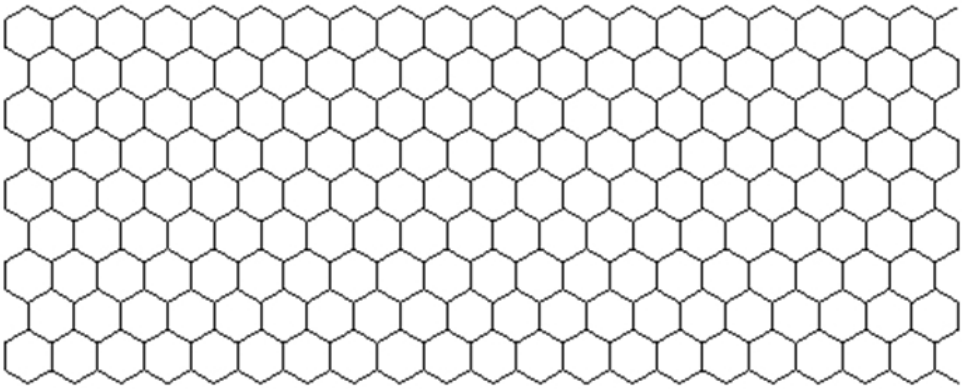

(c)

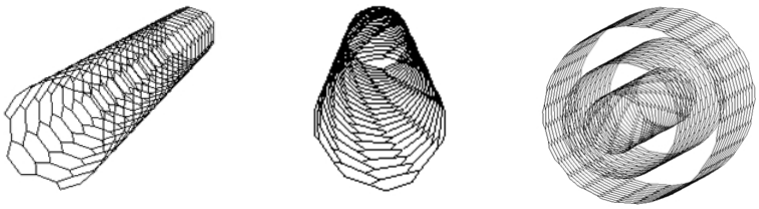

(d) (e) (f)

FIGURE 1.1 Molecular structures of conducting polymers and carbon nanotubes. (a) Molecular structure of polyacetylene showing alternating single and double C-C bonds. (b) Structure of polypyrrole, the conducting polymer studied in this thesis work. (c) A two-dimensional graphene sheet that can be wrapped in many ways leading to one-dimensional (d) achiral nanotubes or (e) chiral nanotubes. (f) Multiwalled carbon nanotubes (MWNT) have many nanotubes arranged concentrically.

In this thesis size dependence and other aspects of electrical properties are explored in:

- - sub-200 nm thin films of polypyrrole (PPy) electrochemically deposited onto a discontinuous layer of gold islands. The significance of a gold island layer is two-fold. It promotes rapid lateral growth leading to long thin films and provides an opportunity to study transport at small size scale corresponding to nanoscale inter-island spacing.

- - Individual back-gated multiwalled carbon nanotube devices (MWNT) in the diameter range 3 - 10 nm. There is previously hardly any work on MWNTs in this diameter range. This work therefore bridges the study gap between the works on single- and double walled CNTs and MWNTs of diameter > 10 nm.

The CP samples and MWNTs studied in this work are mesoscopic since their size falls within the size range 1 nm to 1 μm [6]. This leads to quantum confinement as one dimension of the sample becomes comparable to the electronic wavelength. The CP thin film samples are more two-dimensional with thickness comparable to diameter of quasi-one-dimensional CP nanofibres, CP nanotubes or CP nanowires as reported in literature [7], [8], [9], [10], [11], [12]. Mesoscopic conducting polymers and multiwall carbon nanotubes offer an opportunity to study low dimensional physics and are useful for nanoelectronics applications such as nanoscale sensors, high speed memory devices, field effect transistors (FET) and interconnects of nanoscale electronic devices.

Chapter 2

Conducting polymers

2.1 Fundamental properties

The term polymer is often associated with saturated polymers like polyethylene, which are used to make ordinary plastic items that are electrically insulating. There is, however, a class of polymers called 'conducting polymers' that can exhibit electrical properties like metals or semiconductors. Conducting polymers are generally conjugated polymers that have alternating single and double carbon-carbon bonds along their constituent polymer chains, as typified in the structure of polyacetylene shown in Fig.1(a).

The difference in electrical properties of saturated polymers and conducting polymers can be understood in terms of sp^3 and sp^2 orbital hybridization of carbon. In polyethylene, there is sp^3 hybridization such that all valence electrons are locked up in covalent bonds and therefore not available for electron transport. In contrast, the sp^2 hybridization in conjugated polymers leaves one unbonded electron per carbon atom that can delocalize along the chain leading to conduction. This sp^2 hybridization is also responsible for the structure and electrical conduction in graphene as well as in carbon nanotubes, as discussed in Chapter 1.

Examples of conducting polymers (CPs) are polyacetylene (PA) and polypyrrole (PPy), the polymer used in this work and shown in Fig.1(b). Due to delocalization of π-electrons along the polymer chain, CPs are theoretically predicted to exhibit metallic behavior comparable to that of copper. However, owing to disorder, the bulk conductivities of CPs are much lower than conductivity of copper. In fact, intrinsic conjugated polymers exhibit semiconducting behavior where as doped CPs can exhibit conductivity in the range 1 S/cm to 10^4 S/cm depending on the doping level, degree of disorder, and chain orientation.

The significance of studying electrical properties of CPs is two-fold. Firstly, CPs have a good potential for many applications that need a combination of good mechanical properties of plastics and good electrical properties such as wearable electronics, flexible displays light emitting diodes, interconnects and electrostatic shielding materials. A good understanding of charge transport mechanisms behind their electrical properties is useful in the tuning of those properties for a particular application.

Secondly, CPs are important for study of fundamental physics. In the field of condensed matter physics CPs present a good material in which nonlinear excitations known as solitons can be studied. Solitons lead to formation of midgap states in the bandstructure of polyacetylene, the most simple conducting polymers. The soliton refers to a region (or a domain wall) where there is a change in single-to-double bond alternation caused by the dopant as illustrated in Fig.2.1 [13], which is possible since in polyacetylene both alternations are energetically equivalent. On doping of a polymer chain, soliton formation is more favoured than hole or electron excitation, since the chemical potential of undoped polymer is in the mid of the gap. This means that solitons do form spontaneously with less cost.

In nondegenerate conjugated polymers, as they usually are, the possible excitations are known as polarons and bipolarons,which are illustrated in Fig.2.2 [10]. A polaron with spin-½ is formed when a single electron is injected into the chain (by doping). Addition of extra hole or electron leads to a spinless bipolaron formation. This spin-charge decoupling phenomena in highly doped polymers is one of the great triumphs of conducting polymers in physics [13].

Over the past two decades a lot of electron transport studies have been done in macroscopic CP samples [4]. One would wish to extend those studies to mesoscopic and nanoscale systems for the sake of studying physical phenomena in those and in the hope of using CPs as nanowires and nanoscale FETs. Very few works have been reported since fabrication of well defined CP mesoscopic samples is in general a difficult task and that they tend to exhibit more insulating behaviour at low temperature. The other reason for the scarcity of works is the instability of conducting polymers which can be more severe in mesoscopic samples. However with various modern fabrication techniques such as dip pen nanolithography [14], it is possible to fabricate mesoscale CPs with better quality. More low temperature works on mesoscopic polymers are needed since there are still a few unresolved issues on transport at small length scales. This is the source of motivation for our work on submicron size CP samples.

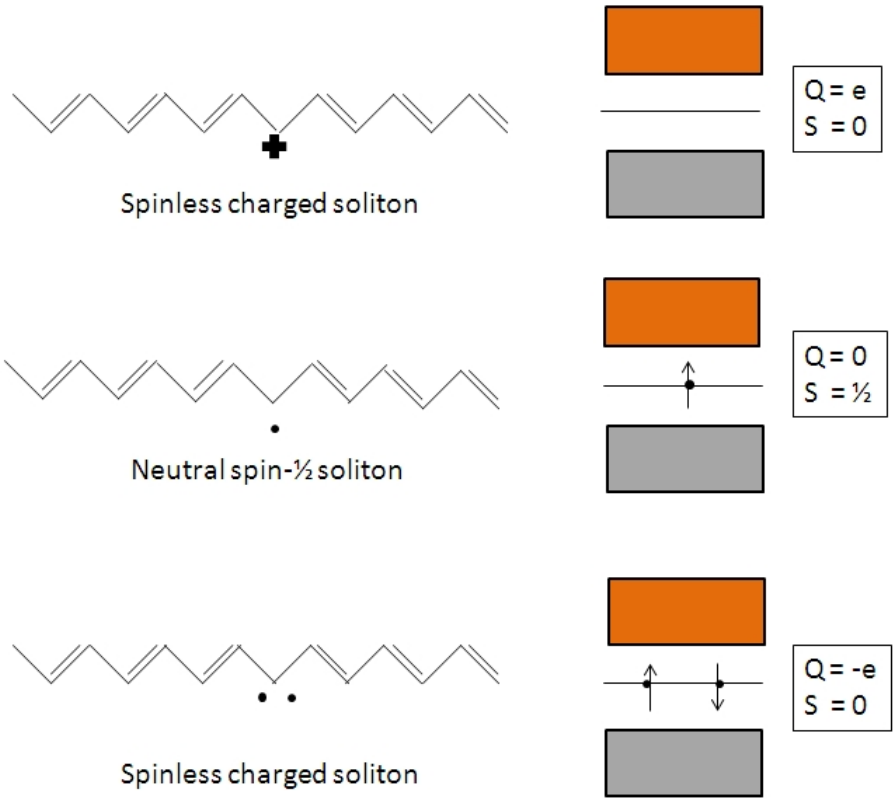

FIGURE 2.1 Illustration of solitons or bond alternation domain walls in polyacetylene. Note that this is just a localized shorthand for otherwise delocalised structures. On the right are the electronic structures with various charge and spin states. The horizontal line is the Fermi level.

2.2 Polypyrrole synthesis

Polypyrrole can be synthesized via chemical, electrochemical and photochemical means. All these techniques involve three stages, namely initiation, propagation and termination as shown in Fig. 2.3 [10]. The initiation phase involves oxidation of precursor monomers to form radical cations which are then coupled and deprotonated to form bipyrroles. The bipyrroles are subjected to further oxidation in the propagation stage and linked to form longer polymer chains. The electrochemical method is known to yield by far the highest quality PPy with the best conductivity. Chemical methods yield polymers with low conductivity and are only suitable for mass production of PPy. The oxidation of the PPy leaves excess negative charge on the polymer chain which is balanced by counterions which act as dopants. Suitable dopants are hexafluorophosphate (PF_6) and camphorsulfonic acid (CSA). The influence of doping level on electron transport in polypyrrole is discussed in section 2.3.

2.3 Electron transport in conducting polymers

Pristine conjugated polymers usually have low conductivity but raising the doping level can considerably raise their conductivity. The doping level can be measured in terms of the number of dopants per monomer. The doping level influences the nature of charge carrier in the polymer. For instance, in lightly doped polypyrrole the charge carrier is a polaron where as in highly doped polymer the carrier is a spinless bipolaron as shown in Fig.2.2 [10]. In the languange of band theory, doping alters the bandstructure of the polymer with respect to the fermi level or chemical potential of contact electrodes as shown in the band diagrams in Fig.2.2 [10].

In disordered conjugated polymers electron transport is influenced by π electron delocalization, interchain interaction, band gap, carrier density, level of disorder, morphology and distribution of dopants [2]. Considering π electron delocalization alone CPs are predicted to be metallic with high conductivities comparable to that of copper on account of a high density of states (DOS) of charge carriers and long mean free path along chain direction for well oriented polymers. However, disorder leads to low mobility and hence low conductivity. Transport in CPs is therefore discussed in the context of disorder-induced metal-insulator transition (MIT). Depending on the nature of disorder many possible charge transport mechanisms such as hopping between localized states and tunneling between metallic domains in the polymer may occur.

There has been a vigorous debate [2] over whether the appropriate model for

charge conduction in CPs is homogeneously or heterogeneously disordered CPs, as illustrated schematically in Fig.2.4. In the former, electrical properties are dominated by inter-chain and intrachain hopping of charge carriers between homogeneously distributed localized states, and in the latter case by transport (direct tunneling, hopping) between metallic regions in heterogeneously disordered CP materials (Fig.2.4) [10]. A good analog of heterogeneously disordered CPs are cermet like hybrid materials where metallic grains are embedded in an insulating polymer material. In this work, our samples have gold islands that are embedded in a conducting polymer (PPy), such that at low temperature when the polymer becomes more insulating the composite sample can possibly be treated as a heterogeneously disordered system where transport will be mainly by tunneling from gold island to gold island.

For homogeneously disordered CPs phonon assisted variable range hopping (Mott VRH) is usually the dominant transport mechanism for samples in the insulating (Fermi glass) regime of MIT. In this regime the temperature dependence of conductivity is given as

$$\sigma\left(T\right)=\sigma\left(0\right)\exp\left[-\left(\frac{T}{T_0}\right)^{P}\right] \tag{2.1}$$

where σ_0 is a parameter that depend on the sample and the factor
$T_0 = 4\pi/3N(\epsilon_F)k_B L_o^3$ where L_o is the localization length and $N(\epsilon_F)$ is the density of states at Fermi level [4], [10]. The exponent $P = 1/(d+1)$ where d (= 1, 2 and 3) is dimensionality of transport. In samples where electron-electron interaction energies are significant there are usually cross-overs from Mott VRH to the Efros-Schlovskii (ES) VRH model, where the temperature dependence of conductivity is given as

$$\sigma\left(T\right)=\sigma\left(0\right)\exp\left[-\left(\frac{T}{T_{ES}}\right)^{1/2}\right] \tag{2.2}$$

for all dimensions where T_{ES} is the characteristic ES temperature [15], [4].
For the case of heterogeneously disordered CPs, where electron transport is by tunneling between metallic islands separated by thin insulating barriers, tunnelling models such as Sheng's fluctuation induced tunneling (FIT) and charging energy limited tunneling (CELT) can be considered [10]. In the Sheng's model field dependent tunneling current density across an insulating barrier can be expressed as

$$J\left(E_A\right)=\int_{\infty}^{-\infty}dE_T J\left(E_A+E_T\right)\Gamma\left(E_T\right) \tag{2.3}$$

where E_A is the applied electric field and $\Gamma(E_T)$ is the probability that the tunneling barrier junction has a fluctuation of the field E_T [11]. A more handy conductance expression for temperature dependence of conductance in heterogeneously disordered systems with large metallic islands is given by equation2.4

$$\sigma\left(T\right) = \sigma_t exp\left[\frac{T_t}{T+T_s}\right] \tag{2.4}$$

where T_t is the temperature at which thermal voltage fluctuations across the tunneling barrier become large enough to rise energy of electronic states above the barrier and the ratio T_t/T_s implies tunneling in the absence of fluctuations [16].For very small metallic island FIT is said to predict a $\sigma(T) \propto -T^{-0.5}$ which is similar to 1D VRH behaviour [10].

For nanoscale CPs such as nanowires, nanotubes and ultrathin films at low temperature there is a need to take into account other low dimensional transport models such as Luttinger liquid models on account of short range electron-electron interactions and Wigner crystal behaviour due to long range Coulomb interactions [10]. Typical signatures of Luttinger liquid behavior are $G(T) \propto T^x$ at low bias and power law $I(V) \propto V^y$ at high bias [10].

In view of many possible models and variations from sample to sample it is important to examine critically the applicability of any of these models for each particular sample. Since a wide range of transport mechanisms, due to tunneling and hopping, are possible in PPy and the interfaces of gold and PPy, the charging energy and Coulomb correction effects are also expected to play a role in the hybrid PPy-Au system fabricated in this work.

2.4 Existing works on mesoscopic conducting polymers

Due to fabrication difficulties many of the most rigorous experimental studies of transport in CPs have been conducted in bulky films of thickness typically $\approx$ 100 μm and width 1 mm [4]. Such films can be thought of as being more 3-dimensional in nature although 1-dimensional transport behaviour has been observed at low temperature [4]. It would be interesting to study transport in conducting polymer at mesoscopic scales. Efforts to make submicron CPs has been demonstrated in fabrication of CP lines via electrochemical dip pen lithography [14]. Notable studies on low temperature transport studies in submicron CPs have been done on iodine doped polyacetylene fibre networks and also individual nanofibres [10], [17].

The individual polyacetylene fibres were found to exhibit current-voltage characteristics with strong nonlinearities. In polyacetylene nanofibres of width 15-100

nm, power law behaviours of $G(T) \propto T^x$ and $I(V) \propto V^y$ were reported and attributed to Luttinger liquid behaviour [18], [19]. Their data could not fit well 3D VRH models.

Other studies have been on PPy nanotubes of diameter 120 nm and wall thickness 20 nm that were chemically synthesized in polycarbonate poles [9]. Polyaniline (PANI) nanofibres [7], [8] of sizes 30 nm - 120 nm have been studied [10]. Notable works include also template-free self-assembled PPy and PANI nanotubes of diameters 100-120 nm and template synthesized 20 - 190 nm thick poly(3,4-ethylene dioxythiophene) (PEDOT) nanowires, where fluctuation induced tunneling (FIT) transport behavior [11], [12] has been observed. There has also been some transport studies on hybrid metal-polymer nanowires of diameters ≈80 nm prepared by sequential electrodeposition of PPy and metal in polycarbonate templates [20].

Further works have been on deposition of CPs on prefabricated microelectrodes. By making interelectrode spacings a few nanometers wide via electron beam lithography and then depositing CP electrochemically nanoscale metal-CP-metal junctions have been achieved [21]. In such junctions large conductance fluctuations have been observed and attributed to switching of redox states in individual polymer chains or nanoscale domains in the polymers [21]. In a closely related work, CP fabrication has been made on thin films of a few hundred nanometers thickness, fabricated by spin-coating chemically synthesized lightly doped polyalkylthiophenes or quinquethiophene on a discontinuous metal film island layer [22]. In other works hydrophobic pretreatment of insulating substrates has been used to promote rapid lateral growth thereby realizing thin films [23], [24], [25]. However these have been found to exhibit more insulating behavior.

In summary, all the techniques for fabrication of submicron CPs discussed above represent to some extent a good succes in extension of transport studies in conducting polymers towards the sub-100 nm (nanoscale) regime. Most of these works above have yielded samples that become more insulating at low temperature.This is not surprising given that most of the above works have been based on chemical synthesis methods which from earlier bulky CP studies are know to yield poor quality polymers compared to electrochemically synthesized CPs [10]. Experimental studies towards understanding transport mechanisms in these materials are still being pursued. Sub-20 nm CPs with high conductivity are still difficult to synthesize.

As we explain in section 5.1, the contribution of this thesis has been to fabricate a mesoscopic conducting polymer (PPy) device based on a novel concept and to measure its basic transport properties.

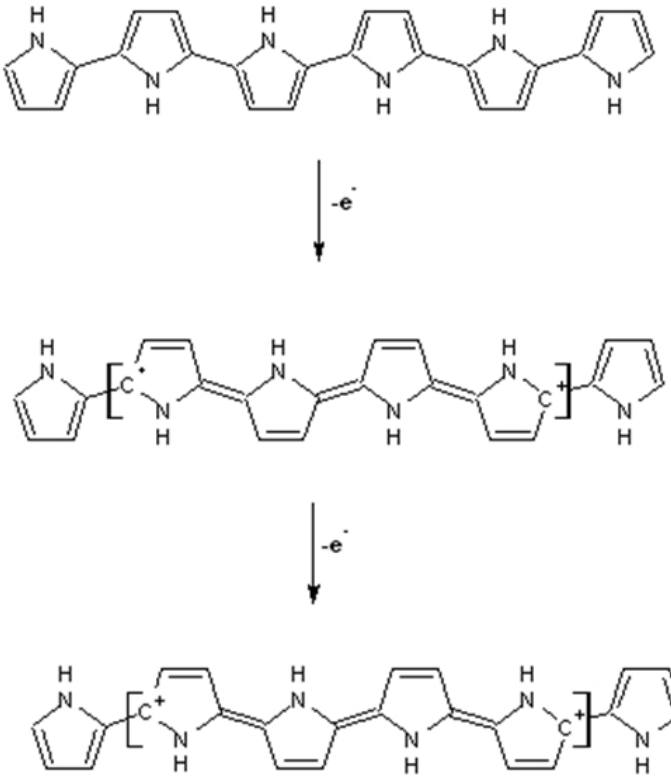

(a)

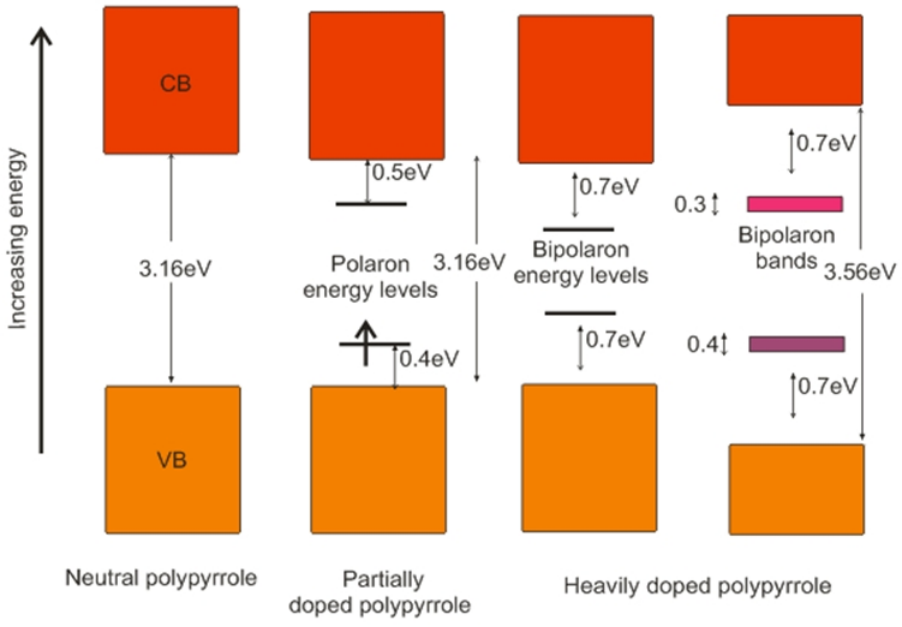

(b)

FIGURE 2.2 (a) Electronic structures of a non-degenerate polypyrrole illustrating polarons and bipolarons. (b) Corresponding band diagrams of polypyrrole at various doping levels. The neutral PPy (top) has a benzenoid structure whereas the doped PPy have a quinoid structure. The middle structure shows a polaron of charge +e and spin ½. The lower structure has charge +2e and no spin. [10].

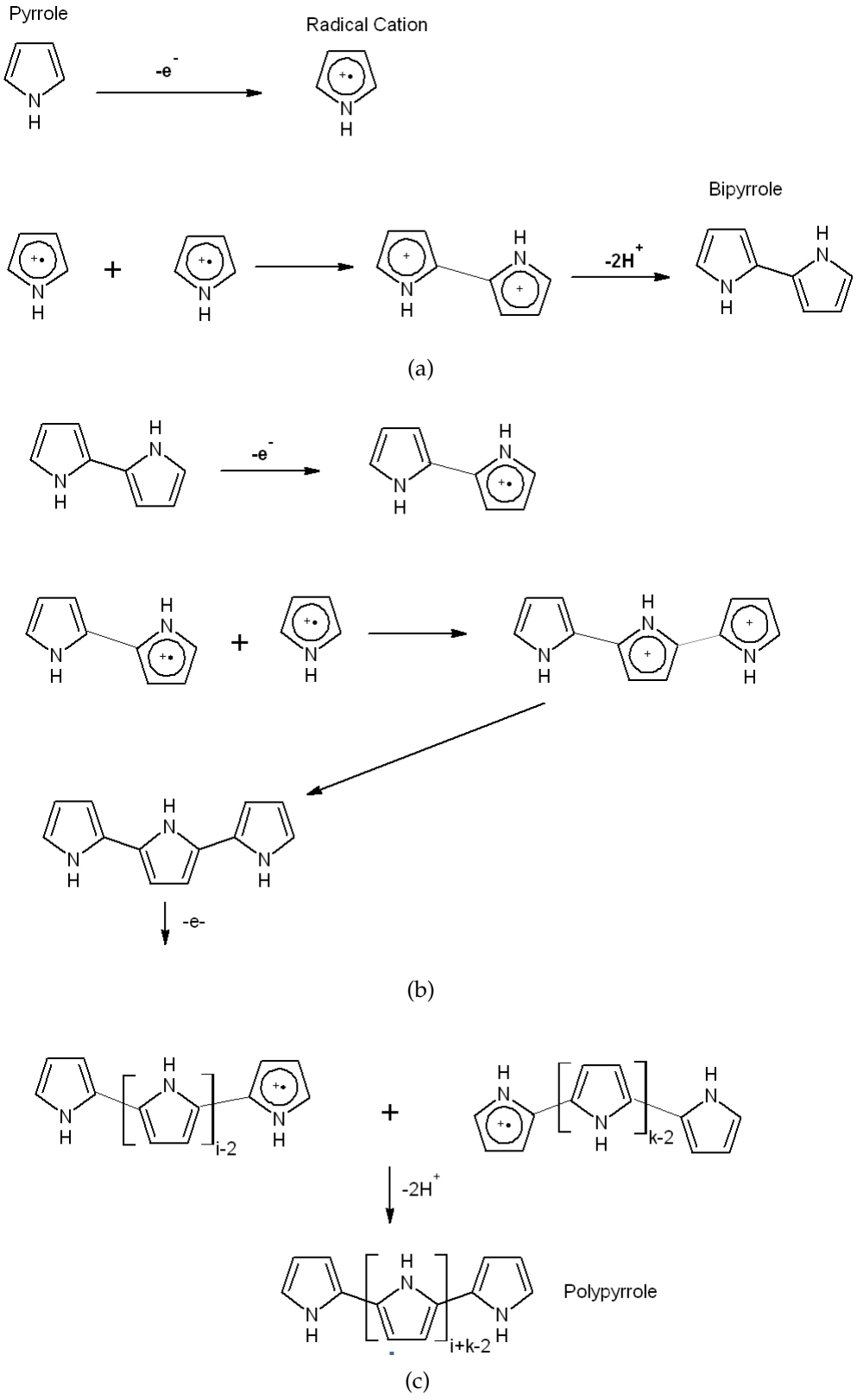

FIGURE 2.3 Synthesis of polypyrrole involves three stages namely (a)initiation, (b) propagation and (c) elongation.

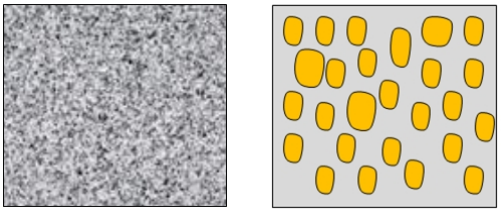

(a) (b)

FIGURE 2.4 Schematic illustration of (a) homogeneously disordered material and, (b) heterogeneously disordered material with conducting islands embedded in a non-conducting host material.

Chapter 3

Multiwalled carbon nanotubes

3.1 Fundamentals of carbon nanotubes

A carbon nanotube is an allotrope of carbon characterized by a high aspect ratio (i.e. nanoscale diameter and length that can exceed 1 μm. In terms of number of walls one can identify two classes of nanotubes namely single wall nanotubes (SWNT) and multiwall nanotubes (MWNT). A SWNT can be defined as a rolled graphene seamless cylinder where as a MWNT can be defined as a system of concentrically arranged nanotubes. This description of a true MWNT is referred to as the Russian doll model. The simplest form of a MWNT is a double wall nanotube (DWNT) [26] although many authors distinguish DWNT from the multiwall nanotubes (MWNT) structures where the number of walls, n is greater than 2 as illustrated in Fig. 3.1.

In addition to the Russian-doll type MWNTs there may exist deficient MWNT structures such as the parchment structure, in which the graphene layer is rolled like a newspaper or a scroll [27]. Temperature dependent X-ray diffraction studies have shown that the predominant MWNT structure for diameters below 10 nm is the concentric (Russian doll) tubular structure [28] in arc-discharge synthesized MWNTs. For diameter higher than 10 nm one should take into account the possibility of other geometrical structures as indicated in Fig. 3.2 and also highly defective

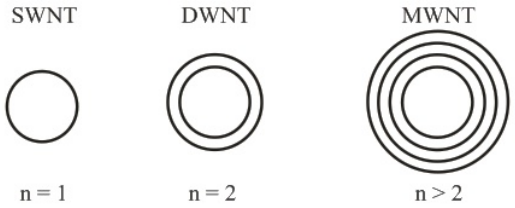

FIGURE 3.1 Cross-sections of carbon nanotubes with different number, n, of layers.

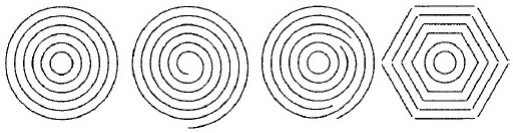

FIGURE 3.2 Structure of a MWNT, at left, and related or seriously defective MWNTs. Adapted from [28]

MWNT outer walls [28].

Due to their nanometric diameters and typical micrometric lengths carbon nanotubes are essentially regarded as quasi-one-dimensional (1D) structures. It has also been demonstrated that 0-dimensional structures, quantum dots, can be artificially formed along nanotubes. Very large diameter nanotubes may be regarded as 3-dimensional objects comprising of shells(tubes) that are themselves 2-dimensional structures. Due to this richness in dimensionality CNTs are important objects for fundamental studies of low dimensional electron transport phenomena.

Owing to chirality controlled electrical properties, high charge carrier mobilities up to 10^5 $cm^2V^{-1}s^-1$, high current carrying capacity, high thermal conductivities, mechanical strength and chemical stability, carbon nanotubes have a good potential for nanoelectronics applications as transistors, memory devices and interconnects. This has driven a lot of research effort over the last two decades to understand their properties as evidenced by scientometric studies conducted by Barth and Marx shown in Fig. 3.3. There has also been a rapid rise in research on two dimensional graphene, another carbon based material with many related properties to nanotubes but which is thought to be more suitable for realization of integrated circuits compared to nanotubes.

Whilst it is reasonable to argue that a lot of charge transport works has already been done in carbon nanotubes, recently reported works suggest that more intriguing physics phenomena could be still discovered or explored despite a decade of research [29]. Indeed, recently, phenomena such as one-dimensional Wigner crystallization [30], Klein tunneling [31] and spin-orbit coupling [32] have been observed in carbon nanotubes. These results provide a motivation for continuation of experimental studies of electron transport in them.

It is worth noting that most of significant low temperature electron transport experimental studies reported in literature have focused on small diameter single wall nanotubes (SWNTs) [5], [30], [31], [32] [33], [34], [35], [36], [37], [38] [39], [40], [41], [42], [43], [44], [45], [46], [47], [48], [49] [50], [51] and large diameter MWNTs [52], [53], [54], [55], [56], [57], [58], [59], [60], [61], [62] leaving the diameter range 3-

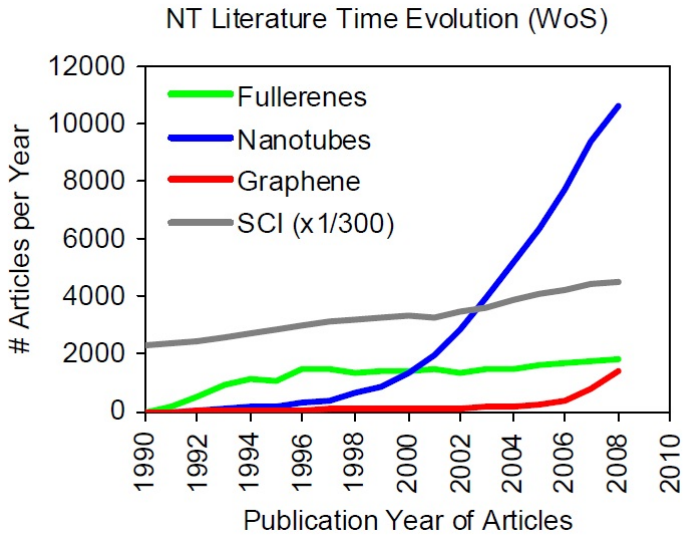

FIGURE 3.3 Number of articles on fullerenes, nanotubes and graphene per year. In this graph SCI is a science citation index based on hundreds of leading journals, used by Web of Science(WoS). Adapted from Scientometric studies by A.Barth and W.Marx, Max Planck Institute for Solid State Research based on Web of Science.

10 nm mainly unexplored. Our studies on intermediate sized nanotubes cover this diameter range [63]. Of course, there have been some reports on transport studies on sub-10 nm nanotubes but these have been on a single or few devices [64], [65] or at room temperature only. Our work provides a systematic study on size dependence of transport properties in MWNTs over a wide range of temperature with a large set of devices.

3.2 Synthesis of carbon nanotubes

Carbon nanotubes are synthesized using chemical vapour deposition, arc discharge and laser ablation techniques. In chemical vapour synthesis a carbon-containing feedstock gas is fed into a CVD chamber containing catalyst particles where temperature is maintained in the range 700 - 1000 ^{o}C. Depending on size of catalyst particles, SWNTs or MWNTs can be grown. In arc discharge synthesis, a vapour is produced by an arc discharge between two graphite rods and nanotubes can grow with or without catalyst. In laser ablation a graphite rod is targeted with a laser to create a vapour that can lead to growth, again with the presence of catalyst particles as optional.

The purity of nanotubes produced by these techniques vary depending on how a particular synthesis technique is tuned. CVD is known to produce MWNTs and large SWNTs whose diameters are poorly controlled. In general, laser ablation is

known to produce small quantities of clean nanotubes, whereas arc discharge is known to produce large quantities of impure samples. However some non-catalyst based variations of arc-discharge technique have been found to yield nanotubes of relatively good quality [66]. Nanotubes produced without catalyst particles are favourable for transport studies since catalyst removal (purification methods) involving acids may lead to defects in nanotube walls.

Chiral-selective synthesis, the holy grail of nanotube nanoelectronics applications, remains elusive. Exact synthesis mechanisms are not well established but are thought to involve nucleation, growth and termination stages. There have also been some recent works that suggest chirality driven growth rates in which some chiralities are more favoured [67].

3.3 Theory of transport in carbon nanotubes

Electron transport in nanotubes is influenced by many factors such as diameter, chirality, curvature, topological defects, chemical impurities, electron-electron interactions, electron-phonon scattering, etc. In this section factors that influence transport properties of nanotubes devices are discussed. A structural basis for semiconductivity or metallicity in nanotubes is presented first in 3.3.1. The effect of gate voltage and bias voltage on bandstructure of nanotube field effect devices is discussed in section 3.3.2. This is the most important section since a backgate voltage has been used to probe transport properties in all our samples. Transport regimes in general are discussed in the next section to highlight different scenarios or mechanisms in presence or absence of elastic or inelastic scattering. These are relevant to length scaling of transport properties explainable in terms of electron mean free paths and localization effects. A discussion on Coulomb blockade phenomena in nanotube quantum dots is included in view of studies on Coulomb oscillations done in this work. A special discussion on effects of interwall (or tube-tube) interaction in multiwall nanotubes is presented in section 3.3.6.

3.3.1 Basic transport properties of nanotubes: Role of chirality and diameter

The structural basis for metallicity or semiconductivity in nanotubes (rolled graphene cylinders) can be discussed starting from electronic structure of ideal flat graphene layer, a gapless material and then introducing effects of rolling and other structural perturbations to see how bandgaps open up. A good starting point is the tight bind-

ing model of graphene in which the dispersion relation is given as 3.1

$$E^{\pm} = (k_x, k_y) = \gamma_0 \sqrt{1 + 4cos\frac{\sqrt{3}k_x a}{2} cos\frac{k_y a}{2} + 4cos^2\frac{k_y a}{2}} \tag{3.1}$$

where, $a = \sqrt{3}a_{CC}$ is the graphene honeycomb lattice constant, where $a_{CC} \approx 0.142$ nm is the carbon-carbon bond length, and γ_0 is the π interaction energy (or the hopping integral) [1].

From this equation one can obtain the electronic structure of graphene as shown in Fig.3.4(a) where two cones (or lines in 2D) meet at a high symmetry point called the Dirac point. The linear dispersion in graphene means that graphene has no bandgap and hence will exhibit metallic behaviour.

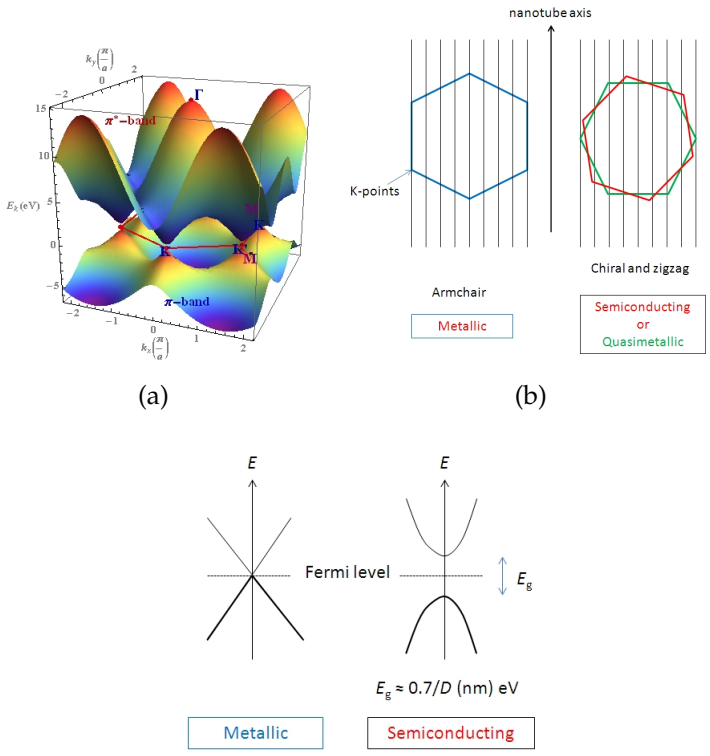

FIGURE 3.4 (a) Dispersion of graphene in 3D. The conical (linear in 2D) intersections of π and π* are called Dirac point imply that graphene has no bandgap. (b) Allowed vectors of nanotube on a graphene Brillouin zone. Metallicity or semiconductivity of nanotubes depends crucially on whether the wavevectors intersect or miss the high symmetry points of the BZ of graphene. (c) Corresponding electronic structures of nanotubes.

When rolled into a graphene cylinder (or nanotube) wavevectors around a nanotube circumference are quantized due to periodic boundary conditions, where

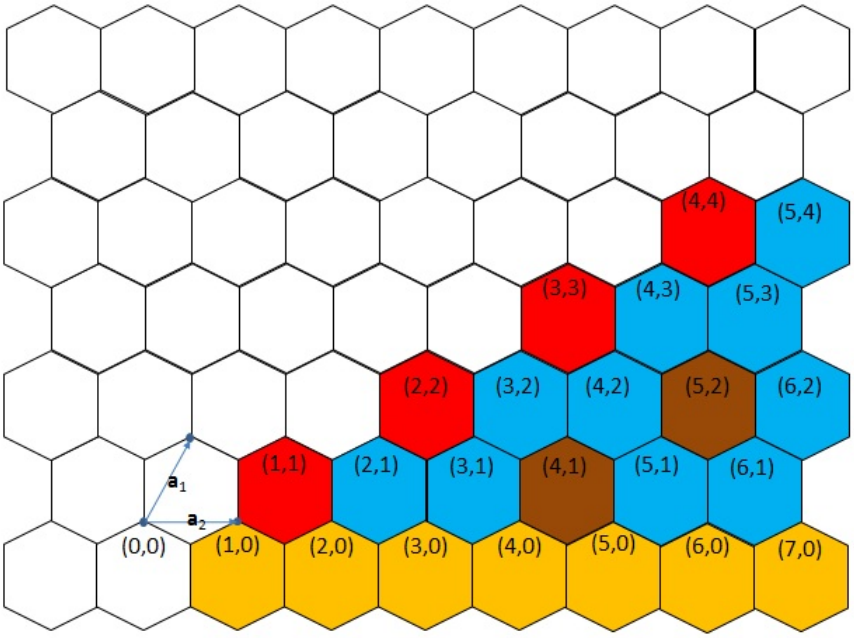

FIGURE 3.5 Chiral indices of nanotubes (n,m). In this figure the indices represent components of a vector that connects site (0,0) to a crystallographically equivalent site (n,m) when rolling graphene to form a tube. Nanotubes with indices (n, n) are armchair nanotubes which exhibit metallic behaviour. Nanotubes with indices $(n, 0)$ (zigzag) and those where $n - m = 3i$ are quasimetallic. The rest are semiconducting nanotubes.

as those along the tube axis are continuous. When the allowed wactors are drawn onto a brillouin zone of graphene, they form parallel lines as shown in Fig.3.4(b) that can intersect or miss high symmetry points of the brillouin zones. Depending on how allowed wavevectors are arranged with respect to the Brillouin zone of graphene one can then realise either metallic or semiconducting dispersions as illustrated in Fig.3.4(c). This description is referred to as the zone-folding approximation [1]. In this scheme, therefore, whether a tube is metallic or semiconducting can be predicted from their chiral vector $\vec{C}_h = n\vec{a}_1 + m\vec{a}_2$ or rather indices (n, m) that describe the different ways of rolling a graphene sheet to form a nanotube as shown in Fig. 3.5.

The criteria for metallicity need to take into account curvature effects. It has been found that nanotubes that are predicted to be metallic by chirality considerations alone, often possess pseudogaps on account of curvature and defects such that truly metallic nanotubes are very rare [68]. When curvature effects are also taken into account, the truly zero band-gap nanotubes (or type I metallic) are armchair nanotubes ($n - m = 0$). Nanotubes where $n - m = 3i \neq 0$ are small tiny-bandgap semiconductor(or type II metallic) where i is a non-zero integer. The rest where

$n-m \neq 3i$ are semiconducting with a band gap that can be calculated from equation 3.2

$$E_g^1 = \frac{2\gamma_0 a_{cc}}{D} = \frac{0.7}{D(nm)}[eV] \tag{3.2}$$

where a_{cc} is the C-C bond length.

The band gap is found to be inversely proportional to its diameter as shown in Fig. 3.6. We see that for diameters closer to 10 nm the band gap will be so small that the tubes will exhibit metallic behavior at room temperature.

For the small(tiny)-band gap nanotubes where $m - n = 3i$, the curvature induced secondary bandgap depends on both the diameter and chiral angle θ is given by equation 3.3 [69].

$$E_g^2 = 3.1 cos3\theta \frac{a_{cc}^2}{D^2}[eV] \tag{3.3}$$

In quasimetallic zigzag nanotubes, $\theta = 0$ and the secondary gap is then given by 3.4

$$E_g^2 = \frac{3\gamma_0 a_{cc}^2}{4D^2}[eV] \tag{3.4}$$

where $\gamma_0 \approx 2.9$ eV.

Just like in large semiconducting nanotube, in small-gap nanotubes thermal energy at room temperature smears the bandgap making them exhibit metallic like behaviour.

It can be seen therefore that diameter is a crucial scaling parameter for the size of the bandgap of semiconducting tubes. Diameter also plays a role in determining the finite density of state (DOS) at the Fermi level $n(E_F)$ of metallic nanotubes as seen in equation 3.5 [69].

$$n\left(E_F\right) = \frac{2\sqrt{3}a_{CC}}{\pi\gamma_0 \vec{C_h}} = \frac{2\sqrt{3}a_{CC}}{\pi^2\gamma_0 D} \tag{3.5}$$

3.3.2 Gate-controlled conduction

As was discussed above, the SWNT can be either metallic or semiconducting, and the bandgap E_g of the latter given by equation 3.2. Unlike the metallic tubes, in the semiconducting tubes, the conduction can be strongly modified with an electric field from a nearby gate electrode, provided that the bandgap is large compared to

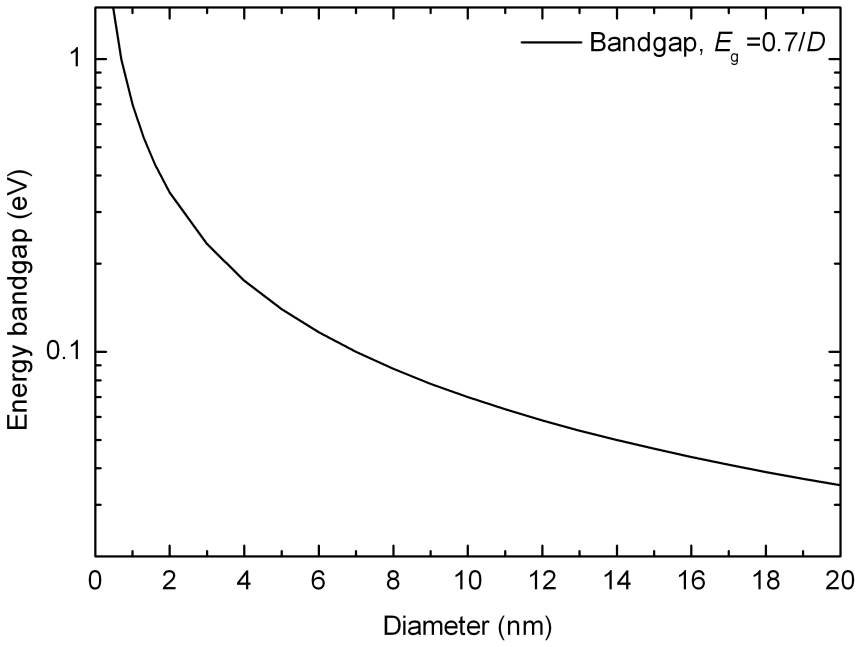

FIGURE 3.6 Tight binding model based calculated bandgap of semiconducting nanotubes as a function of diameter.

the thermal energy. We then have the CNT as a field-effect transistor, or CNT-FET. Most of our measurements reported in this thesis are gate response curves that show how conductance of the device vary with voltage applied from a backgate separated from the nanotube channel by the dielectric insulator SiO_2. This section is devoted to explaining how the backgate voltage shifts the band structure of a device and hence the conductance of the device.

In a nanotube device constructed as a field effect transistor one has two electric fields associated with electron transport; the drain-source biasing electric field and the electrostatic gating field. The bias voltage yields charge carrier propagation along the nanotube. They define chemical potential on the left and right side of the device. Typically, it has been concluded [70] that the valence band edge of a semiconducting CNT is close to the Fermi level of a metal electrode as shown in the band diagrams in Fig. 3.7(b). The gating field acts to lower or raise the band edges of a nanotube with respect to the Fermi level of the metal contacts. The negative gate voltages tend to align the Fermi level with the valence band thereby promoting hole injection into the nanotube leading to p-type behaviour manifested as an high conductance level, technically called ON state of a CNT-FET, on the left of the charge neutrality point. Positive gate voltages tend to move the conduction band in the center part of the device towards the Fermi level thereby promoting electron injection leading to n-type behaviour. The p-type and n-type ON states as well as the OFF state in between are illustrated in the gate curve shown in Fig.3.7(c). Since the valence band is close with the metal electrode Fermi level, the p-type conduction is typically higher than the n-type.

The OFF state equals the transport gap ΔV_G, which is the width of the off-state region (or low conduction region in gate curve). This transport gap, ΔV_G, is a very significant parameter in studies of electronic conduction in backgated low dimensional devices like nanotubes and narrow graphene nanoribbons as it is known to be related to an energy scale in the single particle energy spectrum given by equation [71], [72]:

$$\Delta_m = \hbar v_F \sqrt{(2\pi C_G \Delta V_G) \,/\, |e|} \tag{3.6}$$

where $\hbar$ is the reduced Planck constant, v_F is the Fermi velocity and C_G is the gate capacitance(Fig.3.8(b)).
By inducing p-type or n-type behaviour, electrostatic gating acts as a form of doping. The gate response that may be obtained depends, besides on obvious geometrical factors, on how this field doping competes which chemical doping of nanotubes by impurities and doping induced by substrates and adsorbed atoms from the environ-

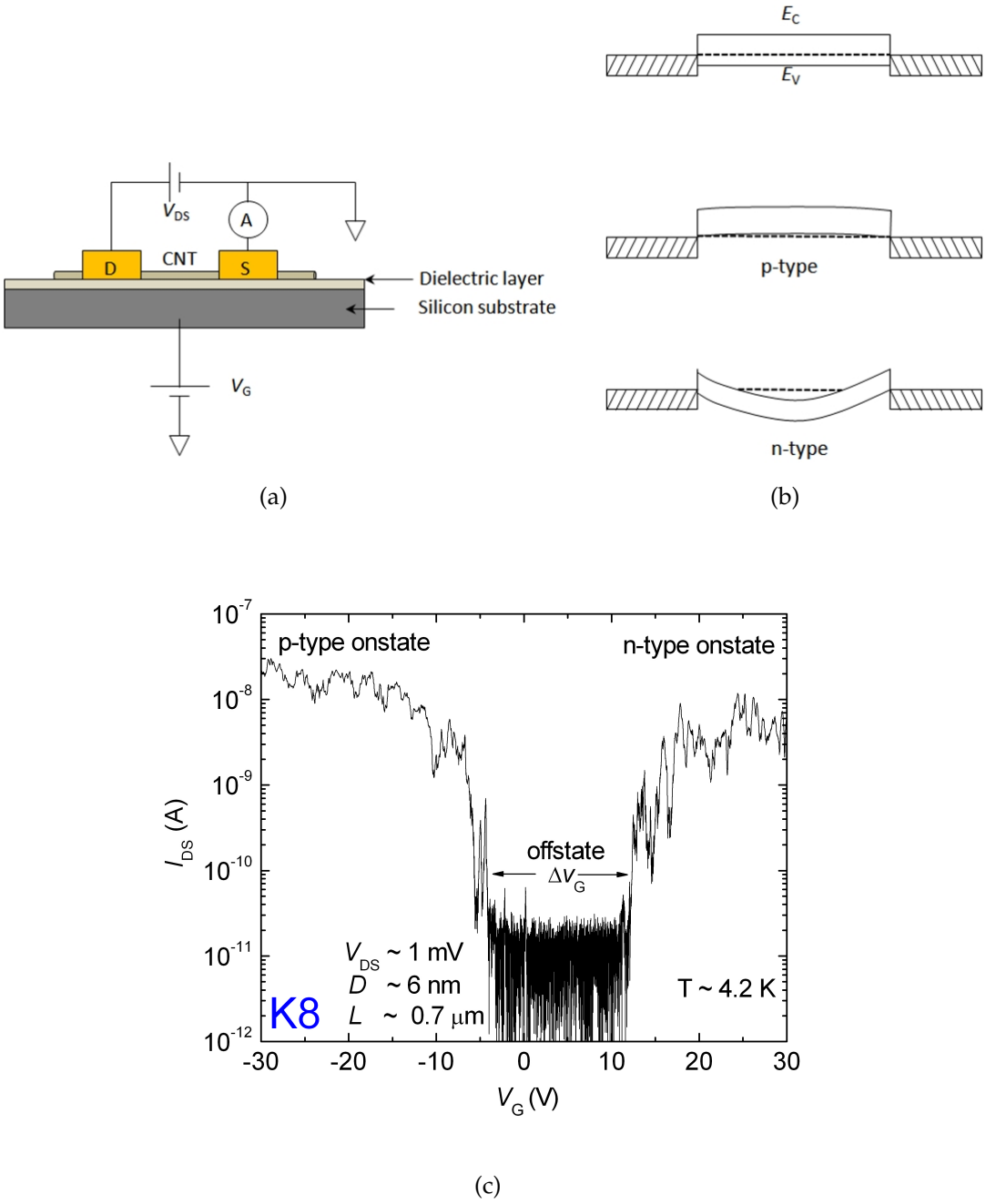

FIGURE 3.7 CNT-FET. (a) Schematic of a CNT between source and drain electrodes and a nearby gate electrode. (b) A corresponding energy diagram at different gate voltages in the case of a semiconducting CNT. (c) A typical gate curve measured in this work, showing ON and OFF states and a transport gap of width ΔV_G.

ment.

The temperature determines the energy level filling. The occupation probabil-

ity of the energy levels is a function of temperature as described by the Fermi-Dirac distribution function in equation 3.7.

$$f(E) = \frac{1}{exp(E/k_BT) + 1} \tag{3.7}$$

Considering the device scheme in Fig.3.7 above, the low-bias resistance maximum R_{OFF} within the transport gap could be expressed as thermally activated (equation 3.8) [73]:

$$R_{OFF} = R_C + \frac{1}{|\Gamma|^2}\frac{h}{8e^2}\left[1 + exp\left(\frac{E_g}{k_BT}\right)\right] \tag{3.8}$$

where R_C is the metal-tube contact resistance, $|\Gamma|^2$ is the transimission probability for electrons with energy $|E - E_F| > E_g$ to cross the gap.

This expression could be simplified by replacing the quantum statistics with a classical formula, namely with the Arrhenius-type behaviour (stemming from the Boltzmann distribution function):

$$R_{OFF} \propto \exp\left(\frac{E_g}{k_BT}\right) \tag{3.9}$$

Temperature also affects the mobility of charge traps responsible for gate curve hysteresis in CNT-FET devices. The temperature effect on hysteresis is usually seen in experiments as a strong gate response hysteresis at high temperatures and weak or not hysteresis at low temperature for non-passivated devices.

3.3.3 Transport regimes

Transport in nanotubes is probed by microsized metallic leads which are electronically 3-dimensional compared to the quasi-1-dimensional nanotube channel. Metal-carbon nanotube junctions are known to exhibit lowered transmission probabilities $|\Gamma|^2$<1 due to symmetry mismatches for incoming and outgoing states at interfaces or presence of Schottky barriers [1]. The later is usually the case in metal-semiconductor nanotube junctions. If contact resistance is taken into account the resistance of a nanotube device is a sum of the intrinsic tube resistance and the contact resistance given as [68]:

$$R_{device} = R_C + R_{tube}. \tag{3.10}$$

The resistance of a nanotube (R_{tube}) depends on how the spacing of electrodes (L) of the sample compares with some characteristic length scales which are signatures of scattering processes encountered by charge carriers in the sample [74]. In

discussing transport in carbon nanotubes the important length scales to be considered are elastic mean free path L_{mfp}, localization length L_o, phase coherence length L_ϕ. Localisation length is associated with elastic scattering on impurities without loss of phase, whereas the phase coherence length is associated with inelastic scattering that lead to phase decoherence. Depending on how the length of the sample compares with such characteristic length scales one can have coherent ballistic transport, diffusive transport, strong (Anderson) localization behaviour and classical (incoherent) transport regimes [74], [75]. Typical scattering processes include electron−phonon scattering, electron-defect or impurity scattering. There can also be electron−electron interactions in the sample that can lead to Luttinger-liquid like behaviour.

Ballistic regime

Ballistic transport refers to propagation of electrons without scattering in the nanotube. This occurs when the length of the nanotube (L) is less than either the localization length (L_o) or the phase coherence length(L_ϕ). This means that there is no voltage drop along the nanotube and thus no resistance in the nanotube itself. However there is voltage drop at the electrode-nanotube contact, associated with a jump in chemical potential differences between the nanotube and the electrodes, leading to a resistance given by the Landauer equation 3.11 [68].

$$G = \frac{4e^2}{h} \sum_i \int_{\infty}^{-\infty} \frac{df\left(E - E_F\right))/k_B T}{dE} \Gamma\left(E_F\right) dE \tag{3.11}$$

where $\Gamma(\mathrm{E}_F)$ is the transmission probability of the ith 1D subband at Fermi level and $f(E)$ is the fermi occupation function. For contacts with perfect transmission, this expression simplifies to:

$$G = N\left(\frac{2e^2}{h}\right) \tag{3.12}$$

where N is the number of channels. In a single channel conductor (N = 1), R_Q $\approx 13k\Omega$ is the inverse of the quantum conductance G_q [74]. Since carbon nanotubes are generally considered as purely or quasi-one dimensional structures, and in some cases rather free from defects, the resistance of a nanotube can be in a SWNT, with N = 2, very close to the two-channel quantum conductance of $\approx 6.5k\Omega$.

Diffusive regime

When inelastic electron-phonon interaction becomes dominant phase coherence length of a nanotube becomes smaller than both localization length and length of the sam-

ple. Electrons propagate diffusively along the sample leading to Ohmic-like transport behaviour with resistance scaling linearly with length. In systems where diffusive transport is more dominant conductance G can be expressed as in equation 3.13, where L_{ie} is the inelastic scattering length [1].

$$G = \frac{(2e^2)}{\hbar}\frac{L_{ie}}{L} \tag{3.13}$$

At high bias there can be deviations from the ohmic like behaviour [74].

Strong localization regime

In unclean nanotubes with large number of impurities and defects the electron wavefunction can be 'completely halted' or localized by the random potential of the defects and impurities. This is called the strong (or Anderson) localization regime. Transport of electrons in this regime is by means of tunneling processes, that is, hopping conduction. The resistance of the nanotube becomes exponentially dependent on length [74].

Considering these many possible regimes a discussion of electron transport need to provide information on the structural cleanliness of the samples, the measurement temperature and the bias voltage regime. In Fig. 3.1 the criteria used to determine the transport regimes of samples of length L is summarized [1], [55].

3.3.4 Coulomb blockade regime in carbon nanotubes

Under certain conditions a nanotube device may behave as a quantum dot (or an island) weakly coupled from leads by tunneling barriers as shown in schematic in Fig.3.8(a) (a). When tunneling resistance is greater than quantum resistance, and the charging energy due to excess electrons added to the island U$\approx e^2/2C$ is greater than thermal fluctuations (k_BT), single electron tunneling and blockade events can occur across the barrier [Grabert and Devoret]. This is usually manifested as oscillations in conductance in gate modulated conductance curves with periodicities that depend on the charging energy U$\approx e^2/2C$. The capacitance C is sum of the capacitances C_D, C_G and C_S shown in the single quantum dot circuit diagram in Fig. 3.8(b) [5], [76].

3.3.5 Magnetic field effects

From the discussion above we see that electrostatic gating field and temperature are important transport probes and are at the heart of experimental studies of elec-

Transport regime	Condition	Conductance expressions
Ballistic	$L_o, L_\varphi > L.$	$G \approx \frac{4e^2}{h}$
Diffusive	$L_\varphi < L, L_o$	$G \approx \frac{2e^2}{h}\frac{L_{ie}}{L}$ $G_M = \left(\frac{\pi Dn}{L}\right) e^2 K_d v$
Strong (Anderson) localization	$L_o < L < L_\varphi$	$G \approx \left(\frac{2e^2}{h}\right) \exp\left(-\frac{L}{L_o}\right)$
Classical (Incoherent)	$L_o, L_\varphi << L$	$G \approx \sigma\left(\frac{w}{L}\right)$

TABLE 3.1 Transport regimes and corresponding conductance expressions [1]. The second equation in the diffusive row applies to MWNTs [55]. In this equation $K_d = v_F \lambda_F / 2$ is the diffusion constant, and D is averaged diameter while n is the number of walls.

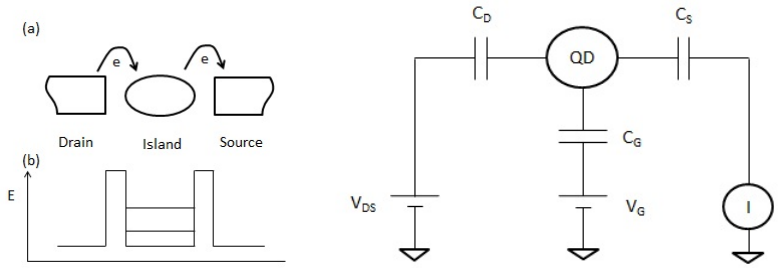

FIGURE 3.8 (a) Schematic of single electron transistor (drain, island, and gate) and a corresponding energy diagram showing tunnelling barriers and single particle states of a quantum dot. (b) Circuit model showing a single quantum dot and circuit capacitances.

tron transport in both nanotubes and other mesoscopic materials. Another important probe worth mentioning is magnetic field. Magnetic field is known to lead to many effects on transport in nanotubes depending on how the field is oriented with respect to the tube axis. A parallel magnetic field add a Berry phase (or rather the Aharonov Bohm phase) to the propagating electron wavefunction and can lead to opening up of bandgaps in otherwise metallic nanotubes.

The Aharonov Bohm effects can be measured experimentally as fluctuations

in conductance when plotted against magnetic field [52], [77]. Such fluctuations are important probes for diffusive quantum transport in carbon nanotubes with typical signatures being weak localization and Altshuler-Aronov-Spivak oscillation for interference of a pair time reversed paths as well as universal conductance fluctuations (UCF) for interference of different paths [56]. Magnetic field can also induce splitting of spin-orbital degeneracy. Perpendicular field on the other hand can lead to formation of Landau-levels manifested as peaks in the vicinity of the charge neutrality point in the density of states vs E plots [1]. The extent of magnetic field effects depends the strength of the field and is usually more pronounced for higher fields where magnetic lengths l_m are comparable to electron mean free paths l_e.

3.3.6 Transport in multiwall nanotubes

The theory of transport discussed so far is generally true for SWNTs but not fully consistent with transport in MWNTs. However, the transport theory in SWNTs provides a a good foundation for discussion of transport in multiwall nanotubes since a multiwall nanotube is comprised of many nested single wall nanotubes and is itself also a quasi-one dimensional structure just like a SWNT. To see the role of inner walls on transport we have to examine the measurement electrode geometry and the electronic structure of the multiwall nanotube.

Transport in a non cap-ended multiwall nanotubes can be measured in two ways, either by side contacts which only make a wet contact to the outer wall or by end-contacts. In the latter case, if all shells of the multiwall nanotubes are similary coupled to the electrode, conductance will in principle be the sum of conductance of all the current carrying channels. For the side contacted case, which happens to be the common experimental technique, transport is assumed to be dominated by the outer shell and the weak intershell coupling is often neglected. The question as to whether the inner walls (shells) have any influence on electrical conductance becomes reasonable when one considers the interwall separation of 3.4 Å, much larger than the intratube C-C bond length of c. 1.42 Å.

The first approach to determine the effect of intershell interaction is to estimate the strength of the intershell interaction and compare it with intrashell energy parameter. The Hamiltonian of a multiwall system, in a simplified tight-binding model that assumes one out-of-plane orbital per C atom, zero onsite-energies and constant nearest neighbor hopping on each wall and an intershell hopping $\pi - \pi$ coupling is given by equation 3.14 [1].

$$H = \gamma_0 \sum_{i,j} \left|p^j\perp\right\rangle \left\langle p^i\perp\right| - \beta \sum_{i,j} cos\left(\theta_{ij}\right) e^{-(d_{ij}-a)/\delta} \left|p^j\perp\right\rangle \left\langle p^i\perp\right| \tag{3.14}$$

where β is the interwall coupling, θ_{ij} is angle between $p^i\perp$ and $p^j\perp$ orbitals and $\delta \approx 0.45$ Å and a = 3.4 Å [1].

First principles ($ab\ initio$) calculations by Lambin *et al.* [78] show that β is nearly 0.36 eV which is nearly one-eighth of hopping parameter ($\gamma_0 \approx 2.9$ eV). This allows redistribution of waves packet between neighbouring shells and thus raising the possibility of intershell transport [1]. This weak interwall coupling is known to influence physical properties of DWNT nanotubes [79].

Further, theoretical studies of density of states of DWNT and TWNTs (triple wall carbon nanotubes) have shown that the presence of inner walls may change the density of state of the outer shell. This has been confirmed by several experimental Scanning tunneling microscopy (STM) measurements [1]. One interesting case was seen in DOS studies of DWNT made up of two metal armchair shells (5,5)@(10,10) where a gap opens making the nanotube semiconducting [1].

In MWNTs of more than 3 shells the structural complexity can be severe on account of many possible assignments of helicities of the constituent shells. In regard to different chiralities multiwall nanotubes can be classified as either commensurate or incommensurate. Commensurate MWNTs exhibit translational invariance are therefore periodic objects in the radial direction whereas incommensurate MWNTs are not periodic. Statistically incomensurate systems should be more common.

Both DWNTs and TWNTs are a good starting point for studies of electron transport in multiwall nanotubes. This is justifiable in light of experimental studies that have shown that about 5 outer shells can contribute significantly to transport [80] and also considering that electrostatic interactions of outer shells decay as $1/r^2$. Furthermore, the first inner wall may screen off the effect of deeper inner walls. However, any wall can potentially affect the DOS of the next wall, so deep wall influences may surface out to outermost walls in a domino effect. This is evidenced by differences in TWNT and DWNT effects on density of states [1].

It is good to note that the effects are Fermi energy dependent so bias level, temperature, as well as defects play a big role. Theoretical studies for TWNTs predict that in defect-free commensurate MWNTs transport is ballistic at all Fermi energies whereas in incommensurate TWNTs nanotubes transport is diffusive with conductances and diffusion that have power law behaviour. Furthermore, in incommensurate TWNTs with outer metallic shell anomalous conductance-length dependence at higher Fermi energies ($E \approx 0.5\gamma_0 \approx 1.5eV$) have been numerically predicted as given in equation 3.15)

$$G = \frac{2e^2}{\hbar}\left(\frac{L}{L_0}\right)^{\frac{(\eta-1)}{\eta}} \tag{3.15}$$

where η is an exponent that depend on both the fermi level energy and helical symmetries of the MWNT [1], [81].

In light of the complexity of transport exhibited in DWNT and TWNTs, the task of studying MWNTs becomes a forbiddingly daunting task. Our work on MWNTs nanotubes provides a catalogue of transport scenarios that one can meet in nanotubes with outer diameter 3-10 nm. A complete experimental study of MWNT would require intrusive structural studies that would provide chiralities of each shell. One way around this problem could be to fabricate multiwall nanotubes of well defined chiralities. This is a synthesis challenge - and also a holy grail of carbon nanotube research. In the next section 3.3.7 we examine many experimental works reported in the MWNT literature, mainly on study of intershell transport and effects of interwall coupling on outershell dominated transport. A discussion of large diameter multiwall nanotubes is also included.

3.3.7 Existing experiments on multiwalled nanotubes - Literature review

From a literature review of many transport studies we found that most of experimental works on nanotubes have been done on small diameter SWNTs (1-2 nm) due to their simplicity in structure and their large bandgap that suits room temperature field effect transistor applications. A review of articles on low temperature transport studies in MWNTs show that many works focussed on diameter in the large diameters range D > 10 nm and not much work has been done in the intermediate diameter range 3-10 nm. The main reason for the overwhelming concentration on higher diameter MWNTs (D: 10-30 nm), is that intermediate sized nanotubes were rare due to synthesis issues. The other reason for a bias towards a higher diameter range was the desire to use parallel magnetoresistance - larger nanotubes respond well to moderately high externally applied magnetic field (B:10 T to 30 T) available in many labs where as small nanotubes would require 100 T to 1000 T which are difficult to produce in a lab. A flux linked to a nanotube is proportional to cross-

Nanotubes in the range of diameters 3-10 nm, tend to have less band gaps compared to semiconducting SWNTs and are not very attractive for practical room temperature FET applications. However MWNTs of this diameter range have their own merits and their transport properties need to be understood. The MWNTs in the lower diameter range usually have few shells and are structurally relatively cleaner than large MWNTs whose outer walls may be covered with amorphous carbon. Despite their complexity MWNTs are still attractive for applications due to bending strength and high current carrying capacity. It is therefore important to understand

how charge is transported via devices made of MWNTs. Such studies can also provide insight into the role of inner walls and various wall-wall arrangements.

Before addressing transport in intermediate sized nanotubes and intershell transport, let's first review low temperature transport studies in large diameter nanotubes (10 nm to 40 nm). Most of the works in this diameter range have shown that MWNTs exhibit mostly diffusive electronic conduction due to structural disorder, as has been reported in several works [82]. The diffusive transport has been examined more extensively with magnetic field dependent measurements yielding Aharonov Bohm effects [52] such as weak localization, AAS behaviour and universal conductance fluctuations. Other temperature dependent transport studies on metallic multiwall nanotubes have studied Luttinger liquid behaviour [54] with power law behaviours $G \propto T^x$ with x varying from 0.12 to 0.3.

There have been some experimental studies on the role of inner shells in a multiwall nanotube structure. The most significant of these is the work aimed at determining the intershell conductance [83] which provide good evidence for intershell transport. In other transport works the number of shell that contribute to conductance in nanotubes has been counted [80].Various techniques have been employed such as peeling off parts of outer shells or breaking down shells sequentially [80] by application of high bias voltages. Other transport works include works by Krstic *et al.* [84]. Another significant work was on use of electron diffraction to characterize chiral indices of individual walls [85].

There have also been some studies concerning temperature dependencies of ON state conductance of say two sections of nanotube of different length [33] but such studies did not address the offstate conductances. We have systematically studied the temperature and size dependence of both on-state and offstate conductance adequately in nearly 100 samples. A few notable works on size dependence has been length dependence studies by scanning conducting AFM tips across the nanotube [86], [74]. Although these measurements have been rich in length data points they have severely lacked temperature dependence data and have generally reported lower contact resistances than our palladium metal-on-tube architectured nanotube devices.

3.3.8 Electron transport in Graphene nanoribbons

At the onset of a theoretical discussion of transport in nanotubes in section 3.3, graphene was mentioned as a gapless material which can be rolled to form nanotubes of either semiconducting or metallic conduction properties. In this section

we discuss the evolution of bandgaps when graphene is sliced into narrow ribbons of nanoscale width (i.e nanoribbons)in view of recently reported transport works on graphene nanoribbons that have shown temperature-dependent gate-modulated transport similar to our experimental results in intermediate sized multiwalled carbon nanotubes [87], [72], [71], [63]. Of interest to us is the range of width of the graphene nanoribbons ($20 < W < 120$ nm) that corresponds to circumference of wrapped graphene cylinders (or nanotubes) of diameters in the range 6.5 nm to 38 nm.

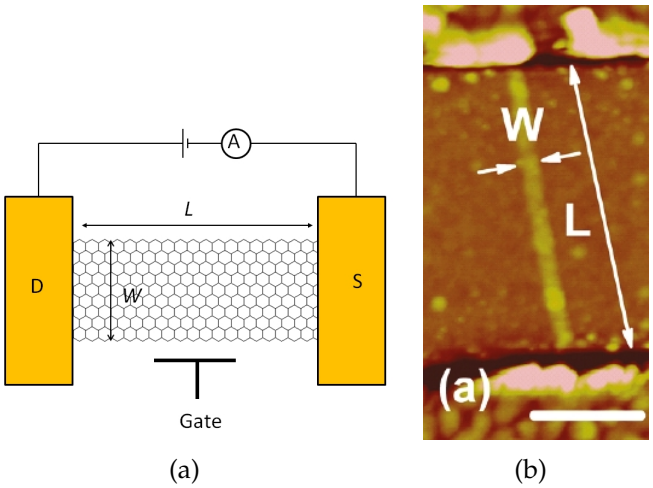

FIGURE 3.9 (a) Schematic of a graphene nanoribbon device of width W and channel length L. (b) A typical narrow GNR sample in literature [88]. The scale bar is 300 nm

The gapless nature of graphene arises due to linear energy dispersion near the charge neutrality point also know as the Dirac point. Charge carries can propagate through the graphene sheet as massless relativistic fermions. However, when graphene is sliced into nanoribbons the charge carriers become confined into a quasi-1D system and this leads to formation of gaps. Since lithographically fabricated GNRs have disorder, the central question is whether the transport gap in such GNRs is a simple gap, or is due to edge disorder induced Anderson localization, or Coulomb blockade in quantum dots formed in series on the GNRs [87], [72]. Systematic studies of width and length dependence of transport in GNRs can help to address this question.

Notable work in narrow nanoribbons has been the work of Han *et al.*, in which bandgaps ranging from 3 meV to 350 meV for GNRs of width 90 nm to 15 nm were measured by reading the width of Coulomb diamonds on the bias voltage axis of low temperature plots of conductance versus voltage and gate voltage [87]. These bandgaps fitted to an empirical scaling law $E_g = \zeta/(w - w*)$ with ζ = 0.2 eV nm where w is the nanoribbon width and w* is a fitting parameter. This inverse width

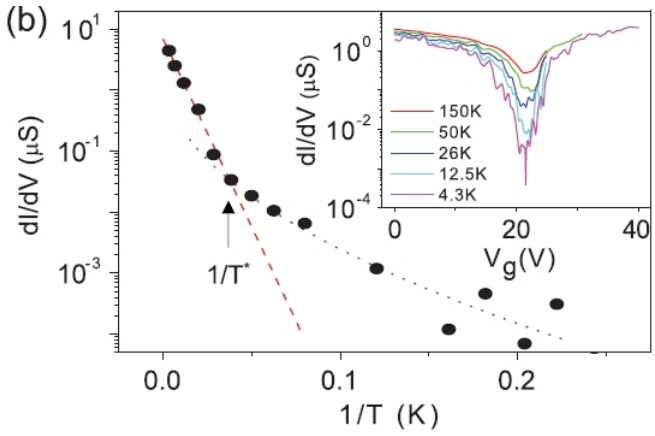

FIGURE 3.10 Gate-controlled transport in a graphene nanonorribon of width 36 nm studied by M.Han *et al* [72].

scaling of GNR bandgaps is analogous to the inverse diameter scaling of bandgaps in nanotubes [1] as was shown in Fig. 3.6. The work on GNRs has shown temperature dependences of minimum conductance at gate voltages near the charge neutrality point, as shown in Fig3.10, similar to what we have observed in transport gaps of our MWNT samples reported in this thesis. Transport gaps ΔV_G are seen to be more pronounced as temperature was lowered and and are generally wider for narrower ribbons and absent in wider nanorribons even at low temperature.

Many temperature dependent studies of offstate minimum conductance on GNRs have reported Arrhenius activated transport behaviours at temperatures near 300 K and hopping transport at low temperature.

Length scaling has been explored in very few works [88], [72], mainly disordered graphene nanoribbons. It is not surprising, therefore, that in one of these works [88] exponential length dependence of room temperature onstate and offstate resistance was observed in single layer graphene nanoribbons of width 40 nm. In the same work bilayer graphene nanoribbons exhibited linear length dependence of room temperature resistance. In the other work [72], nonlinear I-V gaps (ΔU_B) were found to scale with length at low temperature. However, fields ($\Delta U_B / L$) calculated from the nonlinear I-V gaps were found to be independent of length.

Related to the issue of interwall effects in DWNT and MWNT was a recent study on bilayer graphene nanoribbon(BLG) [88]. Such studies of transport in bilayer and multilayer graphene nanoribbon structures present one way to examine effects of interwall interactions in DWNT and MWNT and a direct measurement of interlayer tunneling conductance. However, edge effects may play a role in such multilayer GNR's.

Chapter 4

Sample fabrication and measurement methods

In this thesis work we fabricated hybrid polypyrrole-gold samples and backgated carbon nanotube devices with geometries as shown schematically in Fig. 4.1 and measured electron transport properties of these samples using a two-probe technique. In this chapter fabrication, imaging and measurement techniques common to both polypyrrole-gold and nanotube samples in this thesis work are discussed. These include fabrication of microelectrodes via electron beam lithography, atomic force microscopy, scanning electron microscopy and electrical measurements. Specific details that apply only to the PPy-Au devices are discussed in Chapter 5. In Chapter 6 are discussed issues regarding nanotube materials and specific measurements of multiwall nanotubes.

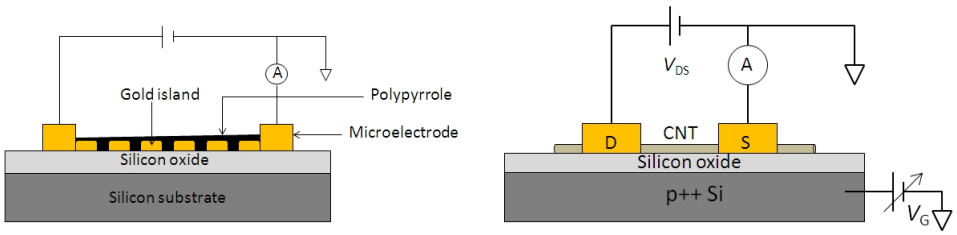

(a) (b)

FIGURE 4.1 (a) PPy-Au hybrid device.There is an ultrathin (2nm)Ti adhesion layer under the electrode of the PPy-Au device. The Au islands are contacted directly to the oxide layer. (b) Back-gated carbon nanotube device. The nanotubes are contacted with Pd metal only.

4.1 Fabrication of microelectrodes

Silicon substrates

We fabricated all samples on silicon substrates. Since some electron transport studies in this work involve measuring current as a function of backgate voltage at various temperature, a good substrate which remains highly conducting even at cryogenic temperatures (down to 100 mK) is needed. For this purpose we chose a highly (or degenerately) boron-doped silicon wafers with room temperature resistivity of 0.05 Ωm. The silicon wafers were then dry-oxidized (under oxygen flow) at 1200 ^{o}C for 6 hours to achieve a thickness of 300 nm in a local oxidation chamber shown in Fig. 4.2(a). The oxide thickness was measured using a laser ellipsometer shown in Fig. 4.2(b) and color charts were used to ascertain the thickness values from the ellipsometer. Before any oxidation we ensured that the wafers were thoroughly cleaned with acetone and then isopropanol to get rid of dust particles that are known to cause pinholes which lead to current leakages. Current leakage tests on the oxide involved deposition of two adjacent 25 nm thick gold layers via a detachable aluminum mask and quick resistance measurements using a digital multimeter and soft titanium probes. The wafers were then diced with a diamond saw into 5 mm x 5 mm chips.

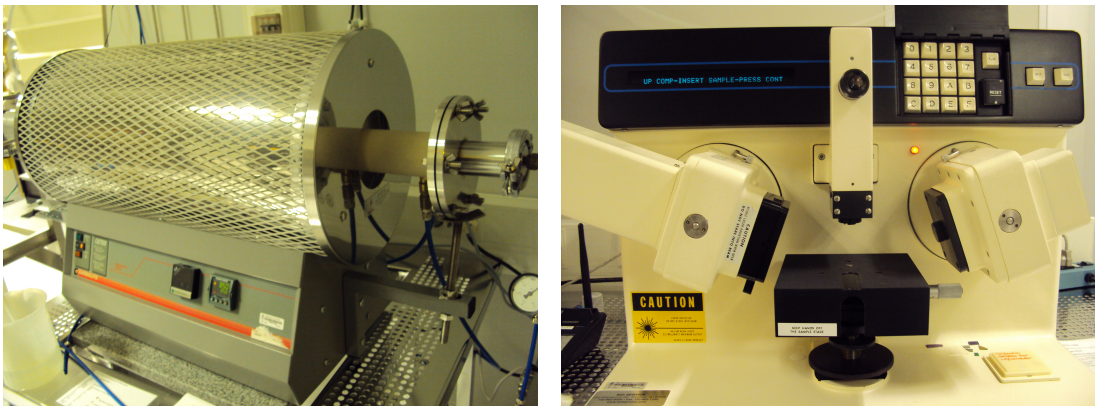

(a) (b)

FIGURE 4.2 (a) Oxidation furnace used to oxidise silicon wafers. This instrument is equipped with a PID temperature controller. During oxidation the sample is placed in the mid of the chamber which is the hottest part of furnace. (b) Elipsometry equipment used to measure thickness of thermally grown silicon oxide.

Electron beam lithography

Electron beam lithography technique was used to fabricate microelectrodes on the silicon oxide substrate as illustrated schematically in Fig. 4.3. In this lithography process an electron beam is scanned along a positive resist coated surface to draw (expose) lines and areas defined by the design pattern (Fig. 4.3(b)). The electron beam causes chain breaking or scission of the resist polymer thereby forming a latent image. The exposed areas can easily dissolve in a suitable solvent thereby leaving lithographic lines. In fabrication of our samples two layers of a positive resist were deposited on a substrate by spin coating(Fig. 4.3(c)). The 'softer' bottom resist layer was made from a solution of 495 polymethylmethacrylate (PMMA) dissolved in anisole (3 percent solids in anisole) and the top resist layer was made of 950 PMMA dissolved in anisole (2 percent solids in anisole). The thickness of the PMMA layers is determined by the spinning speed and the PMMA concentration. The layers were typically 50 nm and 100 nm respectively. The resist was then baked at 160 ^{o}C for 4 minutes and then exposed with an electron beam of dosage 300 μC/cm^2 and acceleration voltage of 30 kV. The sample was then developed in methylisobutylketone in Isopropanol (MIBK:IPA) which dissolve the exposed resist areas and leaves the unexposed areas intact. Use of a 'softer' bottom resist layer (PMMA:EL3) ensures that there is enough undercut after sample development which promotes easy liftoff after metallization. The samples after metallization and liftoff look like shown in (Fig. 4.3(d)) and (Fig. 4.3(e)). Reactive ion etching (RIE) was used to remove residual resist from lithographic lines.

Electrode deposition

Metallization of gold electrodes for PPy-Au samples and palladium electrodes for nanotube samples was accomplished using an ultrahigh vacuum ($P \approx 10^{-8}$ mBar) electron beam evaporator shown in Fig. 4.4. The evaporation rate was 0.1 nm/s. The UHV evaporator is equipped with a calibrated quartz crystal monitor which measures the thickness of deposited layers. For the PPy-Au samples a 2 nm thin layer of titanium which acts like an adhesion agent is deposited first before deposition of 25 nm thick layer of gold. This titanium layer protects the electrodes from peeling off when subjected to ultrasound, thermal, or other stress. For the nanotube samples the palladium electrode is contacted directly to the nanotube. Pd is a metal known to make good (ohmic) contacts to nanotubes [89] [33].

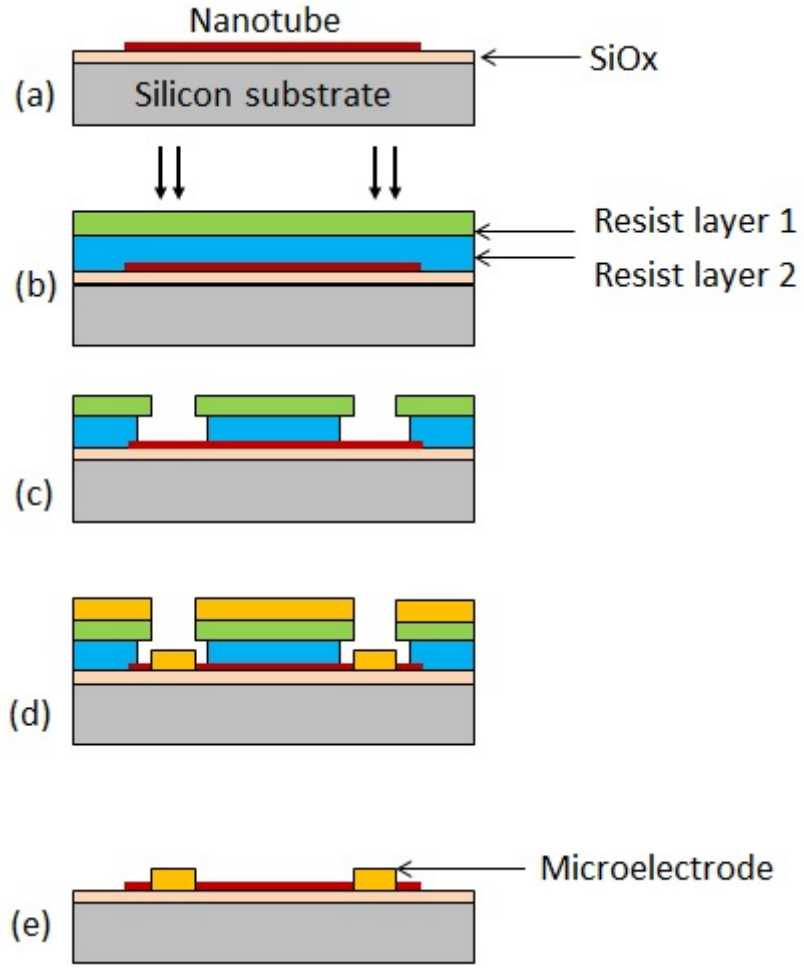

FIGURE 4.3 Schematic shows a fabrication procedure of microelectrodes on a CNT using electron beam lithography. (a) Deposition nanotubes on a substrate. (b) Deposition of a double layer PMMA resist and electron beam exposure. (c) Development. (d) Deposition of metal. (e) Sample after liftoff.

4.2 Characterization and measurement techniques

Atomic force microscopy

A Veeco atomic force microscope (AFM) instrument shown in (Fig. 4.4(b)) was used to measure diameters of carbon nanotubes and thickness of polymer-gold samples. This AFM instrument has a specified height measurement accuracy of 0.1 nm. This AFM instrument was also used for imaging of both MWNTs and PPy-Au samples and also for sample mapping essential for accurate positioning of microelectrodes onto nanotubes.

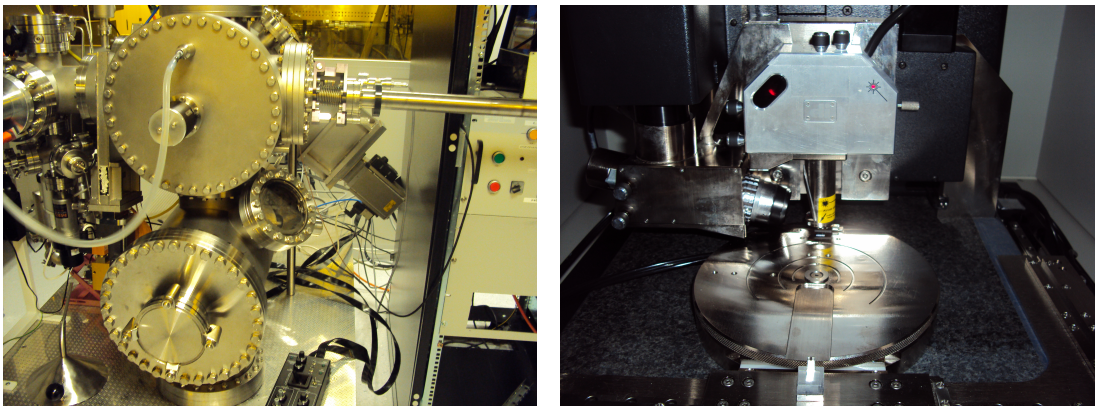

(a) (b)

FIGURE 4.4 (a) Ultrahigh vacuum electron beam evaporator used for metallization of samples. (b) Atomic force microscope (AFM) instrument used to measure thickness of the polypyrrole-Au films, sample mapping of nanotube samples and measurements of nanotube diameters.

Cryogenics

After imaging of devices the chip is attached to a chip carrier using GE varnish and leads are attached to the bonding pads of the sample using an ultrasonic bonder. During wire-bonding the bonding pads on the chip carrier are grounded to avoid electrostatic discharge (ESD) damage . Current leakages via backgate are tested. The sample yield was less than 70 percent due to fabrication damages of electrodes, leakages, or accidental ESD damage. The chip carrier is then mounted on a stage of a liquid helium cooled 4 K dip-stick cryostat and is sealed in a vacuum can using indium wire. A rough pump and a diffusion pump is used to create a vacuum ($< 10^{-3}$ mBar) in the vacuum can. This helps to get rid of gases and moisture that can dope the samples. When placed in a liquid helium dewar a temperature range of 4 K to 280 K can be accessed for temperature dependence studies. For sub-Kelvin low temperature measurements we used a homemade plastic dilution fridge with a base temperature of 50 mK. The 4 K cryostat is equipped with a silicon diode temperature sensor purchased from Lakeshore, whereas in the plastic dilution refrigerator (PDR) there is a Cernox Germanium resistance temperature detector (RTD) inside the mixing chamber (coldest part). For the temperature sensor of the 4 K cryostat (silicon diode sensor), we used a four-probe technique in which a 10 μA current was applied from a Keithley current source and the voltage across the sensor was read. The voltage output is passed through a pre-amplifier to filter out noise and interferences before reading it with a data acquisition device (DAQ). The gain of this pre-amplifier stage was unity. The RTD sensor can measure tem-

peratures from 300 K to 10 mK reliably. The resistance of the Cernox element was measured by a resistance bridge and a Cernox software was used to convert the resistance to temperature. A copper strip was used was used for thermalization of the sample and the mixing chamber. This was checked by mounting a Cernox sensor on the sample and measuring temperatures of the mixing chamber sensor and the sample sensor. The difference was tens of mKs. This was sufficient since the temperature dependence of interest in our samples is studied over a wide temperature range in steps larger than 100 mK.

Electrical measurements

Two-probe measurements are performed by applying dc voltages from a Yokogawa voltage source to the nanotube device drain electrode and measuring the drain-source current. The gate voltage is supplied by another Yokogawa dc source. Fig. 4.5(a) shows schematically how various measurement instruments shown in Fig. 4.5(b) are connected to the sample and a measurement computer. Computerized data acquisition and control was accomplished using LabVIEW software. The two dc sources are controlled remotely via a general purpose interface bus (GPIB) which is connected to an NI-GPIB card. The voltages and currents are measured by an NI-DAQ which has an ADC. The DAQ is connected to the measurement computer via a multifunctional 16-bit NI-PXI 6081 and digital data is sent to the measurement computer via optical fiber which is immune from pick-up noise. We used LabVIEW software to set and control voltage sweeps as well as to record and display the current-voltage data.

Since the drain-source currents are very low (< $1\mu A$), we measure them using a low noise current amplifier which gives a voltage output proportional to the current. The current sensitivity S setting of the amplifier defines the threshold noise level in the measurements (i.e 200 pA for $S \approx 1\mu A$/V), 20 pA for $S \approx 100$ nA/V, 2 pA for $S \approx 10$ nA/V and 200 fA for $S \approx 1$ nA/V. The gate curves with onstate current near 100 nA have a threshold current of 20 pA in the offstate. If one tries to calculate offstate resistance from a gate curve measurement, this 20 pA gives a value 50 MΩ for 1 mV bias voltage. This is not a true resistance of the sample but rather the amplifier noise at that particular sensitivity setting. To measure high resistances (R > 50 MΩ) correctly, we use slowly scanned IV curves and calculate the slopes in the low bias regimes. For nanotube samples, gate voltage V_G was scanned from -20 V to 20 V and for some samples -30 V to 30 V corresponding to electrostatic field of $\approx 10^8 Vm^{-1}$. The current was kept below 1 μA to avoid self-heating and damage to samples.

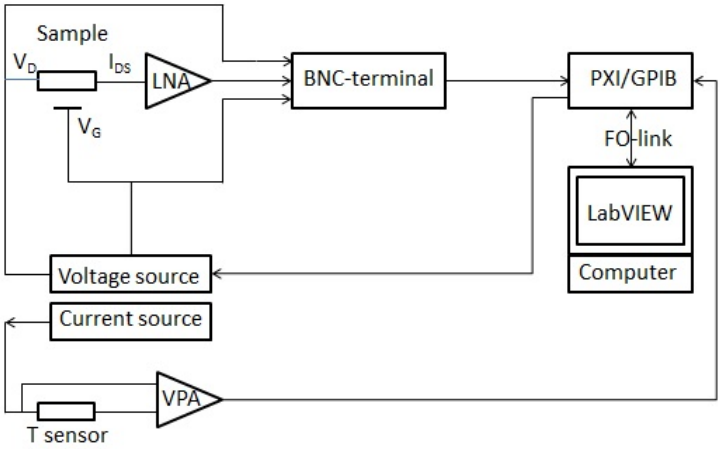

(a)

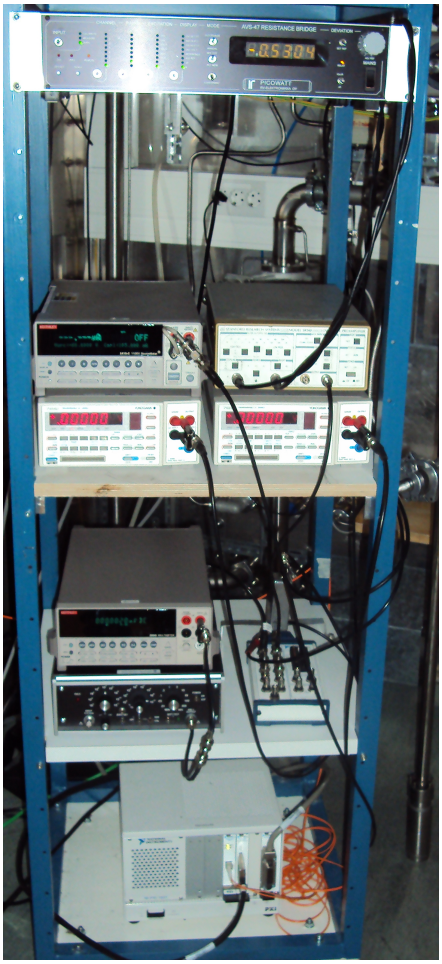

(b)

FIGURE 4.5 Electrical measurement set up (a) Measurement schematic showing how different measurement instruments are interfaced. (b) Measurements instruments on our measurements rack. From top to bottom left to right are: Resistance bridge, Keithyley voltmeter, SRS voltage preamplifier, Yokogawa DC voltage sources, LN1211 low noise current amplifiers, BNC connector box and data acquisition devices (DAQ) with a PXI and a GPIB card. The 4 K dipstick is shown on the right side of the rack.

Chapter 5

Mesoscopic conducting polymer devices

5.1 Novel fabrication concept: Nanoscale hybrid PPy-Au device

In this thesis I present a concept for creating mesoscopic conducting polymer devices which has no precedents except for a few previous work with similar fabrication ideas. The central idea is presented in Fig. 5.1.

A discontinuous film of gold is placed between two electrodes as shown in Fig.5.1(a). The gaps between the gold islands are very small, also compared to the islands. In Fig.5.1(b) an electrolyte containing the oligomer constituents of an electrochemically growing conducting polymer is covering the gold island layer. A voltage is applied between the electrodes and the polymer begins to grow from one of the electrodes. It grows extraordinarily quickly along the island layer, as pictured in (b) as the growing polymer film connects from one island to the next, which then effectively become part of the growth promoting electrode. The end result is a polymer film that covers the whole gold island layer, as shown in (c), and which is uniform but for a certain thickness gradient. Moreover, the polymer film thickness is larger than the island layer thickness with at most a factor of 10, so the islands may play a crucial part in the conductive properties of the device. The structure would then essentially be a hybrid PPy-Au device.

Since the island size can vary from a few tens of nanometers to hundreds of nanometers polymer growth initiated at anode can reach several microns away in a few seconds while the polymer/metal film thickness is still a few tens of nanome-

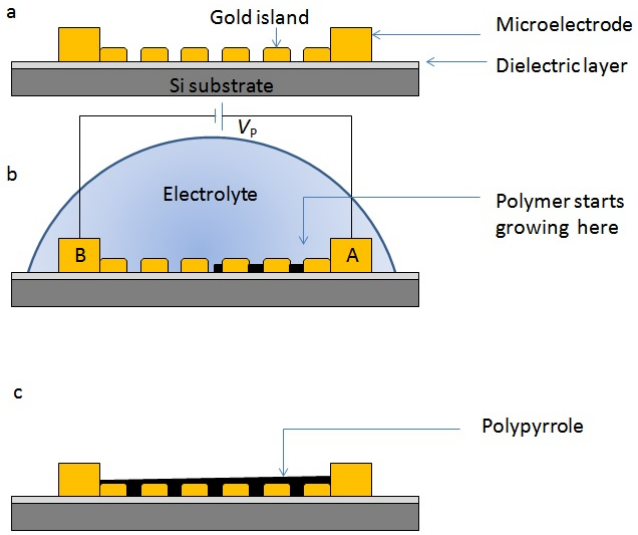

FIGURE 5.1 Schematics of polymer film growing on discontinuous gold film. (a) We start by fabricating a plain gold film (b) Electrolyte droplet is then placed on gold film and a voltage of 2 to 4 V is applied across the film. Polymers starts growing from anode and proceeds towards the cathode. (c) Polymer on a gold film after removal of electrolyte.

ters. Using this technique we have been able to fabricate hybrid Polypyrrole-gold (PPy-Au) nanostructures of thickness 10 nm to 200 nm and of length and width 1- 5 μm on insulating substrates. This technique also provides an opportunity to study polymers at short length scales corresponding to nanoscale inter-island spacing of ultrathin gold films. The width of the PPy-Au film is defined by the width of the underlying Au islands layer and can be scalable to 100 nm if small Au islands can be deposited in lithographic lines. The thickness of the polymer can be controlled by synthesis duration.

5.2 Ultrathin gold films

To achieve rapid lateral growth of polymer film on insulating substrates as discussed above, we need discontinuous metallic films. Such are simply created by depositing ultrathin films such that the nanoscale inter-island spacing is not filled up. Ultrathin gold films are usually fabricated using electron beam evaporation techniques. During evaporation atoms falling on a silicon oxide substrate at a high temperature tend to diffuse towards nucleation sites. The stability of Au against oxidation, leads to weak substrate-metal interaction which favors Volmer-Weber like island growth mode [90]. The general shape of the islands is complex, but is assumed to be oblate spheroid in many theoretical conductance derivations. One can

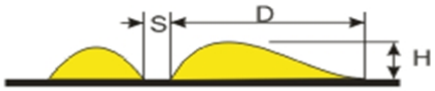

FIGURE 5.2 Islands of a discontinuous gold film. D is the diameter of an island, H is the height, and S is the inter-island gap width.

derive basic equations based on average parameters such as island size and spacing as depicted schematically in 5.2. In practice the morphology depends on deposition technique and substrate.

The islands grow until they coalesce forming semicontinuous films. The inter-island gap S reduces until a critical separation is reached where electrical conduction by means of electrostatically activated tunneling between the islands can occur [91]. The most applicable theory of transport is charging energy limited tunneling (CELT). Other possible transport mechanisms like percolation and fluctuation induced tunneling (FIT) can also be invoked. The choice is guided by island size and morphology. Since the island shape and inter-island spacings are not well defined many energetic and geometrical parameters arise in tunneling transport equations making estimation of conductance of ultrathin gold films rather difficult [92], [93]. In regard to such complexity, an experimental approach is justifiable, in which we have studied conductance as a function of film thickness. For our purposes, we strive to obtain films with large D/S ratio (Fig. 5.2), that is, films just below the transition to continuity (percolation treshold).

We therefore deposited many ultrathin gold films of nominal thickness 1 nm to 10 nm on silicon oxide substrates and measured their electrical conductances, with the aim of identifying the nominal thickness of the gold layer t_{Au} below which electrical conduction ceases. Samples with thickness 1 to 4 nm had small islands with large inter-island spacings as seen, from example, in a SEM image of a 2 nm film in Fig. 5.3(a). Films of thickness 5 to 6 nm, had larger islands with smaller inter-island spacing as shown in Fig. 5.3(b). The ratio of average diameter (D) of the gold island to inter-island gap is in the range 10 - 100 for a 5-6 nm nominal thickness of gold island layer. Au films of thickness 7 nm to 10 nm were more semicontinuous as shown in Fig. 5.3 (c) and (d).

The 7 to 10 nm thick gold films were electrically continuous with two-probe room temperature resistance in the range 10 to 500 Ω which were easily measured with a digital multimeter. The films with thickness below 1 to 4 nm were electrically

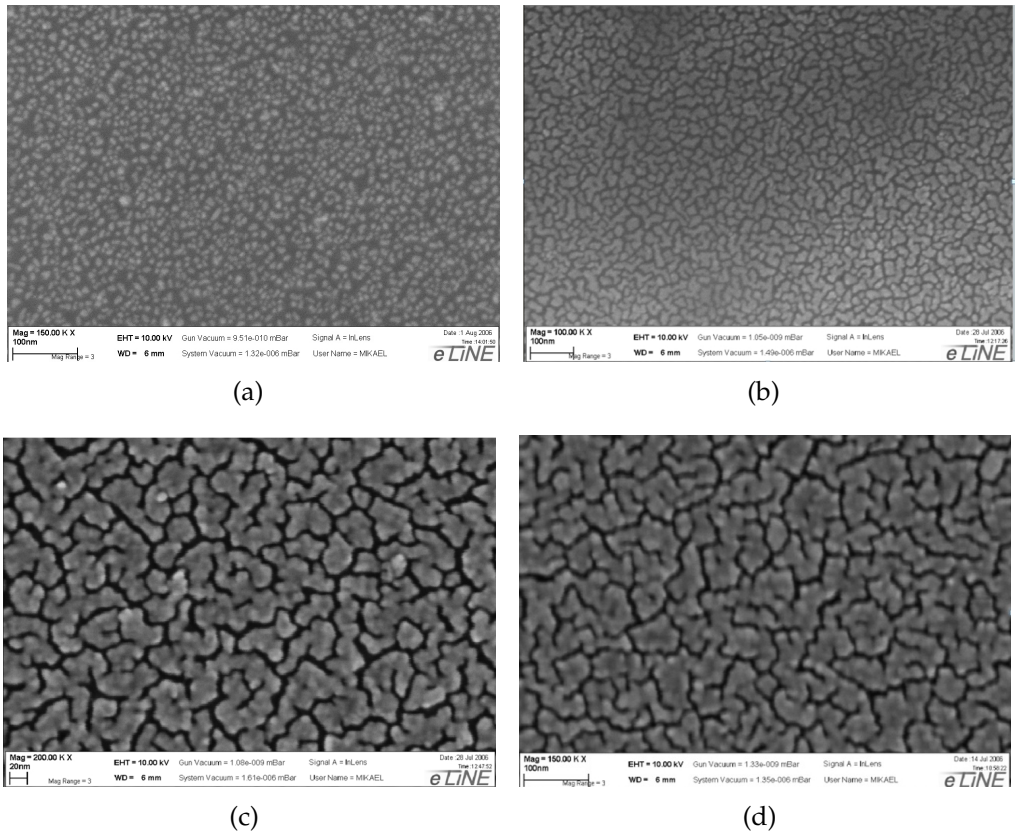

FIGURE 5.3 SEM images of discontinuous gold films of nominal thickness (a) 2 nm, (b) 5 nm, (c) 7 nm and (d) 10 nm. The scale bar on the lower left corner is 100 nm in figures (a) (b) and (d). In (c) the scale bar is 20 nm.

insulating even at very high field. This was expected given the large separation between islands. For 5-6 nm samples, whose inter-island spacing are small enough for one to consider a possibility of tunneling at high field, we measured current as a function of voltage as shown in Fig. 5.4 (a). Within the voltage range of 0 to 1 V the measured currents stay well below 100 pA, therefore these are insulating with resistances exceeding ≈ 10 GΩ within the resolution of the current measurement. However at voltages above 2 V high tunneling currents are observed that approach 1 nA above 5 V as shown in Fig. 5.4 (a). We estimate the zero bias resistance of 6 nm gold films films to be ≈ 100 GΩ. The conductances of the Au films are plotted as a function of nominal thickness in Fig. 5.4 (b).

From these conductance measurements and SEM studies discussed earlier we chose gold films of thickness 6 nm (that is, just below the percolation treshold) and below for polymerization studies as discussed in the next section.

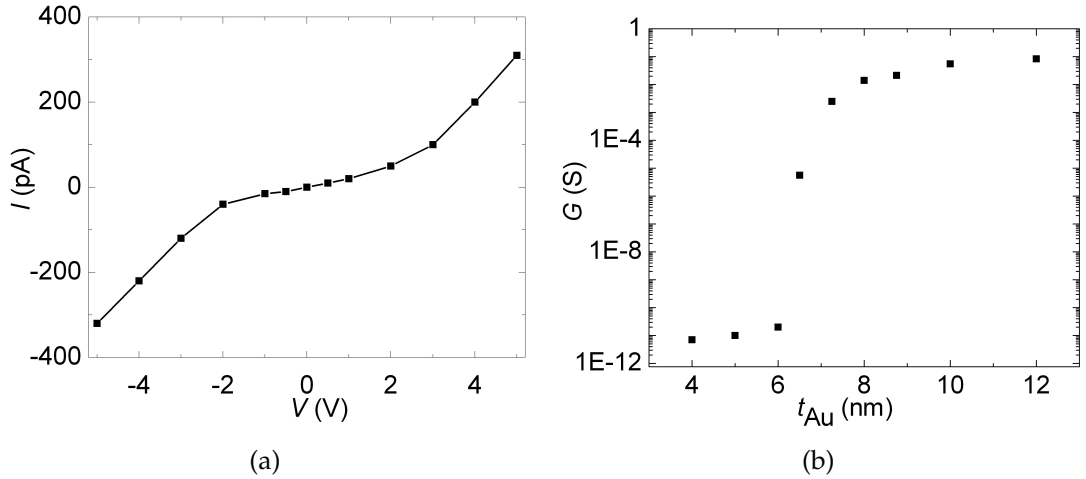

FIGURE 5.4 Room temperature electrical properties of ultrathin gold films. (a) Current-voltage characteristics of a gold film before deposition of polymer. (b) Room temperature Au films conductance as a function of thickness.

5.3 Fabrication of polypyrrole on insulating substrates

Preparation of the PPy-Au devices in this work involved fabrication of microelectrodes and the ultrathin gold films, and electropolymerization on top of these.

5.3.1 Fabrication of microelectrodes and ultrathin gold films

In Fig. 5.5 we show optical and SEM images of the real device based on the concept presented above. Electron beam lithography was used to fabricate microelectrodes on a silicon oxide substrate as described earlier in Chapter 4. In Fig. 5.5, electrodes A and B are anode and cathode, respectively, that drive the electropolymerization. Electrodes C1 and C2 are inserted for measuring purposes and electrodes labeled D are used for optional dedoping of the polymer films. The C1, C2 and D electrodes do not participate in the polymerization process.

Next, a patch of discontinuous gold films (1 to 5 μm wide) was fabricated on/between the microelectrodes using four alignment marks as shown in Fig. 5.5. The alignment marks facilitates the placement of the gold film on the right location. Figures 5.6 and 5.7 show AFM images of the gold film layer before polymerization.

We had two cathode-anode configurations, see Fig.5.8, namely a gapped configuration as in which the top edge of the ultrathin film overlaps the anode while the lower edge of the film is not in contact with the cathode, and a bridging configura-

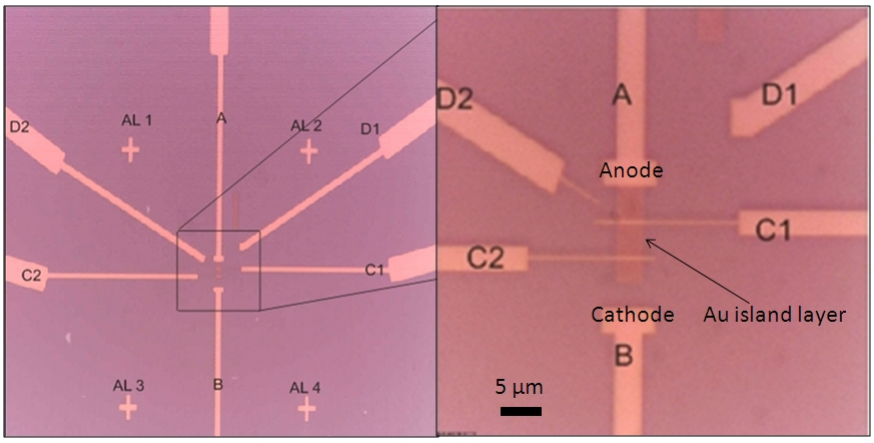

FIGURE 5.5 Electrodes and ultrathin film layout. The Au layer is the vertical strip in the middle of the images. In the lower right image, the black arrow points towards it.

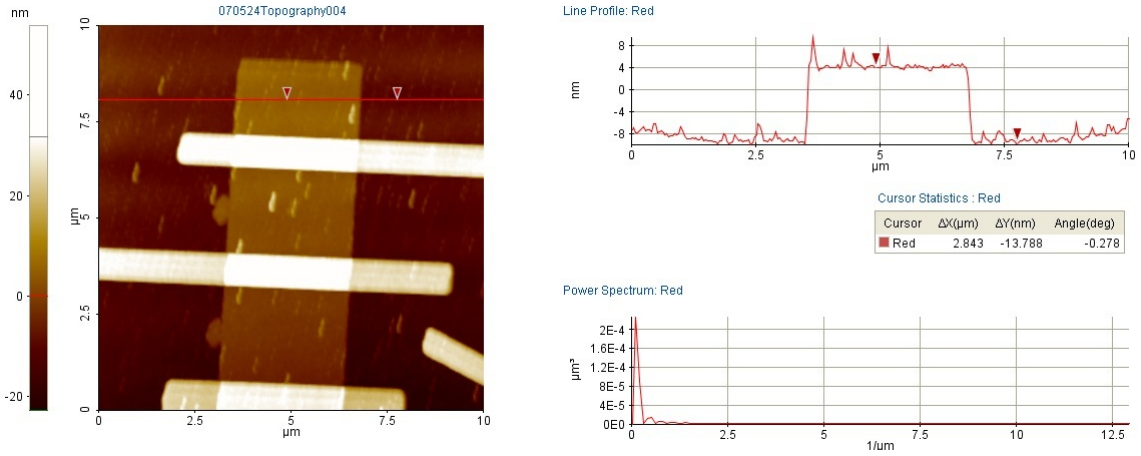

FIGURE 5.6 AFM image of a 6 nm nominal thickness gold film.

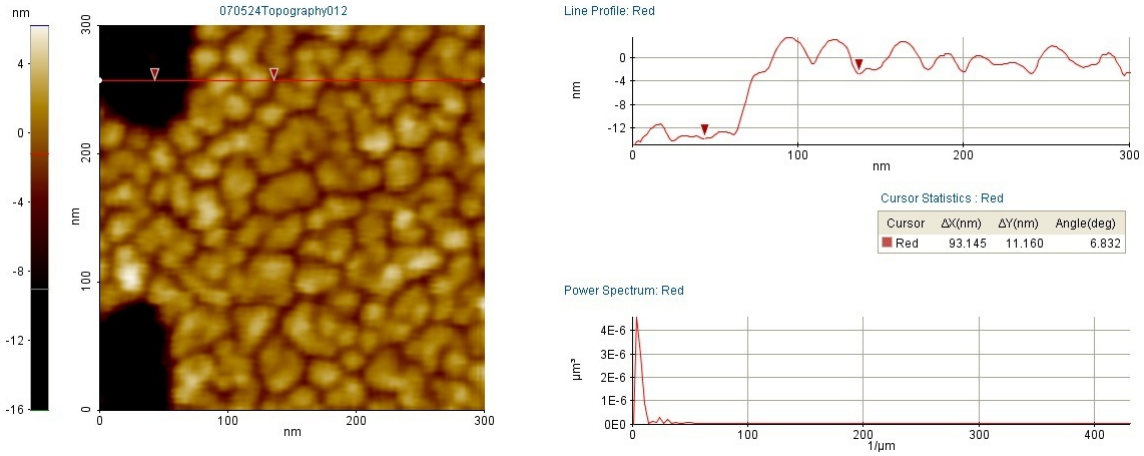

FIGURE 5.7 Close-up AFM images of a 6 nm thin gold film islands. AFM image of Au film height profile a sample with deposition nominal thickness 6 nm. The thickness measured by AFM is 14 nm.

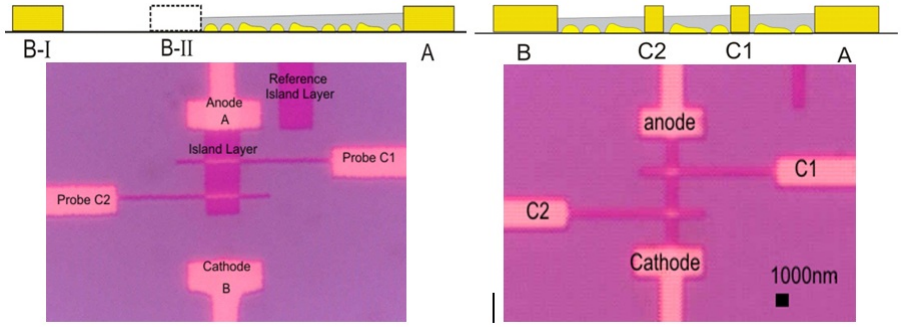

FIGURE 5.8 Schematic showing side section views of the two configurations of the deposited island layers.

tion in which the film is in contact with both electrodes. The bridging configuration ensures that polymerization terminates automatically when the conducting polymer bridges the anode and cathode, thereby reducing the electropolymerization potential to zero.

5.3.2 Electrochemical Synthesis of polypyrrole on substrates

An electrolyte consisting of 0.1 M pyrrole monomer (C_4H_5N), 0.05 M tetrabutylammonium hexafluorophosphate in propylene carbonate was prepared. The hexafluorophosphate is the dopant ion. A 2 mm wide electrolyte droplet was placed on the chip to span the cathode and the anode as shown in Fig.5.1 and a voltage of 2 V to 4 V was applied. Electropolymerization was done under nitrogen flow and at room and low temperature (≈ 230 K) to prevent oxygen induced degradation of polymer observed in polymers synthesized in ambient conditions.

The Atomic force microscope (AFM) (Fig4.4(b)) was used to determine thickness and morphology of the polypyrrole films. In general the films exhibited a more granular surface morphology as shown in 5.10 [94]. The thickness of polypyrrole films ranged from 10 nm to 200 nm. The films were thicker at the anode side and thinner at the cathode side. This is seen as a color gradient in figure 5.9.

AFM images of very thin PPy-Au films in Fig. 5.10 show that the polymer follows the profile of the gold island with narrow polymer links between gold island. However, in thicker films the surface has a more granular morphology like pellets as shown in Fig. 5.10.

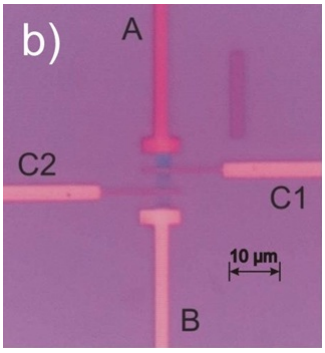

FIGURE 5.9 Optical image of sample after polymerization. The separate strip to the upper right is another gold island layer that remains unpolymerized and thus shows the contrast between pristine and polymer-covered island layers.

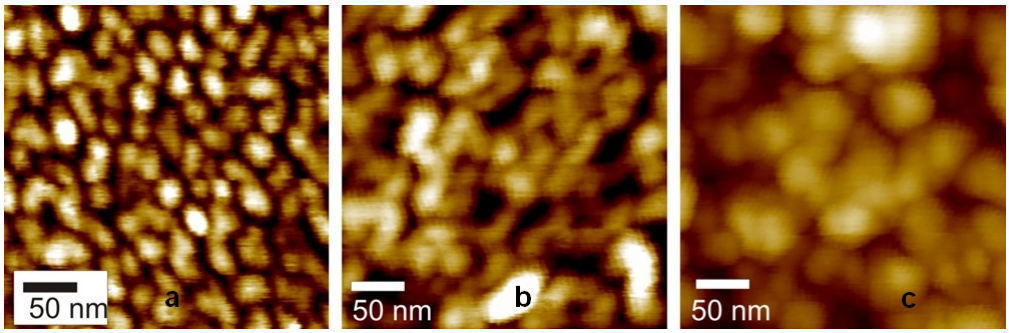

FIGURE 5.10 AFM images of samples before and after polymerization.(a) A gold island layer before deposition of polymer.The nominal thick of this film is 6 nm.(b) Surface of sample of PPy/Au with total thickness (t_{Au} + t_P) $\approx$ 45 nm and room temperature resistance 770 kΩ. (c) Surface of sample B with thickness 120 nm and a room temperature resistance of 1.2 kΩ

5.4 Results on transport measurements in PPy-Au structures

In this section we present the results of electrical conductivity measurements we took on polypyrrole-gold samples which we fabricated in this work. We first present room temperature conductivity measurement results in section 5.4.1 and highlight the dominant conduction path in a composite system. Temperature dependence measurements of conductivity, from which transport mechanisms are deduced are presented in section 5.4.2. Field dependence measurements are provided in section 5.4.3.

5.4.1 Room temperature conductivity of PPy-Au:Role of gold islands

Some of the samples that were fabricated and measured are presented in Table 5.1. The table presents the essential data for each sample. From a total of 10 samples, 4 samples with low room temperature resistances were selected and used in low temperature measurements reported in section 5.4.2.

Sample	Config.	Gold layer thickness, t_{Au} (nm)	Film width, w (µm)	Sample Length, L (µm)	PPy-Au Thickness, t_p+t_{Au} (nm)	Resistance at 300 K (Ω)
				(Sections: $AC_1/C_1C_2/C_2B$)	(Sections: AC_1/C_1C_2)	(Sections: AC_1/C_1C_2)
I-A	I	6	5	3/5/7	25-75/25-40	26 k/2.6 M
I-B	I	6	5	5/5/5	100-120/70-90	1.2 k/2.6 k
I-C	II	5	1.5	3/3/2	14-20/10-15	105 k/370 k
I-D	II	6	1.5	3/3/2	10-25/9-12	740 k/6.4 M
I-E	II	6	1.5	3/3/2	Not Meas.	18 M/-
I-F	II	6	1.5	3/3/2	50-75/35-45	48 k/113 k

TABLE 5.1 List of PPY-Au samples. The table provides sample details such as electrode configuration (discussed in Fig.5.8), width(w) and thickness of Au film (t_{Au}), combined thickness of Au and PPy, room temperature resistance (R) and sections of sample where R was measured.

PPy is one of the more stable polymer in the doped state such that its conductivity is quite stable for long duration in air. Our PPy samples exhibited good resistance stability for many days in ambient conditions as shown in Fig.5.11. Samples

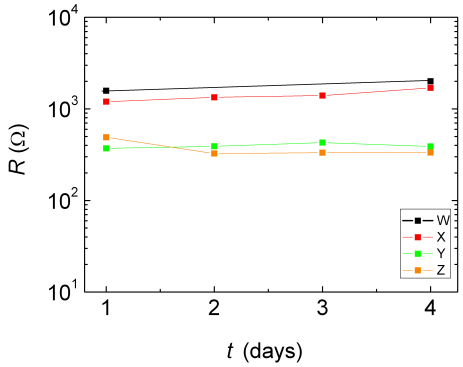

FIGURE 5.11 Resistance stability under ambient conditions.

FIGURE 5.12 Model for conduction in hybrid PPy-Au structure.

with resistance below 100 kΩ exhibited less than 10 percent variation in resistance for several weeks. This good resistance stability ensured that our samples had retained their conductivity during the time frame between polymerization and low temperature conductance measurements, which usually could take place a couple of days after polymerization.

In a hybrid system like our PPy-Au samples the central question is whether the conduction is dominated by gold islands, through the nanoscale polymer filled interisland gaps, or by the doped PPy film itself. To address this question we consider the values of room temperature conductivity and the geometrically simplified conduction model in Fig. 5.12 which assumes a smooth homogeneous polymer film with islands of width D separated by distance S.

We first consider the ideal case where the polymer is only between the gold islands and not above the gold island height (i.e t_P = 0). The conductivity of bulk gold is 5 x 10^5 S cm^{-1}, while that of highly doped PPy varies in the range 1-10^3 S cm^{-1}. From SEM and AFM images the ratio D/S ranges from 10 to 100 for island layers with nominal thickness of 5-6 nm. One can then assume that the combined resistance of the island layer and the polymer is dominated by the polymer, even neglecting interfacial resistance.

In practice there is a polymer layer above the island layer (t_P = 0). Within the ohmic regime, the ratio of resistance of PPy above the island to the resistance em-

bedded in the island layer can be given by the following relation:

$$\frac{R_P}{R_i} \approx \frac{D}{S}\frac{t_{Au}}{t_P}, D >> S. \tag{5.1}$$

The resistance ratio $\frac{R_P}{R_i}$, that may either be > 1 or < 1, can determine whether the dominant path of charge transport is the polymer above the island layer or via the polymer filled island layer. In this work we focussed on samples with t_{Au} = 5 or 6 nm. Since t_P varies from 100 nm to 10 nm, we get $\frac{t_{Au}}{t_P}$ ratios in the range 0.1 to 1 and hence $\frac{R_P}{R_i}$ > 1 implying that conduction of the composite system will be dominated by the intrinsic conductivity of the polymer between islands. The effective resistance of the hybrid system, should therefore remain $\approx R_i$ as t_P approaches t_{Au}. However, we found as shown in Table. 5.1 that as the thickness of polymer decreases, the resistance increases faster than predicted by the ohmic model. This behaviour can be explained in two ways. Either, the intrinsic conductivity of the polymer improves with increasing thickness or there may be resistive barriers between the gold islands and the polymer. The latter case is more likely if we consider the rough morphology of the films.

The room temperature conductivity of our thicker polymer samples is dominated by the intrinsic conductivity of the polymer above the island layer. We may then calculate the values of conductivities of our thicker samples as $\sigma = L/R_P w t_P$. The values are shown in Table 5.1. We find that the PPy in the samples we synthesized in this work exhibit zero-bias conductivity ranging from 10 to 100 S/cm at room temperature (300 K). Such values indicate that the PPy is of a relatively good quality.

5.4.2 Temperature dependence of conductance

Samples (II-A, II-B, II-C, II-D), listed in Table 5.2, exhibited negative temperature coefficients of resistance. At low temperature 4 K the samples are more insulating with resistances R > 10 GΩ. These samples have a resistivity ratio (R_{4K}/R_{300K}) » 10 and therefore fall within the insulating regime of the disorder induced metal-insulator transition (MIT) [4]. It is reasonable then to expect hopping transport mechanisms in these samples. The plot of resistance vs. $T^{-1/4}$ in figure 5.13 shows that within temperature range 20 K to 300 K the zero-bias resistances of samples IIA to IID obey a 3D variable range hopping (Mott VRH) transport model [95]. The resistance of the samples can be written as in equation

$$R(T) = R_0 \exp\left[\left(\frac{T_0}{T}\right)^{1/4}\right]. \tag{5.2}$$

Sample	Measured Section	L/w (µm)	U (V)	$t_p + t_{Au}$ (nm)	R (kΩ)	σ_{RT} (S/cm)
II-A	C_1C_2	3/5	4	70	1.2	71
II-B	C_1C_2	5/5	4	200	1.5	33
II-C	C_1C_2	3/5	4	30	11.5	17
II-D	AC_1	3/1	2	50	40	15

TABLE 5.2 Parameters for selected samples on which low temperature measurements were done. Sample configuration, width, combined thickness of Au and PPy, room temperature resistance and conductivity is given for each sample.

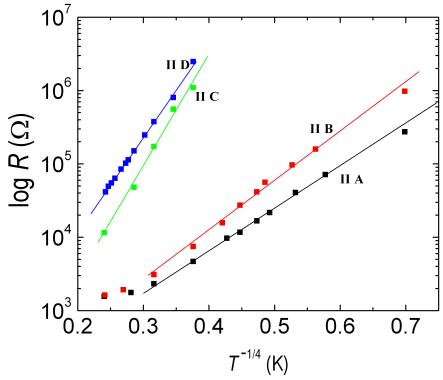

FIGURE 5.13 Temperature dependence of zero-bias resistance of PPy-Au samples.

where R_0 is characteristic of the sample T_0 determines the thermal activation energy for hopping among localized states. Slopes of log R vs $T^{-1/4}$ are smaller in thicker and wide samples (IIA and IIB) and greater in thinner and small width samples (IIC and IID).

The fact that both these mesoscopic $PPy - PF_6$ Au samples (thickness 30 - 200 nm) and bulky $PPy - PF_6$ samples (thickness 5 μm to 15 μm) [4] can all fit to 3D VRH model can be explained in that all samples in insulating regime have localized states domains, between which hopping occurs, which are nanoscale and thus hopping is dominant in both types of samples regardless of size of the overall sample. The conductivity of the bulky samples were also in the range 10 to 100 S/cm [4].

5.4.3 Field dependence of conductance

A current-voltage (I-V) spectroscopy technique is used to probe the transport mechanisms in the PPy-Au samples within a temperature range 300 K to 4.2 K. This method is chosen because it is well known to be a powerful method that provides

good insight into tunneling like transport behavior and rectification in CPs at low temperature. This technique is a good supplement to temperature dependence, magnetoresistance and thermoelectric power studies [20], [96], [97]. I-V spectroscopy is also widely applied in studies of tunneling junctions in general [98]. This I-V approach is justifiable to our mesoscopic samples as they constitute Au-PPy-Au structures in series especially at low temperature.

In samples IIA, IIB, IIC and IID, the I-V characteristics are linear in temperature near 300 K and nonlinear at low temperature. Regardless of temperature all the samples exhibit symmetrical I-V curves implying that the PPy-electrode interface is smooth and ohmic and not rectifying as seen in other works reported in literature [99], [20]. As the temperature is lowered there is a transition to nonlinearity at some low temperature that varies from sample to sample as seen in Fig. 5.14. In general, it is seen that the higher the conductivity the lower the transition temperature.

All samples show a zero bias anomaly (ZBA), or the reducing or vanishing conductivity at V = 0, at low temperature $(T < 20K)$ as shown in plot of differential conductance versus bias voltage in Fig 5.14. The zero bias anomaly is more pronounced for samples with lowest conductivity. The reason for the ZBA is the Coulomb gap, the dip in density of states in disordered materials, as a consequence of enhanced electron-electron interactions.
ly (ZBA), or the reducing or vanishing conductivity at V = 0, at low temperature $(T < 20K)$ as shown in plot of differential conductance versus bias voltage in Fig 5.14. The zero bias anomaly is more pronounced for samples with lowest conductivity. The reason for the ZBA is the Coulomb gap, the dip in density of states in disordered materials, as a consequence of enhanced electron-electron interactions.

Large current fluctuations are observed in low temperature I-V curves of the narrowest sample IID of width $\approx 1\mu m$ around a bias voltage of $\pm$200 mV (5.16). This is not seen in IIB, IIC and IID which are 5 μm in width. Repeated measurements on this sample indicate that the fluctuations are intrinsic to the sample and not measurement artifacts. Such type of fluctuation have been reported in nanoscale CP wires and have been attributed to switching between the reduced and oxidised states of the doping of the polymer [21]. Strong noise arising from two-level fluctuators are a general feature of carbon based electronic devices [100], [101]. It is seen that the fluctuations in our sample IID are more prominent at low carrier density. The exact cause of these fluctuations is not very clear.

The field scaling of our samples at low temperature is examined by plotting logarithm of current vs $V^{1/4}$. From Fig 5.17 it is seen that the log of I follows $V^{1/4}$. The data fits well to this equation especially at low temperature and high field. There

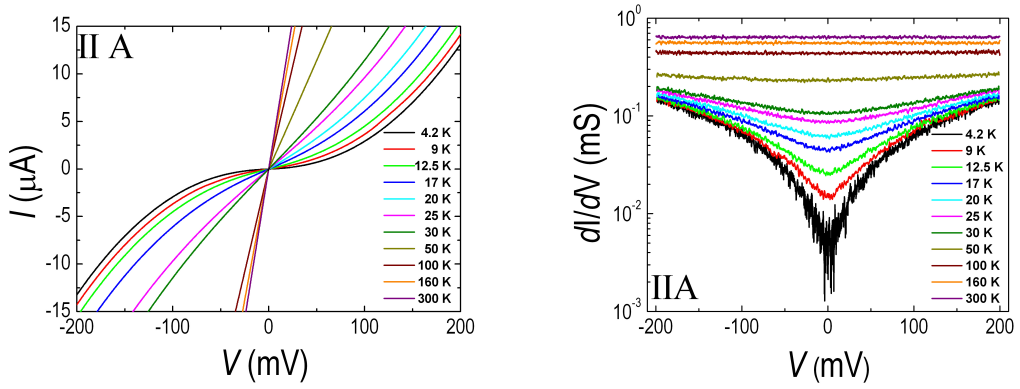

(a) (b)

FIGURE 5.14 (a) Current-voltage characteristics of PPy-Au sample IIA at various temperatures. (b) Corresponding differential conductance curves of sample IIA.

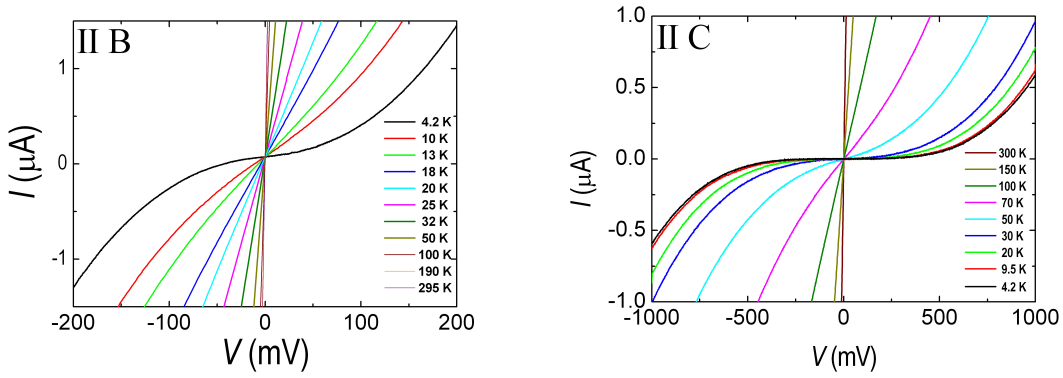

(a) (b)

FIGURE 5.15 Current-voltage characteristics of (a) PPy-Au sample IIB at various temperatures and (a) sample IIC.

is deviation from the $V^{1/4}$ at high temperature and low field. In the higher conducting sample IIA, the data fits well to the $V^{1/4}$ power law only at $T < 10K$. This is because IIA is very close to the metal-insulator transition and field dependent hopping conduction is only dominant at very low temperature. These plots of log I vs. $V^{1/4}$ may indicate that electric-field induced hopping is dominant transport at high fields and low temperature [20]. It is also seen that the I-V curves at low temperature (< 10 K) tend to converge at high field and low temperature in samples IIA and IIC. This is a signature of self-heating.

It is seen in fig. 5.17 that slopes of the portion of the curves that fit $V^{1/4}$ law tend

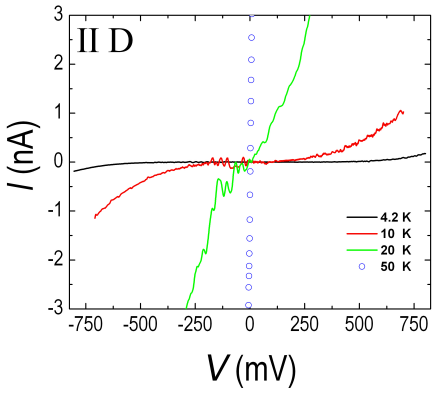

FIGURE 5.16 I-V curves of sample IID. Strong current fluctuations are observed.

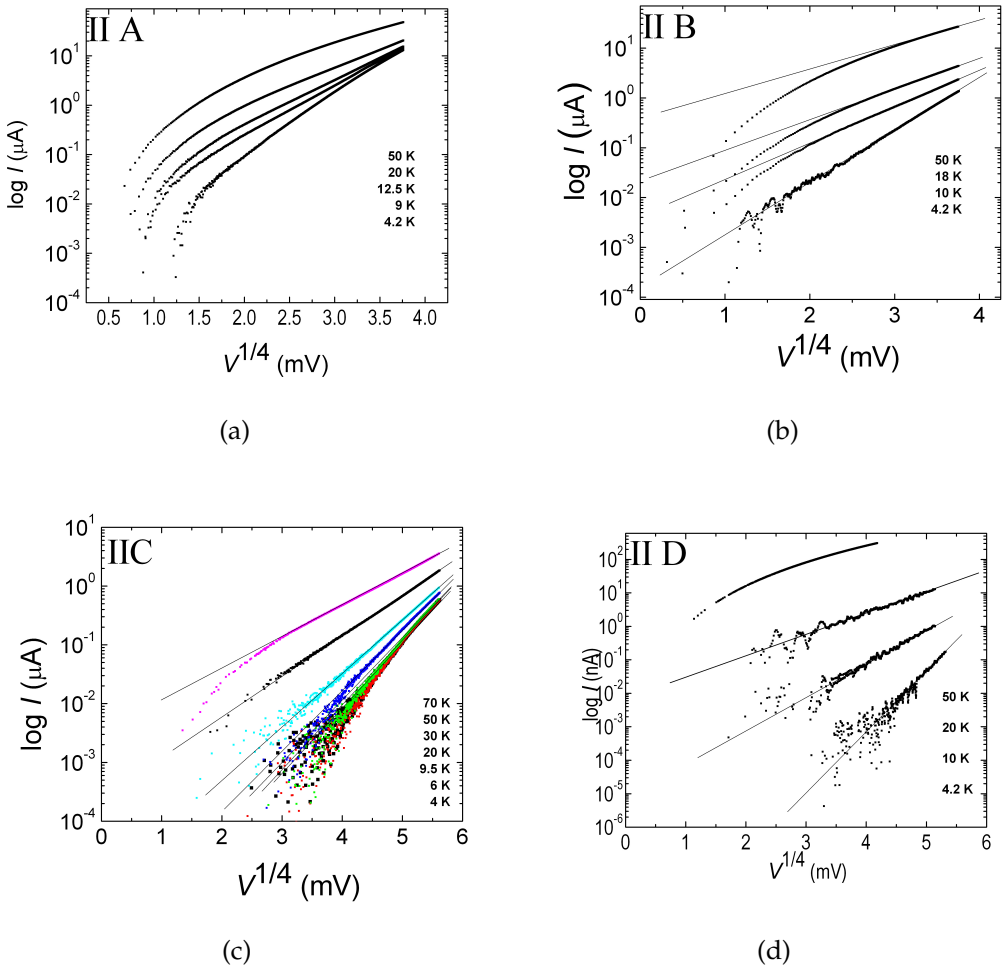

FIGURE 5.17 Logarithmic plot of I vs. $V^{1/4}$ at various temperatures for (a) PPy-Au sample IIA, (b) sample IIB, (c) sample IIC and (d) sample IID.

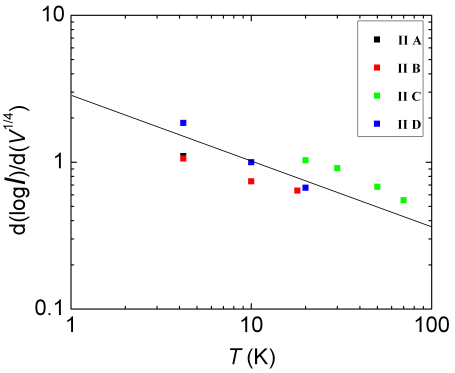

FIGURE 5.18 Field and temperature dependence.

to increase with decreasing temperature. The slopes vary from 0.6 to 2. Plotting these slopes of Fig. 5.17 as a function of T in Fig 5.18we see that the field dependence of all the samples can be described by a phenomenological model 5.3

$$I\left(V\right) \propto \exp\left(\frac{KV^{1/4}}{T^{1/2}}\right). \tag{5.3}$$

where K is a fitting constant.

This model is very different from conventional V^2 and $V^{-1/4}$ field dependencies predicted by theory [102]. Gence *et al.* [20] reported a $V^{-1/4}$ behaviour in Au-PPy structure with similar Au-PPy interface but with longer PPy sections. We are unaware of a transport theory that would exactly match our measurement results, which is not surprising considering the composite character of our system. This peculiar field dependence shows that hybrid systems like metal-CP nanostructure are interesting for exploring novel charge transport mechanisms.

5.5 Future outlook

In this thesis a novel technique for fabricating hybrid conducting polymer-gold films of thickness 10 to 200 nm and width 1 μm to 5 μm by electrochemical synthesis on ultrathin gold films has been successfully demonstrated. The next step will be to reduce the width of the polymer-gold films to the nanoscale regime (20 - 200 nm) by using narrower underlying gold island layers or by etching some areas of the polypyrrole-gold films and fabricating a backgated field effect transistors based on this hybrid material. Further experiments are need to understand the effect of gold islands on transport in the hybrid material and also on how these islands would affect the performance of FET transistors based on these systems.

In light of a recent scaling analysis of field dependent conductance in conducting polymers where the field scales for non-linearity is set by the intrinsic disorder of the samples and not the temperature, it might be worthwhile to look at the field dependent transport in this nanostructures to relate the physical length scales such as localization length or hopping length which can be related to the origin of the field scale [96].

Chapter 6

Transport measurements on intermediate sized MWNTs

6.1 The goal: Experiments on electron transport in intermediate sized MWNTs

This thesis is focused on size dependence studies in a rather unexplored intermediate diameter range 3 nm to 10 nm and length 200 nm to 4 μm to understand the scaling of transport properties with diameter in particular but also length. In addition, we have a few samples with diameters 1.3 - 2 nm and 11-13 nm. From diameter dependences of transport properties it is possible to see signatures of size constriction and interwall interactions and from length dependences we can learn of the transport regimes of our samples. If one imagines unwrapping our nanotubes of diameter 3 nm to 10 nm tubes one would get graphene nanoribbons of corresponding width ranging from 9 nm to 32 nm. This is significant because it is relatively difficult to fabricate good nanoribbon devices with such small width and indeed there has been not much work on nanoribbons in that width range. Related work on influence of size have been on transport properties of graphene nanoribbons of width $20 < W < 120$ nm [87], [72]. In the latter work the size of nanoribbons correspond to unwrapped nanotube of diameters in range 6.5 nm to 38 nm. This thesis work therefore fills the size gap that has not been studied extensively. Our approach has been to fabricate nearly 100 devices with fixed palladium electrodes (metal-on-tube architecture) while varying length from sample to sample and in some cases making 2 to 3 devices on one single tube. The advantage of such an approach is the ability to make near-ohmic contact.

6.2 Fabrication of MWNT samples

The electron transport studies reported in this work are focussed on MWNTs of a special diameter range, 3 nm to 10 nm, which were previously rare owing to synthesis problems. In light of this, we first discuss how these nanotubes were synthesized and characterized in section 6.2.1 and then discuss how we fabricated the devices in section 6.2.2.

6.2.1 Nanotube material with a special diameter range

MWNTs used in our transport experiments were obtained from the group of S. Iijima [66]. The nanotubes were synthesized via a catalyst-free arc-discharge technique achieved by direct vaporization of a graphite rod using radio frequency plasma. To verify that these were MWNTs and not SWNTs a sample of the purchased MWNTs powder was imaged with high resolution transmission electron microscopy (HRTEM). The results of these TEM measurements showed that the powder was composed of predominantly MWNTs as shown in Fig. 6.1. The results of this atomic scale characterization show that the samples were relatively clean and indeed predominantly MWNTs in agreement with supplier specifications.

The nanotube powder was specified to have MWNTs with outer diameters about 5 nm and smallest inner-most wall diameter of 0.4 nm via TEM studies. Our AFM studies of MWNTs from this material found that most tubes were in the range 3 nm to 6 nm with occasional nanotubes with diameters in the range 6-8 nm or below 3 nm as shown in Fig. 6.5(a). Rarely did we find tubes with more than 10 nm diameter. Taking the inner-most wall diameter into account we can deduce that our nanotube devices in the range 3 to 10 nm have the number of walls (shells) ranging from 5 to 15.

6.2.2 Fabrication of backgated MWNT devices

A meaningful study of size dependence of properties of many individual devices on different silicon chips requires that all the devices are fabricated in the same way and that the only fabrication variables are the nanotube diameter and channel length. To meet this requirement, all nanotubes reported in this work were selected from the same batch of MWNTs and processed with the same solvents and fabrication techniques. The architecture of all MWNT devices was that of a backgated CNT-FET, described in section 3.3.2 (Fig. 3.7) and also in Fig. 4.1(b), in which the bulk silicon

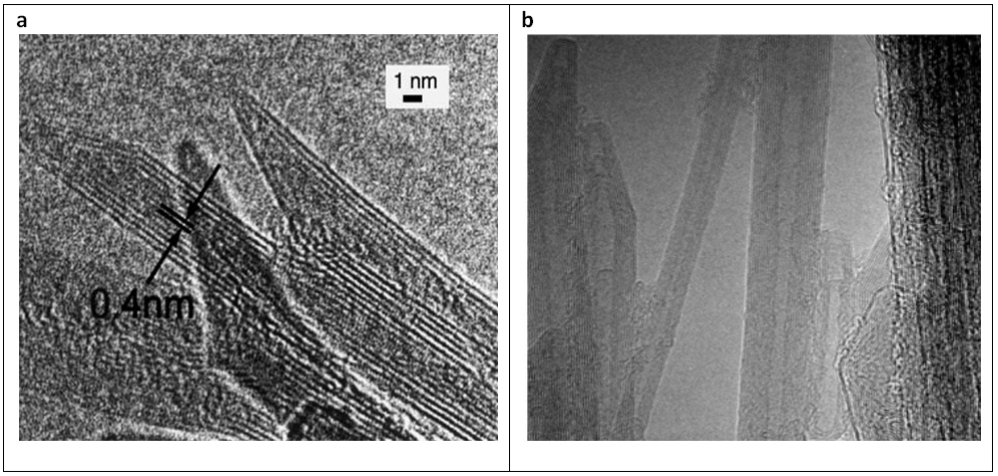

FIGURE 6.1 (a)HRTEM image of MWNTs taken a batch of nanotubes synthesized by Iijima group. The image is adapted from [66]. Note that our nanotube powder material was taken from this batch. (b) HRTEM of nanotubes from same batch. Courtesy:Hua Jiang, Aalto University.

layer is used as a backgate and a 300 nm thick silicon oxide layer is the dielectric material that separates the backgate from the nanotube.

A powder of catalyst-free arc-discharge grown multiwalled nanotubes was dispersed in 1,2-dichloroethane and the resultant suspension was sonicated for 30 minutes. It is well known that random atomic defects may be present in solution processed nanotubes [5]. In view of this, we carried out scanning tunneling microscopy (STM) studies of our nanotubes and found them to be atomically clean. The use of catalyst-free nanotubes precludes the possibility of p-type doping which is known to arise from reaction products of halogen solvents and some catalytic nanoparticles such as iron [103].

A droplet of the nanotube suspension was spinned on the substrate. The nanotubes are randomly oriented on the chip. The surface of the chip was scanned with an atomic force microscope and the positions of individual nanotubes was determined using micron sized markers. Clean and straight nanotubes were selected and their diameters were measured using an atomic force microscope (AFM) with $\pm$ 0.1 nm specified accuracy. The accuracy of our diameter measurements is $\pm$0.3 nm on account of substrate roughness. During diameter measurements a very small force was applied to the sample to avoid pressing the tubes which would result in an underestimation of diameter.

Nanotubes with varying diameters were selected and two or several palladium electrodes of 100 nm - 300 nm width were fabricated onto the nanotubes using PMMA based lift-off electron beam lithography. A recent study has shown very

weak dependence of contact resistance on contact length (electrode size) [104]. In our samples the inter-electrode spacing (or channel length), L varied from 0.3 - 4 μm. Clean and straight nanotubes were selected and the tubes were not subjected to high energy plasma to avoid creating more defects. Thus the nanotubes studied can be considered relatively clean and any atomic scale disorder may be associated with inevitable synthesis impurities and defects. Fig.6.2 shows AFM images of many kinds of nanotubes that we found. Most of the nanotubes studied in this work were clean, straight and had uniform diameter. On some nanotubes several devices of different lengths were made as shown in Fig. 6.3. The sample yield varied from chip to chip, and was generally less than 60 percent due to damages of microelectrodes during fabrication, leakage via substrate and electrostatic discharge (ESD) damage.

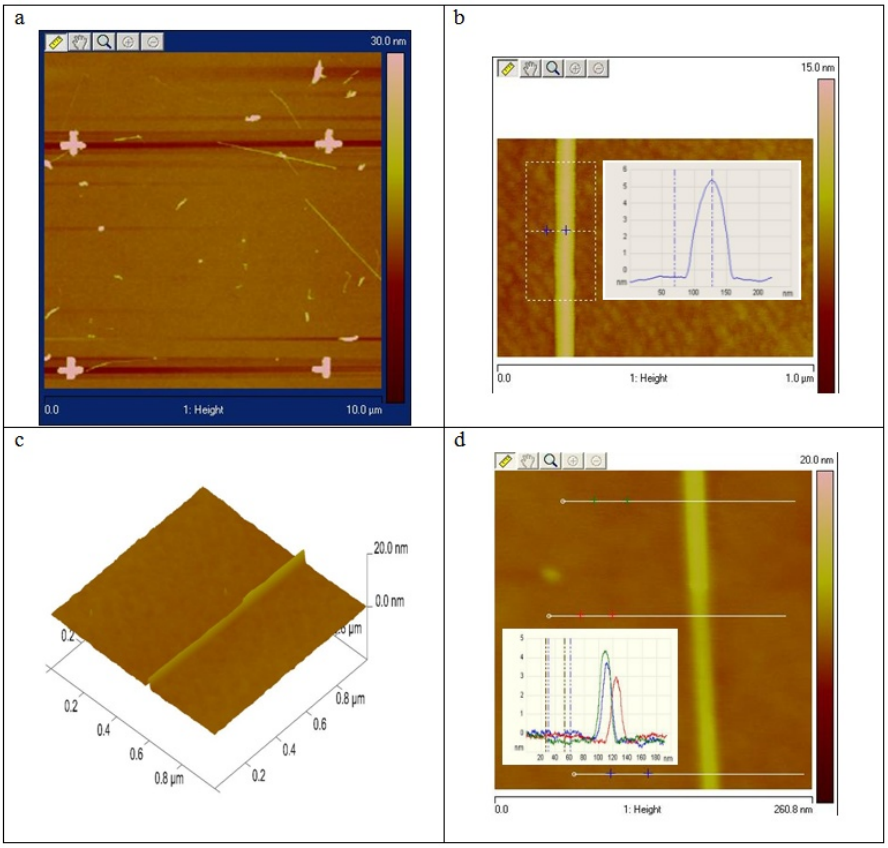

FIGURE 6.2 AFM images of nanotubes on SiO_2 substrate. (a) Nanotubes and marker structures for mapping. (b) Clean nanotube with uniform diameter. (d) Telescope-shaped nanotube with non-uniform diameter.

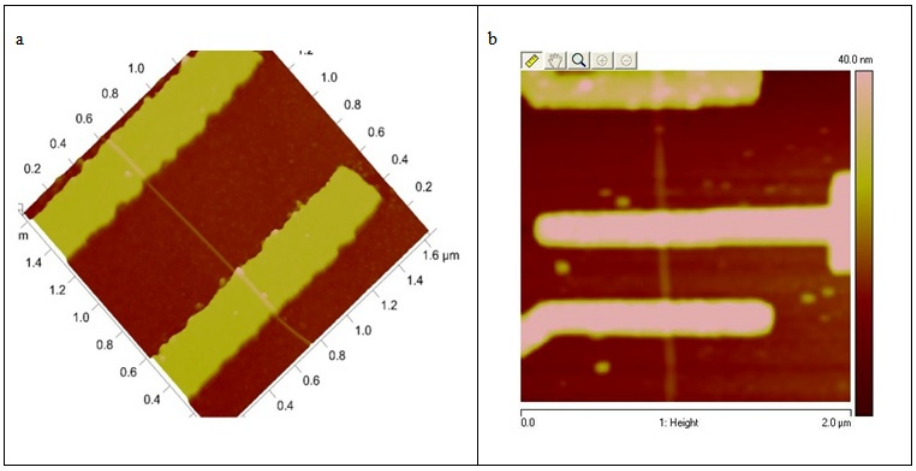

FIGURE 6.3 AFM images of typical MWNT devices showing drain and source electrodes. (a) Single device on a tube. (b) Two devices on one tube. In our sample notation we refer to shorter section as Sample Xa and the longer section as Sample Xb (This particular sample consist of B5a and B5b with data in Table.6.16 in section 6.4.5). Such devices were useful in testing length dependences without structural considerations that may vary from tube to tube.

6.3 General transport features in MWNTs

Electron transport in MWNT devices measured in this work is presented in terms of diameter and length dependences of several gate voltage dependent conduction properties measured at various temperatures and drain-source voltages. The measured CNTs are divisible into "semiconducting" or "gapped" nanotubes, which have a clear transport gap in the I vs. V_G data (and so can be called CNT-FETs), or "gate curves", as illustrated in Fig.6.4 (a), (b) and (c), and on the other hand, into "metallic" nanotubes, shown in Fig.6.4 (d), that do not have strong gate dependent variation on conductance, even at low temperatures. In the semiconducting samples, the transport gaps (offstate regions) sometimes become more pronounced only as temperature is lowered, whereas metallic/quasimetallic samples are those which exhibit finite resistances at the so called charge neutrality point ('offstate') at low temperatures. The gate dependent conductance characteristics that we find in our devices are similar to those generally reported in the literature, with stronger p-type conductance levels than the n-type.

Of the 121 nanotube devices measured in this work, 20 devices exhibited very high contact resistances and were excluded from further studies. 101 nanotubes with good contact resistances were selected for temperature dependent gate response measurements (300 K to 4 K). Of these, 76 were semiconducting (gapped

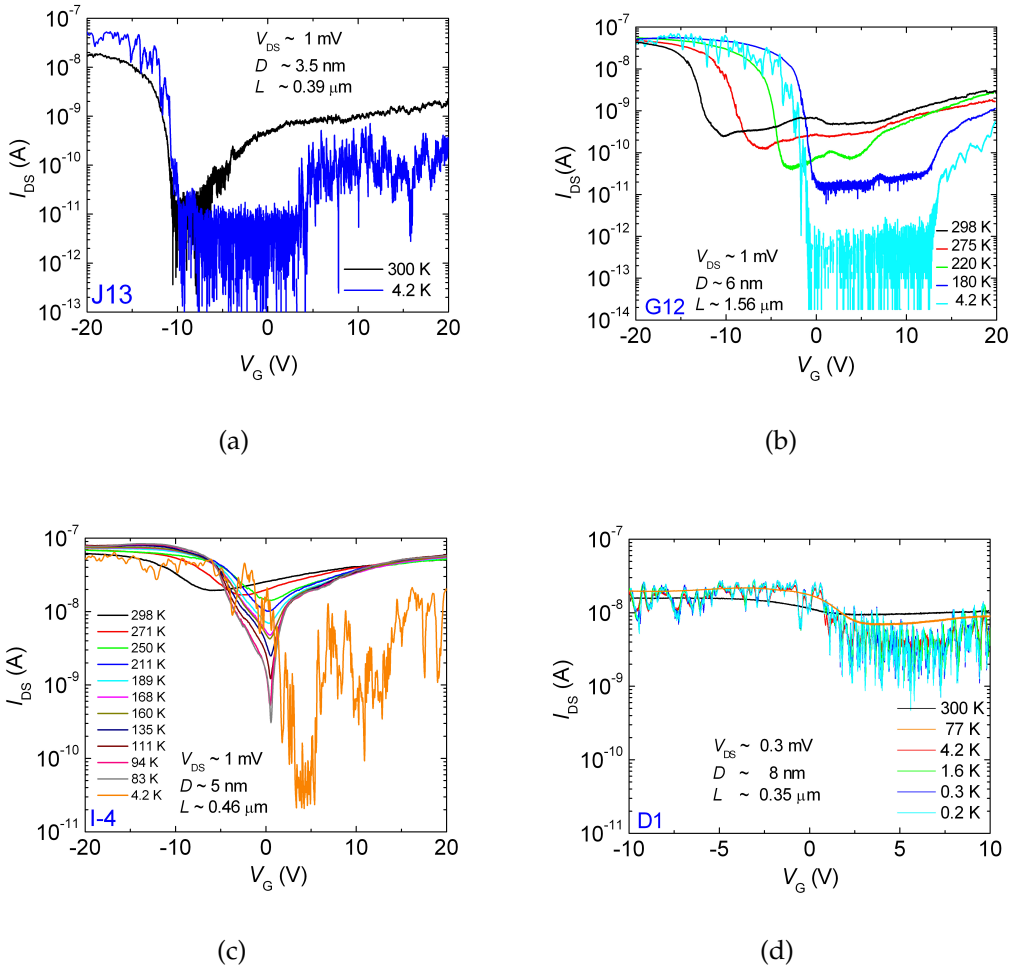

FIGURE 6.4 Typical temperature dependent gate curves. Their form varies from sample to sample. The letter and number at lower left corners are names of samples. (a) Gate curves of a hard gapped nanotube sample (J13) with a small diameter and short channel. (b) Gate curves of an intermediate gapped nanotube (G12) with a large diameter and long channel. (c) Gate curve of small band gap nanotube (d) Gate curve of a metallic nanotube that exhibits finite resistance at very low temperature.

samples) and 25 were metallic or quasimetallic and their diameter distribution is as shown in Fig. 6.3. The distribution of both the diameters and lengths of the measured devices is shown in fig. 6.5(b) (for $D < 10$ nm). The discussion in this thesis is mainly focused on the gapped MWNT devices. However, some data on metallic/quasimetallic MWNTs is included and is presented separately in section 6.5.

Fig.6.4 shows a selection of gate curves for different MWNT devices, taken at different temperatures. It is seen that the gate voltage dependent features vary from sample to sample. As will be demonstrated, this variation is strongly related to the

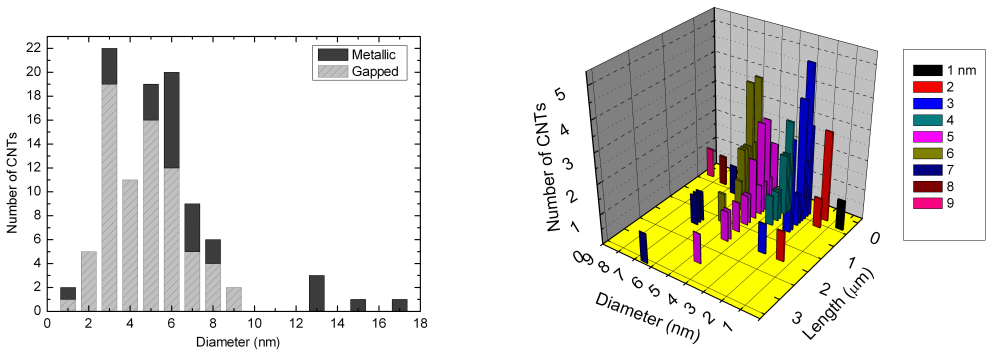

(a) (b)

FIGURE 6.5 (a) Diameter distribution of gapped and metallic nanotubes. (b) A 3D plot showing length and diameter distribution of our nanotube devices.

size dependence (diameter (D) and length (L)) in MWNTs as discussed in section 3.3.6. Moreover, one common feature in all the gate curves is that as temperature is lowered, they exhibit more pronounced oscillations in both metallic and semiconducting nanotubes. These oscillations are due to a combination of quantum transport phenomena and the band structure of the CNTs, as will be discussed further in sections 6.4.5 and 6.5.

Length dependences of transport in MWNT devices are also examined in devices with two or more sections of different length on the same tube as shown in Fig. 6.3. A close inspection of Fig. 6.6 (a) and (b), which show gate curves of sections of different length (0.3 and 0.6 μm) of the same 5 nm tube, reveal that the structure of the gap region is similar. For another set of device (G19a and G19b) with $L \approx 0.4$ μm and 1.1 μm, the width of the gap region (ΔV_G) is greater in the longer section as shown in Fig. 6.6 (c) and (d). The shorter section exhibits one major offstate peak whereas the longer section has two major peaks. For this nanotube the onstate conductance levels for two sections are nearly equal.

Another feature in our measurements is the hysteresis in the gate curves as shown in Fig. 6.3. The position of the transport gap in the gate curve depends on the direction in which the gate voltage is sweeped. This feature complicates studies of temperature dependence of the offstate conductance, as the exact location of the charge neutrality point is not certain, and creates uncertainty in measurements of transport gap widths ΔV_G at high temperature. This phenomena is known to be caused by mobile ions in the dielectric or at the interfaces [105]. Our systematic

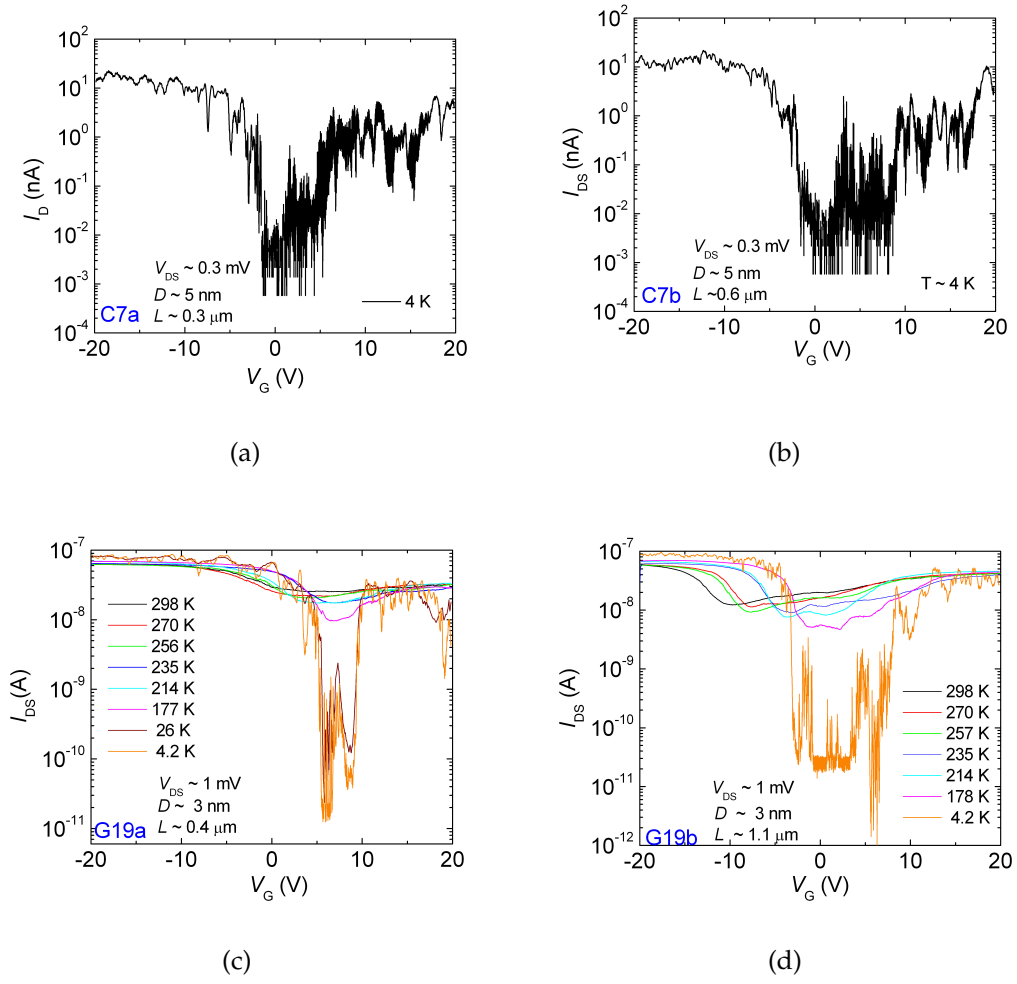

FIGURE 6.6 Gate dependent transport of samples with two sections on one tube. Gate curves (a) and (b) are for two sections of sample C7 of $D \approx 5$ nm nanotube and lengths 0.3 μm and 0.6 μm respectively. Gate curves (c) and (d) are for two sections of sample G19 of $D \approx 3$ nm nanotube and lengths 0.4 μm and 1.1 μm respectively.

studies have shown, as expected, that the hysteresis is highly temperature dependent, with hysteresis shifts up to 30 V (in gate voltage) at room temperature, but is strongly suppressed at low temperatures. It is also seen that the offstate locations are affected by the gate voltage range at room temperature. Although a nuisance for us, the hysteresis behaviour is a useful property for memory applications [106].

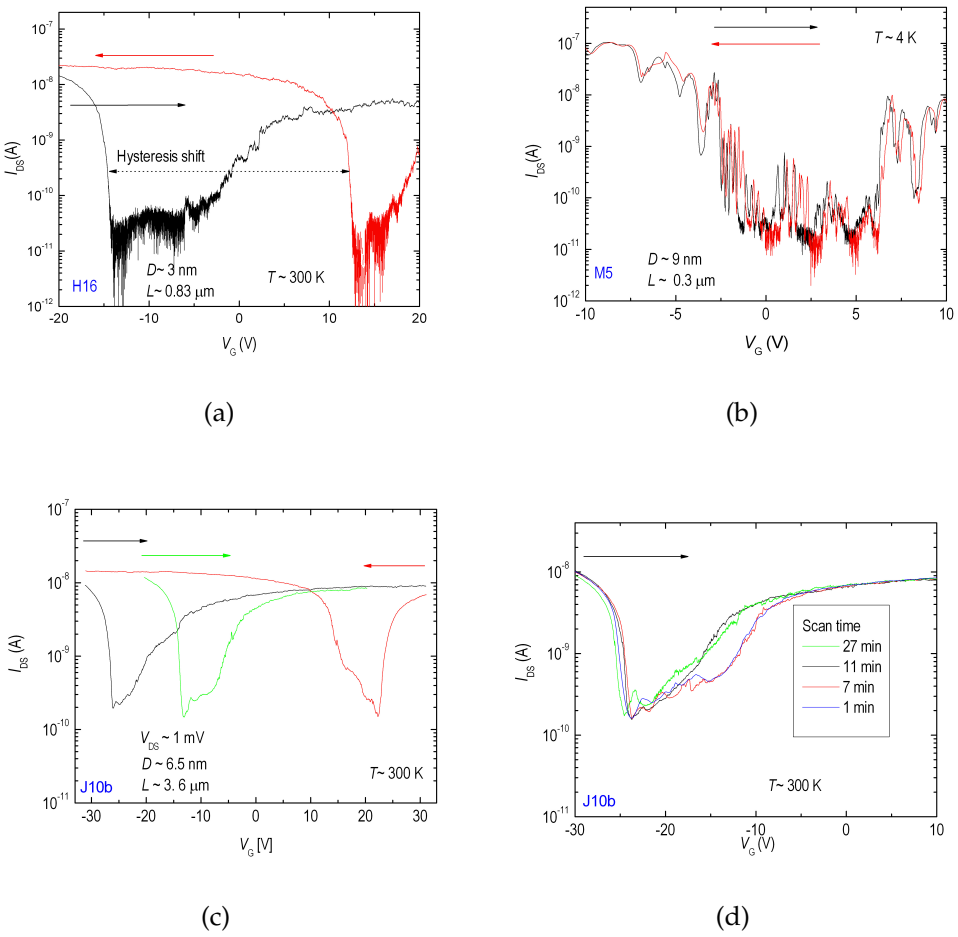

FIGURE 6.7 Hysteresis in gate curves (a) at room temperature, (b) at 4 K. (c) The locations of offstate depend on gate voltage range. (d) The effect of gate scanning speed was also investigated. The arrows on each figure show the directions of gate voltage scanning.

6.4 Measurements on gapped MWNTs

The MWNTs with a transport gap are the main focus in this part of the thesis. They constitute a clear majority of the investigated samples (Fig.6.3). The gate curves have several features that are analyzed in this thesis, some of which were illustrated in figure 3.7 in section 3.3.2. Significant quantities are the zero-bias (low field) on-state minimum resistance (R_{ON}) and the maximum offstate zero-bias resistance (R_{OFF}). R_{ON} is nearly always found in the p-type part of the gate curve. R_{OFF} again usually becomes immeasurably large at cryogenic temperatures so mostly it is available at the higher temperatures. A main issue is the characterization or quantification of the transport gap in the gapped CNT devices. As will be discussed below, such quan-

tities are the room temperature resistance ratio (R_{OFF}/R_{ON}), the bias voltage gap within the transport gap (defined in section6.4.4), and temperature dependence of the transport gap, quantified as the temperature dependence of R_{OFF}.

Our aim was to investigate how the basic transport properties of MWNTs relate to their diameter (D) and length (L) (i.e., the inter-electrode spacing). The following issues are considered for this purpose:

- Size and temperature dependence of the minimum onstate resistance (R_{ON}).
- Size dependence of the resistance ratio(R_{OFF}/R_{ON}).
- Size and temperature dependence of maximum offstate resistance(R_{OFF}).
- Size dependence of the bias voltage gap(ΔU_B).

6.4.1 Size and temperature dependence of the minimum on-state resistance

The gate curves of many samples studied in this work exhibit a strong p-type onstate, an offstate and a relatively weaker n-type onstate. This indicates that hole transport is more dominant in these nanotube devices. R_{ON} at a certain temperature is determined as the minimum zero-bias resistance along the gate curve. As was already stated above, nearly always the minimum on-state resistance R_{ON} is from the p-type part. This p-type dominance behavior is typical for palladium contacted clean nanotubes on silicon oxide substrates. Palladium (Pd) contacted nanotubes tend to have a Fermi level that is aligned closer to a valence band edge. At room temperature transport in onstate is mainly due to hole injection across a weak Schottky barrier. Some samples are more ambipolar while others exhibit no n-type on-state in the entire gate voltage range (-30 V to 30 V).

Figure 6.8 shows R_{ON} at 300 K and 4.2 K as a function of length (L), for a number of samples for which both these values are available. The data is presented such that the dots (whose color is indicative of diameter (D)) are at the 300 K value while the arrow that begins from this dot ends at the 4.2 K value. The onstate conductance at 4 K is oscillatory with local peak resistances lower than the baseline onstate resistance and local valley resistance higher than baseline values. The resistance values

given in this work are the baseline values.

The room temperature R_{ON} values of these nanotubes range within 13 kΩ - 170 kΩ as shown in Fig. 6.8. There were other MWNT devices with R_{ON} up to 800 kΩ probably due to poor metal-tube contact or presence of local defects in some nanotubes. The lowest achievable R_{ON} at 300 K is nearly twice the quantum limit of resistance in SWNTs ($h/4e^2$ =6.5 kΩ). In general, nanotube devices with small diameters have higher R_{ON} at room 300 K as compared to those with large diameter. However, the diameter dependence of R_{ON} is weak for tubes with length below 1.5 μm, indicating that transport in the nanotube is more ballistic in nature in short nanotubes and the resistances are largely from the contacts to the metal electrodes. Similar weak diameter dependence has also been reported in Pd contacted SWNTs [86].

On the other hand, it is observed that, as a function of length, the minimum R_{ON} increases as the length L increases beyond 1 μm. The length dependence of R_{ON} is also consistent in nanotubes where two or three devices are made with different lengths. We may apply equation 3.10 from section 6.6 to this length dependence and to fit the formula to the black solid line in figure 6.8. This would give:

$$R_{300K} = R_{contact} + R_{tube} = 10\,k\Omega + 7\,k\Omega/\mu m * L \tag{6.1}$$

From this we would infer, as the best values obtained among our devices, a contact resistance of 10 kΩ, which is ≈ 4 kΩ more than the quantum of resistance in SWNTs, and a one-dimensional resistivity of 7 kΩ/μm. The scaling of resistance with length is evidence of localization effects, as discussed in section 6.2.1.

The temperature coefficient of resistivity is the derivative of $R(T)$ with respect to the temperature. From figure 6.8 we see that for the 300 K $R_{ON} \approx 27$ kΩ, the temperature coefficient of resistivity is about constant and this value is a kind of demarcation line, indicated in the figure with a dashed line, between positive values for the coefficient, for 300 K R_{ON} < 27 kΩ, and negative values for R_{ON} > 27 kΩ. At 4.2 K R_{ON} ranged from 13 kΩ to several megaohms, beyond the scale of fig. 6.8. The lowest achievable minimum onstate resistance at 4.2 K is also nearly twice the quantum limit of resistance in SWNTs ($h/4e^2$ =6.5 kΩ). The only exception was one sample with $D \approx 7$ nm which exhibited $R_{ON} \approx 5$ kΩ. The onstate conductance variations in the intermediate temperature range are shown in more detail in fig. 6.9.

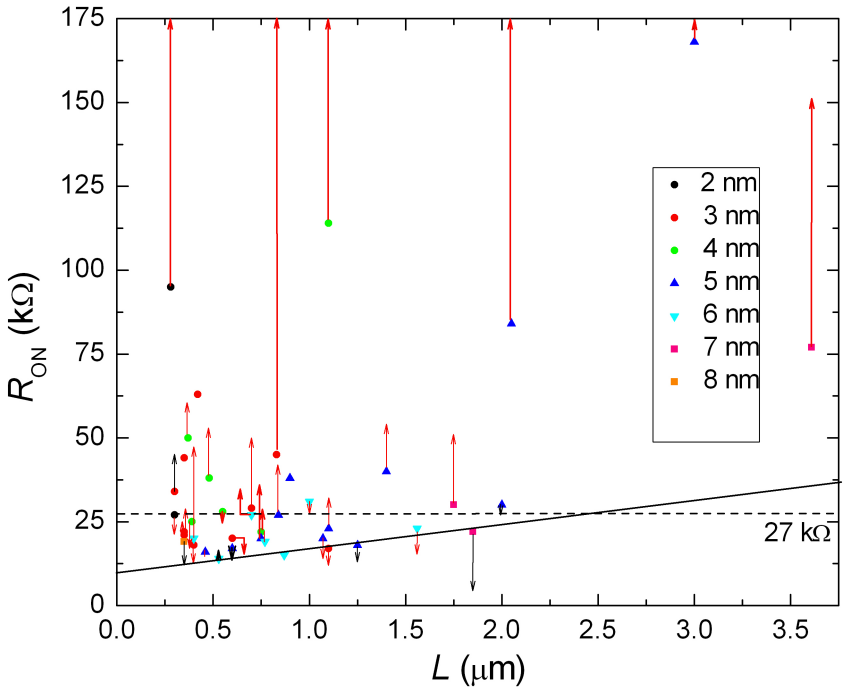

FIGURE 6.8 Minimum onstate resistance (R_{MIN}) at 300 K (dot) and 4.2 K (arrow tip). The black solid line (equation 6.1) and the dashed line (27 kΩ) are explained in the text.

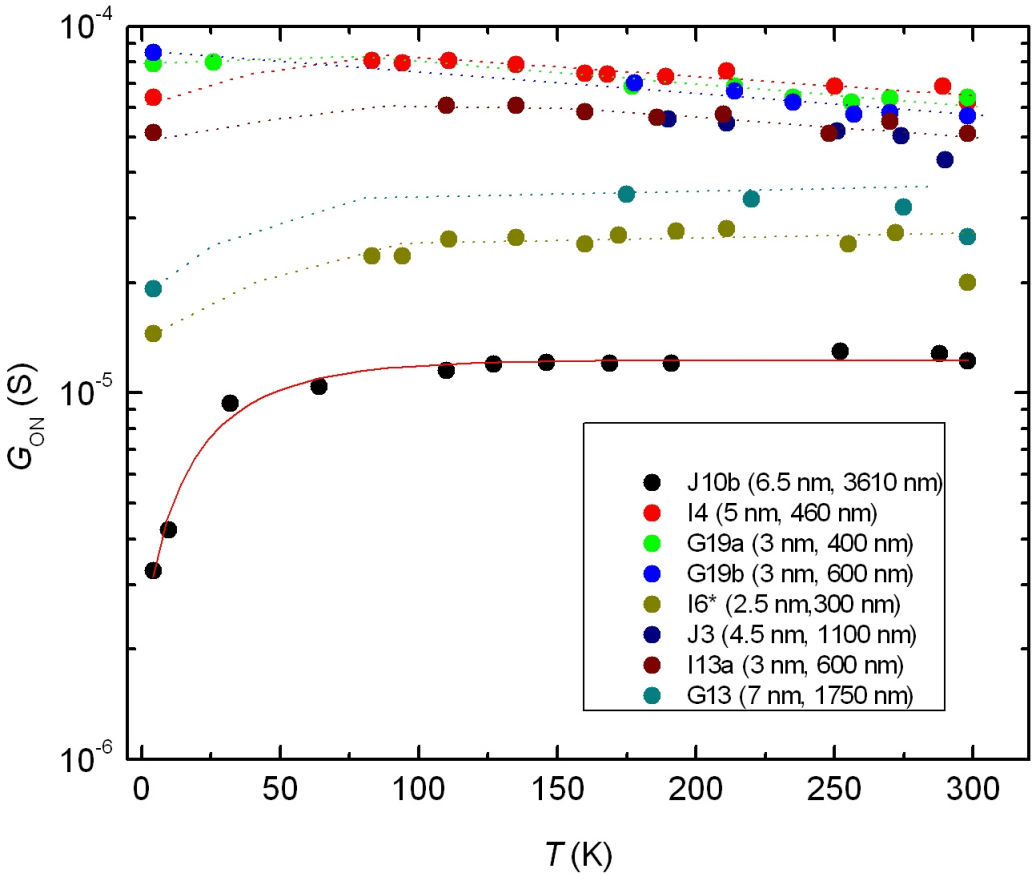

FIGURE 6.9 Plot of onstate conductance versus temperature for many samples.

6.4.2 Size dependence of the Resistance ratio

In this and the following sections the transport gap is investigated. The visibility or shape of the transport gap at room temperature varies significantly among the samples. A quantity that describes it in a simple way at room temperature is the resistance ratio $R_r = R_{OFF}/R_{ON}$, where R_{OFF} (and R_{ON}) was defined earlier in this section. The resistance ratios are shown in two separate figures in 6.10. In (a) are shown samples with D < 5 nm and in (b) with D => 5 nm. On inspection of the figures we see that among the small D devices there is a huge, overwhelming scatter of the R_r values, while among the larger D tubes this scatter is clearly connected to a L-dependence; at small L, all tubes have a low R_r value, which then increases as L increases.

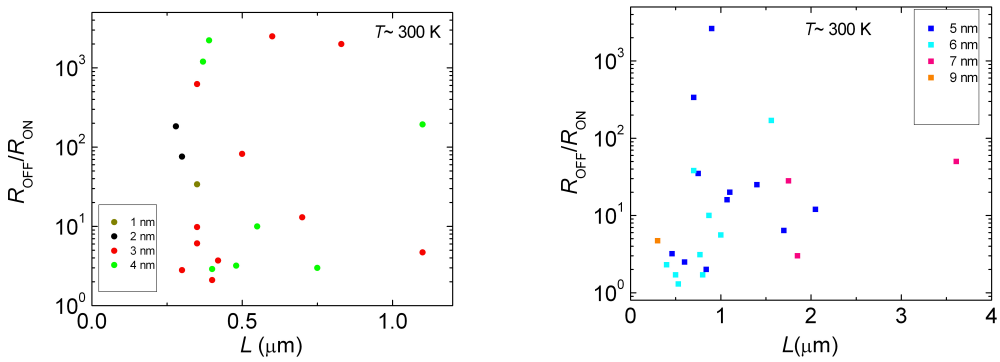

(a) (b)

FIGURE 6.10 Size dependence of resistance ratios at room temperature for (a) small diameter nanotubes and (b) large diameter nanotubes.

6.4.3 Size and temperature dependence of maximum offstate resistance

The transport gap becomes increasingly prominent as temperature is decreased. We characterize this with the temperature dependence of R_{OFF}. The relation of this quantity to the semiconducting gap, under certain simplifying assumptions, was discussed in section 3.3.2. The resistance of the MWNT device can be related to the temperature using equation (6.2)

$$R_{OFF} \propto \exp\left(\frac{\alpha}{k_B T}\right) \tag{6.2}$$

where we have replaced E_g with α, for reasons to be discussed later. The temperature dependence of the logarithm of R_{OFF} vs. the inverse temperature $1/T$ is shown in Fig.6.11, for two samples. The data was collected from gate curves at different temperatures, so it represents R_{OFF} very well, but is composed in most cases of rather few data points, since taking a gate curve at a steady temperature is time consuming. Within some temperature range near room temperature the $\log(R_{OFF})$ is inversely proportional to temperature. The overall temperature dependence of minimum conductance of these MWNT devices bears some resemblance to temperature dependence observed recently in graphene nanoribbons, as was discussed in section 3.3.8.

For each sample this Arrhenius type activated transport model fits rather well the inverse T dependence transport at higher temperatures. Generally, this thermally activated transport behavior is seen in the temperature range 300 K to 150 K. Below 150 K (varies from sample to sample) there is deviation of R_{OFF} from this behaviour as the resistance saturates, in some cases slightly and in others strongly. As with most high resistance measurements (in range 10 MΩ to 100 GΩ), there arise a question of whether such kind of deviation or saturation is real or a reflection of instrument measurement limitation. In our work, we measure large offstate resistances by taking slowly scanned IV curves with amplifier sensitivity or gain settings that allow reliable sub-pA current measurements allowing zero bias resistance measurements up to 50 GΩ.

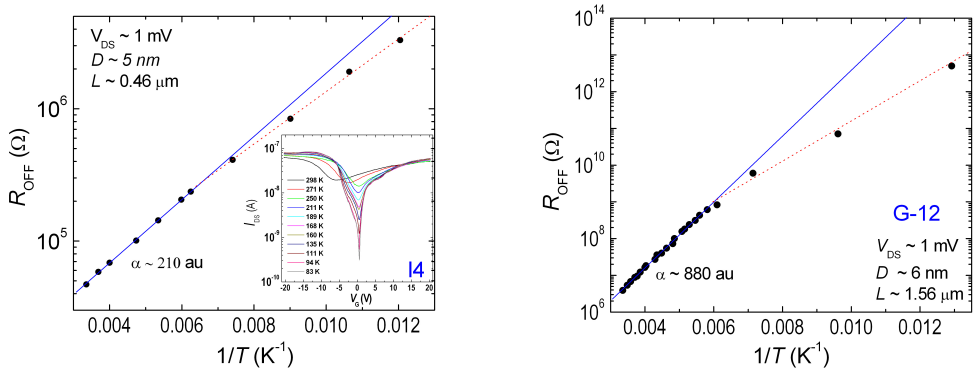

(a) (b)

FIGURE 6.11 Temperature dependence of R_{OFF} for (a) sample I4 and (b) sample G12.

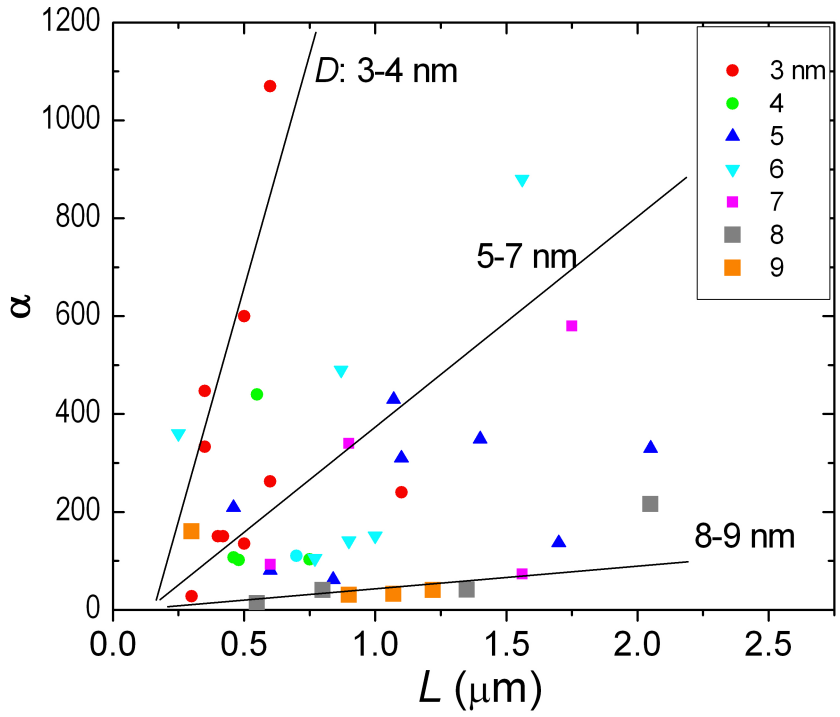

FIGURE 6.12 Plot of slopes α vs. L for tubes of different diameters.

From the slopes of log R_{OFF} vs. $1/T$, we obtain the α-values for each measured MWNT. For a large set of samples, the α values are plotted as a function of length in Fig. 6.12, with different diameters represented with separate labels, just as with the plot of fig. 6.10 for the resistance ratios. In the figure, there is a significant scatter, but we have placed three lines as a guide to the eye. The three lines represent rough average behaviour for the L-dependence of the α values for MWNTs of diameter 3-4 nm, 5-7 nm, and 8-9 nm, respectively. Again, the scatter of the data is strong but the overall trend for the combined D- and L-dependence is unambiguous. We can thus observe that the slopes of α vs. L plots dramatically increase with diameter. We may note here, that in samples with two devices on one tube (e.g. G19a and G19b) the longer section shows a larger value of slope (α).

Moreover, as we noted in section 3.3.7, nearly all previous published work on MWNTs has been done on tubes of $D > 10$ nm. Since in the previous works transport gaps have very rarely been observed, in the figure above we see that all of that would be placed on this kind of a plot along the x-axis at the bottom of the plot.

6.4.4 Size dependence of the bias voltage gap

Within the TG (= transport gap), the zero bias conductance ultimately becomes zero upon decreasing temperature, in the zero temperature limit. One may characterize the TG at low temperature by measuring conductance at the gate voltage corresponding to the charge neutrality point. In this case, where the zero bias conductance disappears, one can increase the bias voltage both on the negative and positive sides until a measurable current/conductance appears. In other words, taking an $I - V_{DS}$ curve at the gate voltage corresponding to the charge neutrality point. By adding the magnitudes of the voltages on the negative and positive sides one obtains the total bias voltage range, labeled ΔU_B, within which the nanotube device remains nonconducting (in the limit of resolution of measurement). Moreover, this quantity is sought at the gate voltage that maximizes it, which is usually near the charge neutrality point. Fig. 6.13(a) shows how this quantity can be obtained from an IV-curve at the particular gate voltage.

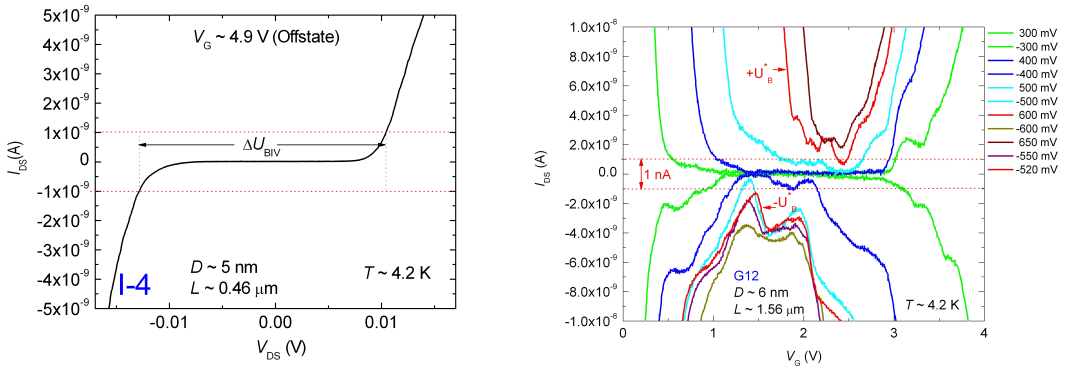

(a) (b)

FIGURE 6.13 Methods of measuring nonlinear gaps. (a) IV curve for sample I4 showing the nonlinear gap ΔU_{BIV} of $25mV$. (b) A typical measurement of ΔU_B that involves taking gate curves at different bias voltages,in this case for sample G12. We call this gap ΔU_{BG}. The ΔU_B is estimated from the gate curves whose offstate current is approximately 1 nA, in this case the red gate curves.

The method outlined above, however, may not be satisfactory, since setting the zero-current region is necessarily quite arbitrary, and if the bias voltages become comparable to the gate voltages, then it may complicate the situation due to so called self-gating effects. More systematic determination of the zero current region is obtained by taking gate curves with increasing positive and negative bias voltages. Then at a certain magnitude of the bias voltage the TG no longer drops to

zero at any V_G. These magnitudes of the bias voltages define the ΔU_B. An example is shown in Fig. 6.13(b).

The size dependence of ΔU_B is shown in Fig. 6.14, again separately for small (D < 5 nm) and larger ($D \geq 5$ nm). Short nanotube devices (i.e small L) with large diameters ($D \approx 8$ nm) exhibited very small or no transport gap ΔU_B whereas nanotube devices with small D (1-4 nm) had very big transport gaps regardless of length. Intermediate sized nanotubes (5-7 nm) had gaps that were strongly length dependent. For the later group samples with small L (0.3 - 1 μm) had small gaps and those with large L (1-3 μm) had big gaps. In other words, the results for the size dependent behaviour of ΔU_B are similar to those of R_r and α.

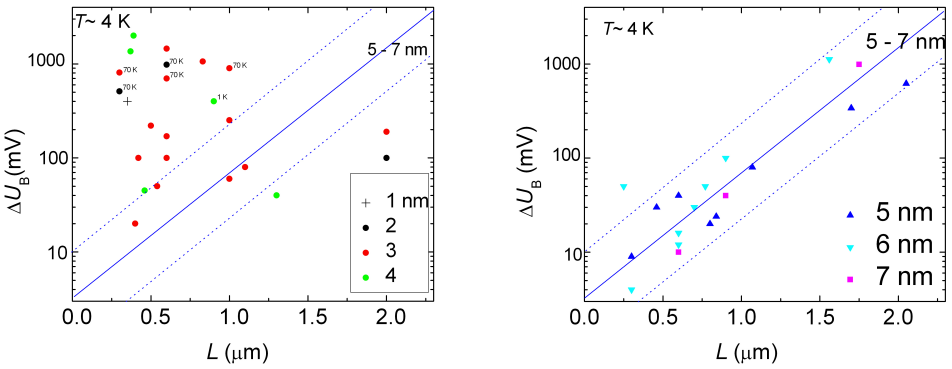

(a) (b)

FIGURE 6.14 Nonlinear IV gap ΔU_B (a) vs. L for samples with diameters 1 nm to 4 nm and (b) for nanotubes with diameter 5 nm to 7 nm.

6.4.5 Coulomb blockade oscillations

Coulomb oscillations are observed within the TG of the gate response curves at low temperature as shown in (Fig 6.15) (a) and (b). Such Coulomb oscillations correspond to tunneling events within the CNTs, when the gate voltage modifies tunnelling barriers between the "bulk" of the CNT and the contact region to the metal electrode. The oscillations appear only at low temperatures. Figure 6.15(c) shows one example of their temperature dependence. At 40 K the oscillations are only barely discernible.

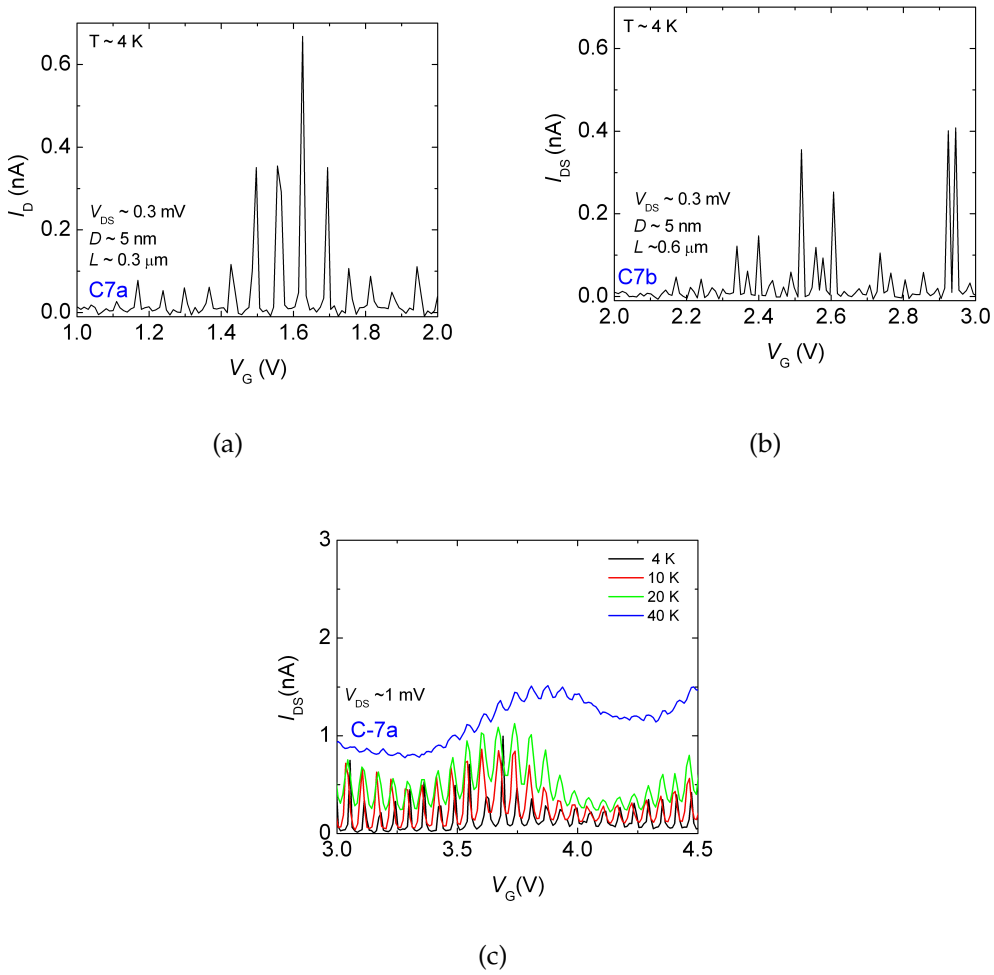

FIGURE 6.15 Coulomb blockade oscillations in a tube with different sections. (a) Shorter section. (b) Longer section. (c) The oscillations get washed out as temperature is increased.

It is found that the oscillations form and periodicity vary from sample to sample indicating possible length and diameter dependence. Size dependence is first investigated in MWNT devices with two different sections of different lengths as shown in (Fig 6.15) and Table 6.16. The oscillation periodicity have been measured in both the negative and positive gate voltage sides which correspond to hole and electron transport respectively [107]. For a fixed diameter, the oscillation period is higher in a shorter segment than in a longer one. This result can be explained in terms of the capacitance of the quantum dot which is proportional to the length of the CNT segment $C \approx L$. Coulomb oscillation periods in single electron tunneling devices are given as $\delta V = e/C$, on account of charging energy of the quantum dot $U \approx e^2/2C$.

Sample	p-type periodicity δV_{G-} (mV)	n-type periodicity δV_{G+} (mV)	Length L (µm)	Diameter D(nm)
B_5A	75	55	0.3	5
B_5B	75†	23	0.6	5
C_7A	90	65	0.3	5
C_7B	70	20-28**	0.6	5
C_3A	70	70	0.3	3
C_3B	35†	30-33†**	0.6	3

† Irregular, ** Double peaks

FIGURE 6.16 Coulomb oscillation periodicity(peak spacings). Samples B5a and B5b are the two sections of sample in Fig. 6.3(b)

It is further observed that the oscillations are much more regular in shorter segments, which is understandable as a result of the better coherence of the charge carrier wave function within the segment. The regular Coulomb oscillations correspond to single electron transport on one well-defined quantum dot. The irregular peaks in longer devices may indicate a presence of a series of quantum dots along the CNT, due to defects. Such electronically serial quantum dots are usually manifested as stochastic Coulomb diamonds in single electron spectroscopy experiments in SWNTs and graphene nanoribbons fabricated on SiO_2 substrate [5], [76], [108], [109], [110], [71].

6.5 Metallic and quasimetallic MWNTs

Recalling figure 6.3, we noted that some, but a clear minority of MWNT devices studied in this work exhibited low finite resistances at all gate voltages point even at low temperature as was shown in figure 6.4(d). More cases are shown in figure 6.17. Moreover, figure 6.3 shows that the metallic cases began to be numerous among the larger diameter devices. This is understandable from the point of view that the large diameter results in small E_g and thus thermal smearing of the bandgap. Case (c), shows that the TG can be rather small and that borderline, or quasimetallic cases do exist.

The metallicity in small diameter devices (≈ 3 nm) indicate that they are armchair or zigzag type. The metallic like behavior of large diameter nanotube may

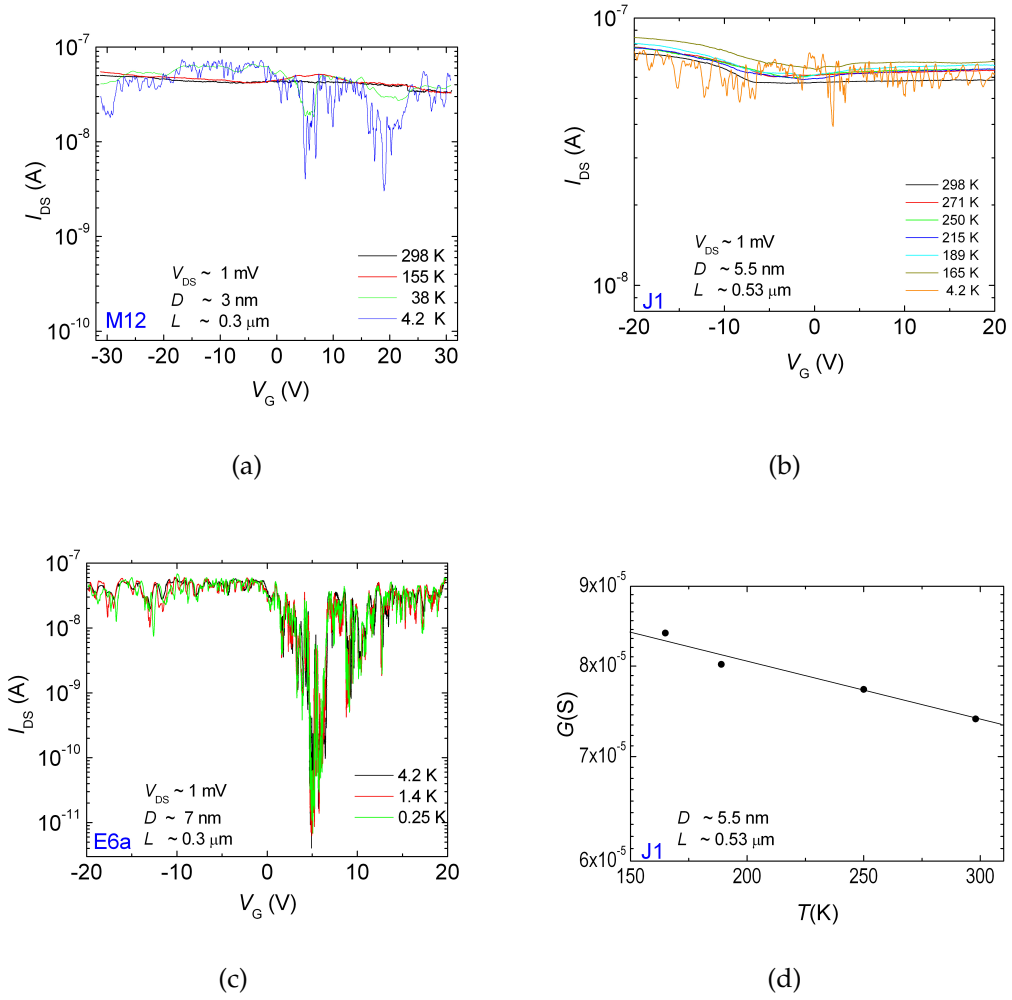

FIGURE 6.17 Gate and temperature dependent transport of metallic and quasimetallic nanotubes devices. (a) Sample M12 (D 3 nm, L 0.3 μm), (b) Sample J1, (c) Sample E6a (D 7 nm, L 300 nm). (d) Temperature dependence of baseline onstate conductance of sample J1.

arise from either chirality or very small band gaps (Fig.6.17(c)). For these very small band gapped ones the offstate resistance becomes infinite at very low T. As pointed out in the transport theory section out that true metallic nanotubes are rare owing to pseudogaps [68] that may arise from curvature, buckling and defects, some devices in this category may exhibit some weak semiconducting behaviour. Other small dips observed in gate curves may be due to Coulomb gaps arising from e-e interactions [51].

From figures 6.17(a),(b) and (c) we find that in some samples the on-state conductance increases with decreasing temperature whereas in other devices it does

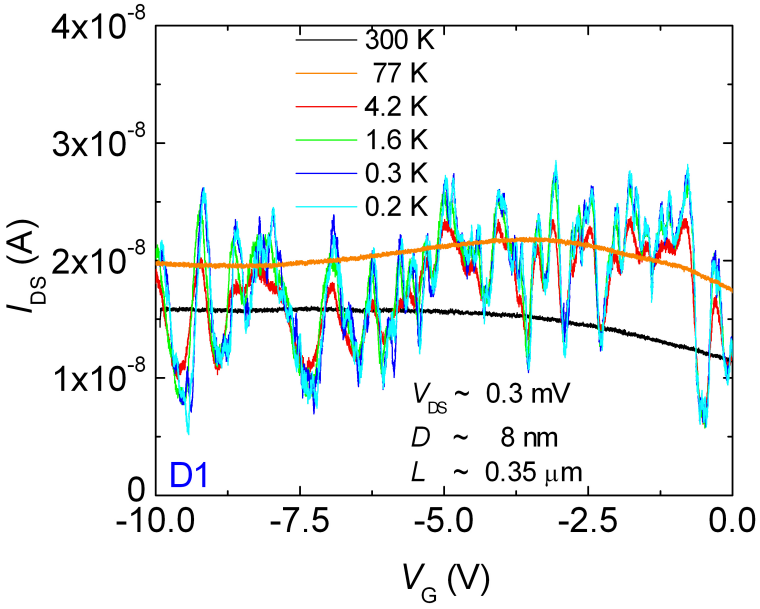

FIGURE 6.18 Onstate conductance oscillations in a metallic nanotube.

not vary with decreasing T save for the oscillations that get more pronounced at low temperature. The variation of on-state conductance with temperature is also shown in figure 6.17(d). For samples that exhibit slightly more p-type dominance two kinds of offstate conductance temperature dependences are observed. For instance, in figure 6.4(d) the offstate region conductance increases with increasing temperature whereas in 6.17(b) there is a decrease in offstate conductance as temperature is increased.

In quasimetallic nanotubes zero-bias gate curves at very low temperatures exhibit strong conductance oscillations as shown in figure 6.18. These oscillations are not seen in room temperature data. The oscillations have multiple periodicities. Many MWNTs devices in this work exhibited aperiodic oscillations. Oscillations in some devices (e.g. D1) are Fabry-Perot resonances (Fig. 6.18) [40], [111] which are known to occur in samples with high contact transparency. In the case of D1 the onstate resistance fluctuates in the range 11 kΩ to 40 kΩ (corresponding to a conductance range of 2.2 e^2/h to 0.6 e^2/h. Such conductances are relatively closer to the ballistic limit of SWNTs. The oscillations are found to be irregular. Similar irregularities have been observed in clean suspended SWNTs and were attributed to imperfections in the device [37].

6.6 Conclusions on transport in intermediate sized multiwall nanotubes

From the results presented in section 6.4 on gapped MWNTs and section 6.5 on metallic and quasimetallic MWNTs, we may see that they in particular bring in new information on the size dependence of transport in MWNTs. The combined results presented on the gapped MWNT devices contain some sizable scatter in the D- and L-dependence of the measured quantities, but clearly point towards some conclusions.

Firstly, in the shortest devices, with $L < 0.5$ μm, only the small diameter MWNTs have large values for R_r, α and ΔU_B. Moreover, the small diameter MWNTs exhibit a large distribution of values, over orders of magnitude. The large spread of data for small diameter can be interpreted as the tendency for a share of the small diameter nanotubes to form armchair structure, as observed by Hirahara *et al.* [85], which then are rather metallic with small observable gaps that can be explained as small pseudo-gaps of less than 100 meV that may arise from curvature or e-e interactions [51]. Secondly, the larger diameter tubes always exhibit small values for R_r, α and ΔU_B at small lengths, but these values increase linearly, on the average, with increasing length.

A primary natural explanation for this behaviour is to infer the diameter dependence for the single shell E_g, eq. 3.2 in section 3.3.1, so that this relation is set to apply for the outer layer or layers of the MWNT. The diameter dependence can therefore be interpreted in terms of bandgaps that are theoretically predicted to be inversely proportional to diameter, and that as such show up in the measurements reported in this thesis. On the other hand, the linear increase of R_r, α and ΔU_B with increasing length is attributed to localization effects due to structural disorder.

The localization effects are visible also in the on-state resistances R_{ON} of figures 6.8 and 6.9. Referring in particular to the latter, the behaviour of the collection of these devices is familiar from systems on the boundary of the metal-insulator transition. Tubes with the least disorder (with the 300 K R_{ON} < 27 kΩ) have a positive temperature coefficient of resistivity which turns to negative as R_{ON} increases. The 27 kΩ resistance may then be a system-specific metal-insulator transition boundary marker value where the transition is driven by disorder driven localization. The localization then of course becomes more severe the longer the device is.

The weak temperature dependence (saturation)of R_{ON}, especially in larger diameter MWNTs, in our samples is drastically different from the reported decrease in conductance in SWNTs [33] as the temperature decreases below 150 K. Temperature dependence in those long SWNTs of lengths about 3 - 4 μm and diameters about 1-2 nm had upturn and downturn within 4 K to 300 K which was attributed to impurity scattering and acoustic phonon scattering [33]. The decrease in conductance is also associated with Coulomb blockade [34]. That difference in behaviour is further testimony to the strong dependence of carbon nanotubes on diameter, with respect to their electronic properties.

6.7 Future outlook

Basic electrical properties of nearly a 100 sub-10 nm nanotubes have been explored. Most of the nanotube devices studied in this thesis have channel length below 2 μm. More nanotubes of length 2 to 10 μm will be needed to enhance the length dependence studies. This may require nanotube materials made via CVD synthesis techniques that can yield ultralong multiwall nanotubes. Combined transport, Raman spectroscopy and transmission electron microscopy (TEM) studies would also be important. The Raman studies will be useful in quantifying both bandgaps and defects. The TEM studies will help in counting the number of walls in each multiwall device. Such combined studies would require fabricating suspended nanotube devices. After doing the transport, Raman and TEM studies the next step would be to exfoliate the outer walls one-by-one to study the chiralities of inner walls. More systematic studies of field dependence of conductance will be needed to clarify the transport mechanisms behind non-linear current-voltage behaviour in multiwall nanotubes. Experiments on negative differential resistance, magnetoresistance and noise to shed more light on electron dynamics in these complex systems. Concerning application of these multiwall nanotube as field effect transistor and memory devices performance analysis studies on parameters such as subthreshold slopes and switching speed will be needed.

Chapter 7

Summary

In this thesis experimental studies of two kinds of nanoscale carbon based electrically conducting materials - conducting polymers (CP) and intermediate sized multiwall carbon nanotubes (MWNT) was presented, with emphasis on size and temperature dependences of their electrical properties. The importance of these materials is two-fold; they offer opportunity for fundamental study of physics of low dimensional systems and also have potential for electronics applications. The order of presentation of material in this thesis is from conducting polymers to multiwall nanotubes which is also the chronological order of our works on these materials.

In chapter 5 we present a novel fabrication technique for sub-200 nm hybrid polypyrrole-gold thin films with conductivity comparable to conductivity of bulky disordered highly doped polypyrrole CPs. The central idea is to electropolymerize pyrrole on a gold island nanolayer of nominal thickness less than 7 nm. Such discontinuous gold films are below percolation threshold and have nanoscale inter-island gaps that are rapidly bridged by the growing polymer. The width of the polymer-gold film can be defined by the width of the gold film which can be in nanometer regime. This fabrication technique complements the previous works on sub-micron CPs. It further provides a composite system where transport at nanoscale size corresponding to nanoscale inter-island gaps can be studied.

Temperature dependence of zero bias resistance of four samples of thickness 30 to 200 nm films show a Mott 3D variable range hopping transport behaviour in temperature range 20 K to 300 K. At lower temperature the current voltage characteristics curves are generally nonlinear with field dependences that can be described by a phenomenological model that differ from conventional V^2 and $V^{-1/4}$ reported predicted by theory. We are unaware of transport theory that would exactly match our our measurement results, which is understandable considering the composite

nature of our system. This peculiar field dependence show that hybrid system like metal-CP nanostructures are interesting to explore novel transport phenomena. In future more systematic field dependence studies on many of these samples could shed more light on the charge transport in these systems.

From our literature review on nanotubes, we found that most of reported previous works have been on small diameter SWNTs (D < 3 nm) and large diameter MWNTs (D > 10 nm). The range 3-10 nm MWNT was not adequately explored. The main reason for lack of studies in this diameter range is scarcity of clean MWNTs nanotubes in the sub-10 nm regime due to synthesis challenges. The reason for study bias towards SWNTs and very large diameter nanotubes relates to structural simplicity of SWNT vis-a-vis MWNTs. We have done an extensive study of basic transport properties of MWNT nanotubes that bridges the rather unexplored 3-10 nm diameter range. We found nanotubes of this diameter range in a nanotube powder of catalyst-free arc-discharge synthesized nanotubes obtained from Iijima. If one imagines unwrapping nanotubes of such diameters the resulting graphene nanoribbons would have widths in the range 9 to 32 nm. It is currently difficult to fabricate clean graphene nanoribbons this small. In a few recent works on narrow graphene nanoribbons of width 20 to 100 nm transport gaps have been observed in gatecurves that bear remarkable resemblance with our results on nanotubes devices.

From gate-controlled conductance measurements on 100 multiwall nanotube devices, we found 25 of them exhibit metallic-like behaviour and 75 to be semiconducting (or gapped). We focussed our studies on the gapped ones. Within the 3-8 nanometer regime we find transport gaps (or regions of low conduction in gatecurves) that become more pronounced at lower temperature. The transport gap features vary from sample to sample indicating diameter and length dependence.

To quantify the gaps we studied temperature dependences of offstate resistance. We found an Arrhenius-type thermally activated transport behaviour within 100 to 300 K in our samples with slopes that scale with length and diameter. Current-voltage characteristics of the offstate and field dependent gate curves were used to measure nonlinear IV gaps that scale with length of samples. We found also some correlations in the length and diameter dependences of α, nonlinear IV gaps and room temperature resistance ratios. The work presented in this thesis is unique in that it bridges previous works on SWNTs and larger diameter MWNTs, of which in the latter transport gaps had hardly ever been observed before.

Bibliography

[1] CHARLIER, J.-C., BLASE, X., AND ROCHE, S., *Electronic and transport properties of nanotubes*. Rev.Mod.Phys. **79** (2007) 677–732.

[2] JAISWAL, M. AND MENON, R., *Polymer electronic materials: a review of charge transport*. Polymer International **55** (2006) 1371–1384.

[3] HEEGER, A., *Nobel Lecture: Semiconducting and metallic polymers: The fourth generation of polymeric materials*. Rev. Mod. Phys. **73** (2001) 681–700.

[4] YOON, C., REGHU, M., MOSES, D., AND HEEGER, A., *Transport near the metal-insulator-transition in polypyrrole doped with PF_6 (VOL 49, PG 10851, 1994)*. Phys. Rev. B **50** (1994) 8138.

[5] STOKES, P. AND KHONDAKER, S. I., *Evaluating Defects in Solution-Processed Carbon Nanotube Devices via Low-Temperature Transport Spectroscopy*. ACS Nano **4** (2010) 2659–2666.

[6] IMRY, Y., *Introduction to Mesoscopic Physics* (Oxford University Press, 1997).

[7] HUANG, J., VIRJI, S., WEILLER, B., AND KANER, R., *Polyaniline nanofibers: Facile synthesis and chemical sensors*. Journal of the American Chemical Society **125** (2003) 314–315.

[8] HUANG, J. AND KANER, R., *A general chemical route to polyaniline nanofibers*. Journal of the American Chemical Society **126** (2004) 851–855.

[9] PARK, J., KIM, B., LEE, S., AND PARK, Y., *Current-voltage characteristics of polypyrrole nanotube in both vertical and lateral electrodes configuration*. Thin Solid Films **438** (2003) 118–122.

[10] CHO, S., SONG, K., AND J, L., *Recent Advances in Polypyrrole, Handbook of Conducting Polymers. 3rd edition* (Florida CRC Press, 1998).

[11] YIN, Z.-H., LONG, Y.-Z., GU, C.-Z., WAN, M.-X., AND DUVAIL, J.-L., *Current-Voltage Characteristics in Individual Polypyrrole Nanotube, Poly(3,4-ethylenedioxythiophene) Nanowire, Polyaniline Nanotube, and CdS Nanorope*. Nanoscale Res. Lett. **4** (2009) 63–69.

[12] LONG, Y. Z., DUVAIL, J. L., LI, M. M., GU, C., LIU, Z., AND RINGER, S. P., *Electrical Conductivity Studies on Individual Conjugated Polymer Nanowires: Two-Probe and Four-Probe Results*. Nanoscale Res. Lett. **5** (2010) 237–242.

[13] HEEGER, A., KIVELSON, S., SCHRIEFFER, J., AND SU, W., *Solitons in conducting polymers*. Rev. Mod. Phys. **60** (1988) 781–850.

[14] MAYNOR, B. W., FILOCAMO, S. F., GRINSTAFF, M. W., AND LIU, J., *Direct-writing of polymer nanostructures:â poly(thiophene) nanowires on semiconducting and insulating surfaces*. Journal of the American Chemical Society **124** (2002) 522–523.

[15] ROSENBAUM, R., *Crossover from Mott to Efros-Schlovskii variable-range-hopping conductivity in inoxy films*. Phys. Rev. B **44** (1991) 3599–3603.

[16] SHENG, P., *Fluctuation-induced tunneling conduction in disordered materials*. Phys. Rev. B **21** (1980) 2180–2195.

[17] PARK, J., KIM, G., KRSTIC, V., KIM, B., LEE, S., ROTH, S., BURGHARD, M., AND PARK, Y., *Nanotransport in polyacetylene single fiber: Toward the intrinsic properties*. Synthetic Metals **119** (2001) 53–56.

[18] ALESHIN, A., LEE, H., AKAGI, K., AND PARK, Y., *One-dimensional transport in polymer nanowires*. Microelectronic Engineering **81** (2005) 420–427.

[19] ALESHIN, A. N., LEE, H. J., PARK, Y. W., AND AKAGI, K., *One-dimensional transport in polymer nanofibers*. Phys. Rev. Lett. **93** (2004) 196601.

[20] GENCE, L., FANIEL, S., GUSTIN, C., MELINTE, S., BAYOT, V., CALLEGARI, V., REYNES, O., AND DEMOUSTIER-CHAMPAGNE, S., *Structural and electrical characterization of hybrid metal-polypyrrole nanowires*. Phys. Rev. B **76** (2007) 1154151.

[21] HE, H., LI, X., TAO, N., NAGAHARA, L., AMLANI, I., AND TSUI, R., *Discrete conductance switching in conducting polymer wires*. Phys. Rev. B **68** (2003) 045302.

[22] PALOHEIMO, J., STUBB, H., AND GRONBERG, L., *Field-effect transport in conjugated polymers/Oligomers between metal islands*. Synthetic Metals **57** (1993) 4198–4203.

[23] NISHIZAWA, M., SHIBUYA, M., SAWAGUCHI, T., MATSUE, T., AND UCHIDA, I., *Electrochemical preparation of ultrathin polypyrrole film at microarray electrodes*. J. Phys. Chem. **95** (1991) 9042–9044.

[24] NISHIZAWA, M., NOZAKI, H., KAJI, H., KITAZUME, T., KOBAYASHI, N., ISHIBASHI, T., AND ABE, T., *Electrodeposition of anchored polypyrrole film on microelectrodes and stimulation of cultured cardiac myocytes*. Biomaterials **28** (2007) 1480–1485.

[25] SU, M., FU, L., WU, N., ASLAM, M., AND DRAVID, V., *Individually addressed large-scale patterning of conducting polymers by localized electric fields*. Appl. Phys. Lett. **84** (2004) 828–830.

[26] BOUILLY, D., CABANA, J., MEUNIER, F., DESJARDINS-CARRIERE, M., LAPOINTE, F., GAGNON, P., LAROUCHE, F. L., ADAM, E., PAILLET, M., AND MARTEL, R., *Wall-Selective Probing of Double-Walled Carbon Nanotubes Using Covalent Functionalization*. ACS Nano **5** (2011) 4927–4934.

[27] LEHMAN, J., TERRONES, M., MANSFIELD, E., HURST, K., AND MEUNIER, V., *Evaluating the characteristics of multiwall carbon nanotubes*. Carbon **49** (2011) 2581 – 2602.

[28] MANIWA, Y., FUJIWARA, R., KIRA, H., TOU, H., NISHIBORI, E., TAKATA, M., SAKATA, M., FUJIWARA, A., ZHAO, X., IIJIMA, S., AND ANDO, Y., *Multiwalled carbon nanotubes grown in hydrogen atmosphere: An x-ray diffraction study*. Phys. Rev. B **64** (2001) 073105.

[29] NYGARD, J., *Old nanotubes, new tricks*. Nature Physics **4** (2008) 266–267.

[30] DESHPANDE, V. V. AND BOCKRATH, M., *The one-dimensional Wigner crystal in carbon nanotubes*. Nature Physics **4** (2008) 314–318.

[31] STEELE, G. A., GOTZ, G., AND KOUWENHOVEN, L. P., *Tunable few-electron double quantum dots and Klein tunnelling in ultraclean carbon nanotubes*. Nature Nanotechnology **4** (2009) 363–367.

[32] KUEMMETH, F., ILANI, S., RALPH, D. C., AND MCEUEN, P. L., *Coupling of spin and orbital motion of electrons in carbon nanotubes*. Nature **452** (2008) 448–452.

[33] JAVEY, A., GUO, J., WANG, Q., LUNDSTROM, M., AND DAI, H., *Ballistic carbon nanotube field-effect transistors*. Nature **424** (2003) 654–657.

[34] ZHOU, X., PARK, J., HUANG, S., LIU, J., AND MCEUEN, P., *Band structure, phonon scattering, and the performance limit of single-walled carbon nanotube transistors*. Phys. Rev. Lett. **95** (2005) 146805.

[35] ZHOU, C., KONG, J., AND DAI, H., *Intrinsic electrical properties of individual single-walled carbon nanotubes with small band gaps*. Phys. Rev. Lett. **84** (2000) 5604–5607.

[36] ZHOU, C., KONG, J., AND DAI, H., *Electrical measurements of individual semiconducting single-walled carbon nanotubes of various diameters*. Appl. Phys. Lett. **76** (2000) 1597–1599.

[37] CAO, J., WANG, Q., AND DAI, H., *Electron transport in very clean, as-grown suspended carbon nanotubes*. Nature Materials **4** (2005) 745–749.

[38] TANS, S., DEVORET, M., DAI, H., THESS, A., SMALLEY, R., GEERLIGS, L., AND DEKKER, C., *Individual single-wall carbon nanotubes as quantum wires*. Nature **386** (1997) 474–477.

[39] NYGARD, J., COBDEN, D., AND LINDELOF, P., *Kondo physics in carbon nanotubes*. Nature **408** (2000) 342–346.

[40] LIANG, W., BOCKRATH, M., BOZOVIC, D., HAFNER, J., TINKHAM, M., AND PARK, H., *Fabry-Perot interference in a nanotube electron waveguide*. Nature **411** (2001) 665–669.

[41] MINOT, E., YAISH, Y., SAZONOVA, V., AND MCEUEN, P., *Determination of electron orbital magnetic moments in carbon nanotubes*. Nature **428** (2004) 536–539.

[42] CAO, J., WANG, Q., ROLANDI, M., AND DAI, H., *Aharonov-bohm interference and beating in single-walled carbon-nanotube interferometers*. Phys. Rev. Lett. **93** (2004) 2168031.

[43] BABIC, B., KONTOS, T., AND SCHONENBERGER, C., *Kondo effect in carbon nanotubes at half filling*. Phys. Rev. B **70** (2004) 235419.

[44] SAPMAZ, S., JARILLO-HERRERO, P., KONG, J., DEKKER, C., KOUWENHOVEN, L., AND VAN DER ZANT, H., *Electronic excitation spectrum of metallic carbon nanotubes*. Phys. Rev. B **71** (2005) 153402.

[45] KONG, J., YENILMEZ, E., TOMBLER, T., KIM, W., DAI, H., LAUGHLIN, R., LIU, L., JAYANTHI, C., AND WU, S., *Quantum interference and ballistic transmission in nanotube electron waveguides*. Phys. Rev. Lett. **87** (2001) 106801.

[46] LIANG, W., BOCKRATH, M., AND PARK, H., *Shell filling and exchange coupling in metallic single-walled carbon nanotubes*. Phys. Rev. Lett. **88** (2002) 126801.

[47] PUREWAL, M. S., HONG, B. H., RAVI, A., CHANDRA, B., HONE, J., AND KIM, P., *Scaling of resistance and electron mean free path of single-walled carbon nanotubes*. Phys. Rev. Lett. **98** (2007) 186808.

[48] STOKES, P. AND KHONDAKER, S. I., *Controlled fabrication of single electron transistors from single-walled carbon nanotubes*. Appl. Phys. Lett. **92** (2008) 262107.

[49] MAKAROVSKI, A., LIU, J., AND FINKELSTEIN, G., *Evolution of transport regimes in carbon nanotube quantum dots*. Phys. Rev. Lett. **99** (2007) 066801.

[50] LETURCQ, R., STAMPFER, C., INDERBITZIN, K., DURRER, L., HIEROLD, C., MARIANI, E., SCHULTZ, M. G., VON OPPEN, F., AND ENSSLIN, K., *Franck-Condon blockade in suspended carbon nanotube quantum dots*. Nature Physics **5** (2009) 327–331.

[51] DESHPANDE, V. V., CHANDRA, B., CALDWELL, R., NOVIKOV, D. S., HONE, J., AND BOCKRATH, M., *Mott Insulating State in Ultraclean Carbon Nanotubes*. Science **323** (2009) 106–110.

[52] BACHTOLD, A., STRUNK, C., SALVETAT, J., BONARD, J., FORRO, L., NUSSBAUMER, T., AND SCHONENBERGER, C., *Aharonov-Bohm oscillations in carbon nanotubes*. Nature **397** (1999) 673–675.

[53] KANDA, A., TSUKAGOSHI, K., AOYAGI, Y., AND OOTUKA, Y., *Gate-voltage dependence of zero-bias anomalies in multiwall carbon nanotubes*. Phys. Rev. Lett. **92** (2004) 036801.

[54] TARKIAINEN, R., AHLSKOG, M., ZYUZIN, A., HAKONEN, P., AND PAALANEN, M., *Transport in strongly disordered multiwalled carbon nanotubes*. Phys. Rev. B **69** (2004) 033402.

[55] HUANG, J., CHEN, S., JO, S., WANG, Z., HAN, D., CHEN, G., DRESSELHAUS, M., AND REN, Z., *Atomic-scale imaging of wall-by-wall breakdown and concurrent transport measurements in multiwall carbon nanotubes*. Phys. Rev. Lett. **94** (2005) 236802.

[56] STOJETZ, B., MIKO, C., FORRO, L., AND STRUNK, C., *Effect of band structure on quantum interference in multiwall carbon nanotubes*. Phys. Rev. Lett. **94** (2005) 186802.

[57] ZHANG, Z. AND CHANDRASEKHAR, V., *Signatures of phase coherence in the low-temperature transport properties of multiwall carbon nanotubes*. Phys. Rev. B **73** (2006) 075421.

[58] NANOT, S., AVRILLER, R., ESCOFFIER, W., BROTO, J.-M., ROCHE, S., AND RAQUET, B., *Propagative Landau States and Fermi Level Pinning in Carbon Nanotubes*. Phys. Rev. Lett. **103** (2009) 256801.

[59] TSUKAGOSHI, K., ALPHENAAR, B., AND AGO, H., *Coherent transport of electron spin in a ferromagnetically contacted carbon nanotube*. Nature **401** (1999) 572–574.

[60] TARKIAINEN, R., AHLSKOG, M., PENTTILA, J., ROSCHIER, L., HAKONEN, P., PAALANEN, M., AND SONIN, E., *Multiwalled carbon nanotube: Luttinger versus Fermi liquid*. Phys. Rev. B **64** (2001) 195412.

[61] SCHONENBERGER, C., BACHTOLD, A., STRUNK, C., SALVETAT, J., AND FORRO, L., *Interference and Interaction in multi-wall carbon nanotubes*. Appl. Phys. A **69** (1999) 283–295.

[62] BOURLON, B., MIKO, C., FORRO, L., GLATTLI, D. C., AND BACHTOLD, A., *Beyond the linearity of current-voltage characteristics in multiwalled carbon nanotubes*. Semicond. Sci. Technol. **21** (2006) 33.

[63] AHLSKOG, M., HERRANEN, O., JOHANSSON, A., LEPPANIEMI, J., AND MTSUKO, D., *Electronic transport in intermediate sized carbon nanotubes*. Phys. Rev. B **79** (2009) 155408.

[64] FEDOROV, G., BARBARA, P., SMIRNOV, D., JIMENEZ, D., AND ROCHE, S., *Tuning the band gap of semiconducting carbon nanotube by an axial magnetic field*. Appl. Phys. Lett. **96** (2010) 132101.

[65] RAQUET, B., AVRILLER, R., LASSAGNE, B., NANOT, S., ESCOFFIER, W., BROTO, J.-M., AND ROCHE, S., *Onset of Landau-level formation in carbon-nanotube-based electronic Fabry-Perot resonators*. Phys. Rev. Lett. **101** (2008) 046803.

[66] KOSHIO, A., YUDASAKA, M., AND IIJIMA, S., *Metal-free production of high-quality multi-wall carbon nanotubes, in which the innermost nanotubes have a diameter of 0.4 nm*. Chemical Physics Letters **356** (2002) 595–600.

[67] RAO, R., LIPTAK, D., CHERUKURI, T., YAKOBSSON, B. M., AND MARUYAMA, B., *In situ evidence for chirality-dependent growth rates of individual carbon nanotubes*. Nature Materials Advance online publication (2012).

[68] BIERCUK, M. J., ILANI, S., MARCUS, C. M., AND MCEUEN, P. L., *Electrical transport in single-wall carbon nanotubes*, vol. 111 of *Topics in Applied Physics* (Springer-Verlag Berlin, 2008).

[69] LAMBIN, P., *Electronic structure of carbon nanotubes*. Comptes Rendus Physique **4** (2003) 1009–1019.

[70] JORIO, A., *Carbon Nanotubes:Advanced Topics in the Synthesis, Structure, Properties and Applications.* (Springer, 2001).

[71] SHIMIZU, T., HARUYAMA, J., MARCANO, D. C., KOSINKIN, D. V., TOUR, J. M., HIROSE, K., AND SUENAGA, K., *Large intrinsic energy bandgaps in annealed nanotube-derived graphene nanoribbons*. Nature Nanotechnology **6** (2011) 45–50.

[72] HAN, M. Y., BRANT, J. C., AND KIM, P., *Electron Transport in Disordered Graphene Nanoribbons*. Phys. Rev. Lett. **104** (2010) 056801.

[73] MINOT, E., YAISH, Y., SAZONOVA, V., PARK, J., BRINK, M., AND MCEUEN, P., *Tuning carbon nanotube band gaps with strain*. Phys. Rev. Lett. **90** (2003) 156401.

[74] FLORES, F., BIEL, B., RUBIO, A., GARCIA-VIDAL, F. J., GOMEZ-NAVARRO, C., DE PABLO, P., AND GOMEZ-HERRERO, J., *Anderson localization regime in carbon nanotubes: size dependent properties*. Journal of Physics-Condensed Matter **20** (2008) 304211.

[75] SAITO, R., DRESSELHAUS, G., AND DRESSELHAUS, M., *Physical properties of carbon nanotubes.* (Imperial College Press, 1999).

[76] GRAEBER, M. R., COISH, W. A., HOFFMANN, C., WEISS, M., FURER, J., OBERHOLZER, S., LOSS, D., AND SCHOENENBERGER, C., *Molecular states in carbon nanotube double quantum dots*. Phys. Rev. B **74** (2006) 075427.

[77] STRUNK, C. AND STOJETZ, B., *Aharonov-Bohm effects in multiwall carbon nanotubes*. Phys. Stat. Sol. B **243** (2006) 3365–3369.

[78] LAMBIN, P., MEUNIER, V., AND RUBIO, A., *Electronic structure of polychiral carbon nanotubes*. Phys. Rev. B **62** (2000) 5129–5135.

[79] SHEN, C., BROZENA, A. H., AND WANG, Y., *Double-walled carbon nanotubes: Challenges and opportunities*. Nanoscale **3** (2011) 503–518.

[80] COLLINS, P. AND AVOURIS, P., *Multishell conduction in multiwalled carbon nanotubes*. Appl. Phys. A **74** (2002) 329–332.

[81] TRIOZON, F., ROCHE, S., RUBIO, A., AND MAYOU, D., *Electrical transport in carbon nanotubes: Role of disorder and helical symmetries*. Phys. Rev. B **69** (2004) 121410.

[82] LANGER, L., BAYOT, V., GRIVEI, E., ISSI, J., HEREMANS, J., OLK, C., STOCKMAN, L., VANHAESENDONCK, C., AND BRUYNSERAEDE, Y., *Quantum transport in a multiwalled carbon nanotube*. Phys. Rev. Lett. **76** (1996) 479–482.

[83] BOURLON, B., MIKO, C., FORRO, L., GLATTLI, D., AND BACHTOLD, A., *Determination of the intershell conductance in multiwalled carbon nanotubes*. Phys. Rev. Lett. **93** (2004) 176806.

[84] KRSTIC, V., BLUMENTRITT, S., MUSTER, J., ROTH, S., AND RUBIO, A., *Role of disorder on transport in boron-doped multiwalled carbon nanotubes*. Phys. Rev. B **67** (2003) 041401.

[85] HIRAHARA, K., KOCIAK, M., BANDOW, S., NAKAHIRA, T., ITOH, K., SAITO, Y., AND IIJIMA, S., *Chirality correlation in double-wall carbon nanotubes as studied by electron diffraction*. Phys. Rev. B **73** (2006) 195420.

[86] TSENG, Y.-C., PHOA, K., CARLTON, D., AND BOKOR, J., *Effect of diameter variation in a large set of carbon nanotube transistors*. Nano. Lett. **6** (2006) 1364–1368.

[87] HAN, M. Y., OEZYILMAZ, B., ZHANG, Y., AND KIM, P., *Energy band-gap engineering of graphene nanoribbons*. Phys. Rev. Lett. **98** (2007) 206805.

[88] XU, G., TORRES, C. M., JR., TANG, J., BAI, J., SONG, E. B., HUANG, Y., DUAN, X., ZHANG, Y., AND WANG, K. L., *Edge Effect on Resistance Scaling Rules in Graphene Nanostructures*. Nano. Lett. **11** (2011) 1082–1086.

[89] NEMEC, N., TOMANEK, D., AND CUNIBERTI, G., *Contact dependence of carrier injection in carbon nanotubes: An ab initio study*. Phys. Rev. Lett. **96** (2006) 076802.

[90] JUN, W., MITCHELL, C., EGDELL, R., AND FOORD, J., *Real time STM observation of Au-assisted decomposition of SiO2 films on Si(111) at elevated temperatures*. Surface Science **506** (2002) 66–79.

[91] MORRIS, J. AND COUTTS, T., *Electrical conduction in discontinuous metal-films.Discussion*. Thin Solid Films **47** (1977) 3–65.

[92] HILL, R., *Electrical conduction in ultra thin metal films .I. Theoretical*. Proceedings of the Royal Soc of London Series A-Mathematical and Physical Sciences **309** (1969) 377.

[93] HILL, R., *Electrical conduction in ultra thin metal films.2. Experimental*. Proceedings of the Royal Soc of London Series A-Mathematical and Physical Sciences **309** (1969) 397.

[94] KOSINA, S., BALUCH, S., ANNUS, J., OMASTOVA, M., AND KRISTIN, J., *Study on the electrical-conductivity and morphology of porous polypyrrole layers prepared electrochemically in the presence of pyridinium chlorochromate*. Journal of Materials Science **29** (1994) 3403–3407.

[95] MOTT, N. AND DAVIE, E., *Electronic processes in non- crystalline materials, second edition* (Oxford University Press, 1979).

[96] TALUKDAR, D., NANDI, U. N., BARDHAN, K. K., BUFON, C. C. B., HEINZEL, T., DE, A., AND MUKHERJEE, C. D., *Nonlinearity exponents in lightly doped conducting polymers*. Phys. Rev. B **84** (2011) 054205.

[97] MENON, R., YOON, C., MOSES, D., HEEGER, A., AND CAO, Y., *Transport in polyaniline near the critical regime of the metal-insulator-transition*. Phys. Rev. B **48** (1993) 17685–17694.

[98] KOPPINEN, P. J., KUHN, T., AND MAASILTA, I. J., *Effects of Charging Energy on SINIS Tunnel Junction Thermometry*. J. Low Temp. Phys. **154** (2009) 179–189.

[99] ABTHAGIR, P. AND SARASWATHI, R., *Junction properties of metal/polypyrrole Schottky barriers*. Journal of Applied Polymer Science **81** (2001) 2127–2135.

[100] TARKIAINEN, R., ROSCHIER, L., AHLSKOG, M., PAALANEN, M., AND HAKONEN, P., *Low-frequency current noise and resistance fluctuations in multiwalled carbon nanotubes*. Physica E **28** (2005) 57–65.

[101] COLLINS, P., FUHRER, M., AND ZETTL, A., *1/f noise in carbon nanotubes*. Appl. Phys. Lett. **76** (2000) 894–896.

[102] APSLEY, N. AND HUGHES, H., *Temperature-dependence and field-dependence of hopping conduction in disordered systems* . Philosophical Magazine **31** (1975) 1327–1339.

[103] MOONOOSAWMY, K. R. AND KRUSE, P., *To dope or not to dope: The effect of sonicating single-wall carbon nanotubes in common laboratory solvents on their electronic structure*. J. Am. Chem. Soc. **130** (2008) 13417.

[104] FRANKLIN, A. D. AND CHEN, Z., *Length scaling of carbon nanotube transistors*. Nature Nanotechnology **5** (2010) 858–862.

[105] WEITZ, R. T., ZSCHIESCHANG, U., EFFENBERGER, F., KLAUK, H., BURGHARD, M., AND KERN, K., *High-performance carbon nanotube field effect transistors with a thin gate dielectric based on a self-assembled monolayer*. Nano Lett. **7** (2007) 22–27.

[106] RINKIO, M., JOHANSSON, A., ZAVODCHIKOVA, M. Y., TOPPARI, J. J., NASIBULIN, A. G., KAUPPINEN, E. I., AND TORMA, P., *High-yield of memory elements from carbon nanotube field-effect transistors with atomic layer deposited gate dielectric*. New J. Phys. (2008) 103019.

[107] JARILLO-HERRERO, P., SAPMAZ, S., DEKKER, C., KOUWENHOVEN, L., AND VAN DER ZANT, H., *Electron-hole symmetry in a semiconducting carbon nanotube quantum dot*. Nature **429** (2004) 389–392.

[108] JORGENSEN, H. I., GROVE-RASMUSSEN, K., HAUPTMANN, J. R., AND LINDELOF, P. E., *Single wall carbon nanotube double quantum dot*. Appl. Phys. Lett. **89** (2006) 232113.

[109] MASON, N., BIERCUK, M., AND MARCUS, C., *Local gate control of a carbon nanotube double quantum dot*. Science **303** (2004) 655–658.

[110] NYGARD, J., COBDEN, D., BOCKRATH, M., MCEUEN, P., AND LINDELOF, P., *Electrical transport measurements on single-walled carbon nanotubes*. Appl. Phys. A **69** (1999) 297–304.

[111] GROVE-RASMUSSEN, K., JORGENSEN, H. I., AND LINDELOF, P. E., *Fabry-Perot interference, Kondo effect and Coulomb blockade in carbon nanotubes*. Physica E **40** (2007) 92–98.